

2018 NSF/REU

RESEARCH EXPERIENCE
FOR UNDERGRADUATES
IN PHYSICS



STUDENT RESEARCH PAPERS

VOLUME 29



UNIVERSITY OF
NOTRE DAME
College of Science

REU DIRECTOR
UMESH GARG, PH.D.

REU Student Research Papers – Summer 2018
University of Notre Dame – Department of Physics

Student	Research Title	Page No.
Noah Applegate Monmouth College	Redesigning and Testing Silicon Detector Array for TwinSol and SSNAPS	1
Andrea Carolina Barros Sarmiento University of Atlántico	Atmospheric Neutrinos with Deep Underground Neutrino Detector	11
Quinn Campagna College of William and Mary	Optimization of the ND MR-TOF	19
L. Alberto Cañizares Dublin City Univeristy	Analysis of the cataclysmic variable GY CNC light curve over two K2 campaigns	29
Zhiyuan Cheng Xi'an Jiaotong University	Controlling Transport with Strain	39
Emily Churchman Texas Luthern University	Using HECTOR for Cross Section Measurement of $^{102}\text{Pd}(p,\gamma)^{103}\text{Ag}$	49
Leah Clark University of Wisconsin-La Crosse	Thin Film Target Preparation and Techniques for Accelerator Low Energy Nuclear Physics	59
Zach Drennan Univeristy of Southern Indiana	Preparation of Rhinoceros Extended Gas Target for Future Experiments	69
Emi Eastman Whittier College	Using Particle-Induced Gamma-Ray Emission Spectroscopy to Detect Fluorinated Substances in Personal Care Products	77
Brooke Emison University of Central Florida	On the Effect of Increased Luminosity on Stubs per Jet and Algorithm Efficiency	87
Rebeckah Fussell Haverford College	Simulating an Interdependent Network of Fibroblasts and Heart Cells	97
Kevin Greif University of Notre Dame	Bend Consistency Cut Performance in the CMS Detector L1-Trigger Upgrad	107
Phuong Thi Hoang Hanoi Natl' Univeristy of Education	Supernova Progenitors of Light Elements Abundances in R-Process-Enhanced Stars	117
Kemo Jammeh Berea College	Dependence of Helium Atmospheric Pressure Plasma Jet (APPJ)-Induced DNA Damaage on Voltage Pulse Frequency and Irradiation Time	127
Michael Kurkowski University of Notre Dame	St. George's Weapon of Choice: the LANCE	137
Baiting Liu Xi'an Jiaotong University	An Electromechanical Model of Cardiac Myocyte with Death	143

Mallory McCarthy Texas A&M Univeristy	Production of ^{149}Tb for Medical Diagnostics and Treatment	153
Christopher E. McGrady Purdue University Northwest	Using Particle Interaction Simulations to Understand Tracker Efficiency for the Phase II High Luminosity Upgrade on the CMS Experiment	163
Martin Meier University of Wisconsin-LaCrosse	Measuring Lifetimes of Excited States in ^{170}Er	173
Max Nguyen University of Notre Dame	Thymine Deposition onto Gallium Arsenide and Changes in the Surface Properties	183
Moses Nnaji Texas A&M Univeristy Commerce	A systematic study of GaMnAsP-based magnetic tunnel junctions	193
Robert Power University College Cork	Truncation of Ab Initio Nuclear Interactions	203
Aidan Tollefson Bethel College	Advances in Time Projection Chamber Design for Nuclear Reaction and Nuclear Structure Detection	213
Xianfeng Wang Xi'an Jiaotong University	Reconstruction of HIPPO Supersonic Gas Jet Target	223
Tino Wells University of Hawaii at Hilo	Galactic Archeology	233
Connor Williams Villanovan University	A Proposal for Experimentally Measuring the $^{35}\text{C1}(^3\text{He},2p)^{36}\text{C1}$ Cross Section: Early Solar System Irradiation Effects on Short-Lived Radioisotope Production	243
Hulin (John) Yang Xi'an Jiaotong University	Constructing and Developing the Instrumentation for Dissociative Electron Attachment Studies	253
Theodora Zastrocky Regis Univeristy	Using Spectral Stacking to Probe the Baryonic Mass of the Milky Way Halo with Fe XIV absorption	263

Redesigning and Testing Silicon Detector Array for TwinSol and SSNAPS

Noah Applegate

Advisor: Dan Bardayan

2018 Notre Dame REU

Abstract

This summer I worked with the SSNAPS, Solenoid Spectroscopy for Nuclear-Astrophysics Studies, group to prepare the TwinSol device for an experiment in early August. This experiment consists of using silicon position-sensitive detectors to gather information from light charged particles fragmented by a light beam interacting with some type of heavy source. This experiment was done last December, but there was determined to be too much data lost with the current setup. This prompted the project that I worked on this summer which was minimizing the dead area of the setup. The main changes were shortening the boards that connected the detectors together and offsetting them to the right of the beam instead of directly over. Also, the detector setup in its entirety was moved deeper inside the solenoid, since the magnetic field where it was currently placed wasn't uniform.

After the changes to the setup of the project were put into place the next step of the project began, which involved testing the new setup to make sure everything performed its function correctly. Thorium-228 was the alpha source used in the experiment and would provide the data for testing the accuracy of the new setup with two separate tests with a possibility for more if time allows. The first with the source being placed directly near the detectors with no magnetic field, and the second test places the Thorium-228 where it will be during the actual experiment with the magnetic field present. All tests performed will also be done in a vacuum environment. These tests will also be later used to calibrate the detectors to help improve the simulations for the experiments that will be performed this upcoming August.

Experiment

This is all being done in preparations for the experiments at the beginning of August. These experiments will be done to learn more about the reactions between certain light beams and heavier sources. For this upcoming testing time the main beam and source of interest is the reaction of a beam of alpha particles, a Helium-4 nucleus, and a Magnesium-24 source with the reaction represented with $^{24}\text{Mg}(\alpha,p)$. Before the main test, a run with a deuterium beam, a deuteron consisting of one neutron and one proton, and Carbon-12, $^{12}\text{C}(d,p)$. This is because this reaction has been well researched and is used to make sure the equipment and devices for the experiment are behaving correctly. If there is still time after performing the first two reactions, a third lesser known reaction will be performed with another deuterium beam and a Fluoride-19 source, $^{19}\text{F}(d,p)$. All these tests will be done with using the TwinSol device at Notre Dame University.

TwinSol is a dual solenoid device that is used to study nuclear fragmentation at low energies though the use of forces caused by the magnetic field.

$$F = q \cdot (\vec{v} \times \vec{B})$$

Eq 1: Equation for forces on charged particles in magnetic field.

In the equation q represents the charge of the particle and the terms in the parenthesis is the cross product of the velocity of the particle and the magnetic field. As reported by the TwinSol collaboration team, the solenoids consist of Nobelium Titanium (NbTi) cables to produce a magnetic field. NbTi is a superconducting material which uses liquid helium to be cooled into a superconducting state, approximately 3 Kelvin (1). Currently one of the solenoids is being replaced, which allows the SSNAPS complete use of the

other solenoid as a helical spectrometer. The spectrometer functions when a current is passed into the NbTi and a magnetic field is produced along the beam line with orientation dependent on the direction of the flow of the current. Since all the reactions being studied are expected to produce particles with positive charge, the magnetic field will not need to be switched between tests. Due to the magnetic forces charged particles that enter the solenoid, from fragmentation of a source and beam coming from the 10MV Van der Graaff accelerator using the SNICS source, will then orbit around the beam line and propelled forward along it. According to Patrick O'Malley of the SSNAPS group, these particles will then spiral inwards towards a detector array which will record their time of flight, energy in the lab frame, and position from the source. This data can then be used to find the initial energy that the particle was emitted with, and the angle at which it was emitted (2). These values will then help identify the reaction that took place between the source and beam.

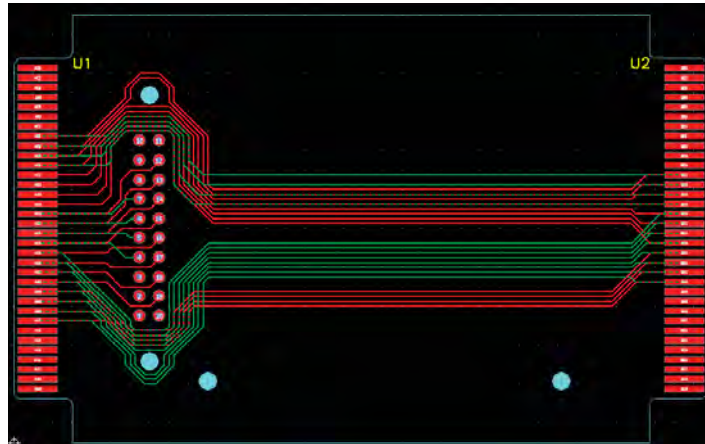
The detector array that is used in this experiment consists of position-sensitive Silicon detectors. These detectors are extremely sensitive and can easily detect particles that are incident on them. Each detector is also split on how it takes in data with the top and bottom side of the detectors performing different functions. The bottom side of the detector takes a full measurement of the energy that the incident particle had. The top side splits it. To help determine where the particle was incident to the detector, the energy value is split between the two ends of the detector due to resistors being placed all throughout the tops of the detectors. The sum of the two energies recorded by the top of the detector should be equal to that of the energy recorded by the bottom, but will have a lesser resolution since the energy is split and the signal to

noise ratio is much worse than the bottom side. This data then would need to be sent to an external device, which was done through a series of boards that were connected and allowed the data to travel.

Detector Boards

During the initial test of SSNAPS experiment, the location of the detectors was realized to be problematic. The spacing between each detector was considerably large, around a few centimeters where the light charged particles would hit but not be recorded. The width of the detectors was also seen to be a problem since the charged particles with very close orbits maybe obstructed form the edge of the boards that were placed directly over the beamline. It was determined since all the particles of interest were determined to share a similar positive charge thus a similar path, the boards and detectors could be offset to allow the low orbiting particles to still be recorded. The original design of the boards had the length of each board to be approximately 120 mm, except for the last board in line which was around 150 mm, with a width of approximately 56 mm. To decrease the dead zone between each detector, the length was changed to a little over 90 mm for most of the boards, 120 mm for the last board, with the same width. The other main change for the new boards were that the holes to attach the board to the main line were shifted to the left of their original positions of the middle of the board by 20 mm. These changes also caused there to be slight alterations to the pathing of the boards, which allow the data from each detector to arrive at the preamplifier. The following figure gives an example of what each of the boards looks like, with the board in the figure being for the one third in line starting at the source.

Fig 1: Third Board Redesign



Alpha Testing

Once the boards had their redesigns completed, the next step was to place the new boards with detectors into the solenoid to provide data that will better the simulations of the experiments to be done in August. Getting the setup in place is a very important step, and one that originally proved difficult. Placing the array of detectors so that they would fit into the smaller entrances in the beam pipe and stay in place was very problematic. This was solved by making a frame that would collapse to fit into the small pipes but could easily be put into its regular shape inside the solenoid. The parts of the frame that held the detectors were added in piece by piece after the target section of the frame was in place.

For these tests, only four of these boards had the silicon detectors on them. This was done by detaching the detectors from one another so that they would fit into the tubing and reassembled in the solenoid. Then using a set telescope at the end of the beam path, the detectors were aligned how they would be during an actual experiment. Once everything was aligned, the detectors were attached inside of the tubing to an

amplifier. An external power source was also attached to this amplifier to give power to the detectors. They were set to be powered by around 150 V, but had larger voltages going to them since each detector had a detectable leakage current in it. The amplifier sent the data that was gathered by the detectors into a detector acquisition unit, DAQ. The purpose of the DAQ is to turn the events that are received from the detector into something that the computer can understand such as where the particle was incident at and the energy values of the particles. The purpose of this was to be able to interpret the data and then calibrate the detectors for better data.

Calibrating the detectors involved using the Thorium-228 alpha source which gave off alphas with a wide range of energies that are well defined, in the range of 5.3 – 8.8 MeV. A well-defined source is needed for calibration so that all the detectors will read the same particle at the same energy value, an energy which may not be known for certain ions of interest. Both sides of the detectors will have to be calibrated separately from each other. With the way that the detector is designed and divided, the calibration will have to be done around 16 times. This was done by forming histograms with each set of data and seeing at which channel the peaks were occurring at. For Thorium-228, six well-formed peaks between the energy levels 5.3 – 8.8 MeV will be formed. Once the channels for each of the peaks for 1 of the 16 data collecting parts of the detector, the channels were then placed into a graph with a line of best fit. This was done to get the slope of the line and zero point. This was then placed into the equation below with $calib(x)$ being the slope and $zero(x)$ the zero point.

$$E = (calib(x) \cdot jbuf + zero(x))/2$$

Eq 2: Equation used to calibrate the backside detectors.

For the histogram made through this process there will be four distinct columns to represent each detector, with the horizontal axis representing the distance from the detectors and vertical axis the energy of the particles. Since we know what that there are six distinct energy values for the particles given off in Thorium-228 alpha decay, each detector should have six lines at the different energies. The uncalibrated data begins to show this, but due to differences in the detectors doesn't have the particles all at the same energy. After being calibrated, the data lines up more and the six energy values of the particles can be clearly seen. The following figures show the histograms with the same data from the first setup for alpha testing, where the source was placed inside the solenoid wall near the detectors. Fig 2 (a) shows the data before being calibrated, while fig 2 (b) shows it after being calibrated.

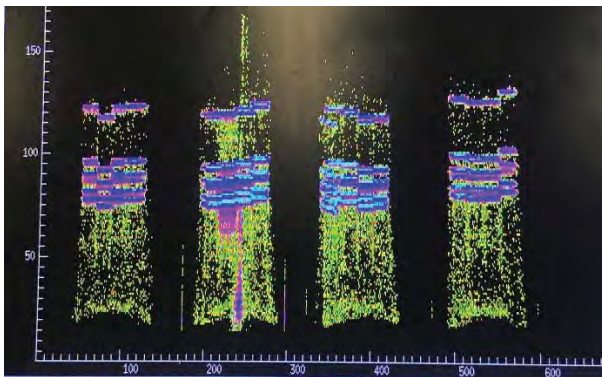


Fig 2 (a).

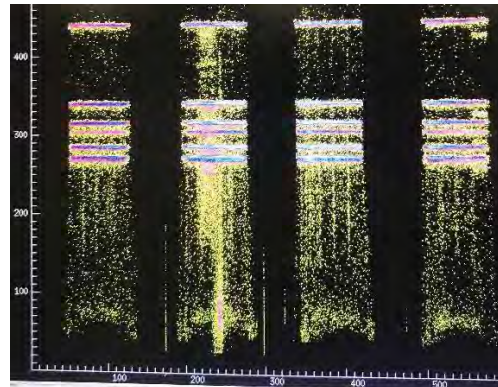


Fig 2 (b).

Figure 2: These figures shows the data from the backsides of the detectors. The horizontal axis signifies the distance of the detector from the source, and the vertical axis is the energy of the particles. Fig 2 (a) shows the uncalibrated data and Fig 2 (b) shows the data after the data has been calibrated.

Conclusions

The main objective for my project this summer was to test a new setup for the SSNAPS group to see if it would perform as well as they calculated it would. These

alpha tests were able to give us some valuable information for the upcoming test in August. The tests also allowed for the direction of current in the coils for the desired magnetic field direction to be found, which is a necessity since if the orientation of the magnetic field is incorrect nothing will be seen. After gathering some data, the new setup for the experiment did perform as well as expected. Both alpha trials were successful and gave the expected results from the known alpha source. The data from the backside of the detectors was able to be calibrated. The exact procedure for how the front sides will be calibrated has been figured out, but it will take some time to complete. The success of the backside calibration using the data from the test placing the Thorium-228 inside the solenoid does imply that the front side calibration should also be a successful one.

Even though the tests were successful there still were some changes that need to be done before the final tests. During the tests, one of the silicon detectors was found to have a large leakage current compared to the others being used. The detector that was third in line had a leakage current approximately twice the size of the nearest one to it. This large of leakage current causes the detector to not be stable, and to get more accurate results must be replaced with another silicon detector. This means that the new detector must be calibrated again, which means more alpha tests will have to be done. Another problem was a bad preamp chip which caused one of the channels in a detector to be obscured with noise. The bad preamp chip was replaced and can be tested during the next alpha test for the new detector. Despite this the setup should be ready for testing in the first week of August.

References

1. O'Malley Patrick, D.W. Bardayan, J.J. Koalta, M.R. Hall, et al. (2016). Upgrades for TwinSol facility. *Nuclear Instruments and Methods in Physics Research, vol 376*.
2. O'Malley, Patrick. *Construction of the Solenoid Spectrometer for Nuclear AstroPhysics (SSNAP) at Notre Dame* [PowerPoint Presentation]. Retrieved from http://www.phy.anl.gov/lep/rss2017/omalley_ssnap.pdf

Atmospheric Neutrinos with Deep Underground Neutrino Detector

Andrea Carolina Barros Sarmiento

2018 REU Program
Physics Department, University of Notre Dame

Advisor: Dr. John LoSecco

Abstract

The Deep Underground Neutrino Experiment (DUNE) is an international experiment for neutrino science and proton decay studies. DUNE will consist of two neutrino detectors placed in the world's most intense neutrino beam. In this project we studied the atmospheric neutrinos with DUNE using simulated data to understand the design needs the experiment, with the collaboration of GENIE even generator, Lar batch tools an analysis of energy, moment and direction of this flux of neutrinos will be shown.

Introduction

The latest discoveries have placed neutrinos as the most abundant particles in the universe, are the focus of attention to continue investigating several fundamental questions about the nature of matter and the evolution of the universe. The global neutrino physics community is developing a multi-decade physics program to measure unknown parameters of the Standard Model of particle physics and search for new phenomena. The program will be carried out as an international, leading-edge, dual-site experiment for neutrino science and proton decay studies, which is known as the Deep Underground Neutrino Experiment. The detectors for this experiment will be designed, built, commissioned and operated by the international DUNE Collaboration.

The facility required to support this experiment, the Long-Baseline Neutrino Facility (LBNF), is hosted by Fermilab. Siting the far detector deep underground will provide exciting additional research opportunities in nucleon decay, studies utilizing atmospheric neutrinos that is the study what will realized, and neutrino astrophysics, including measurements of neutrinos from a core-collapse supernova should such an event occur in our galaxy during the experiment's lifetime [1].

Some generators of particle are useful to simulate neutrinos like GEANT, HERWIG, PYTHIA [2] but one of the most new is GENIE event generator that implements a modern framework for neutrino Monte Carlos and includes state-of-the-art physics modules. GENIE with the LAr Batch Tools were very useful for the realization of this project since with them I was able to study the flux of atmospheric neutrinos.

Analysis

atmospheric neutrinos are produced in primary cosmic ray interactions with nuclei in the upper atmosphere. Secondary mesons (mainly pions

and kaons) may decay and give rise to neutrinos [3].

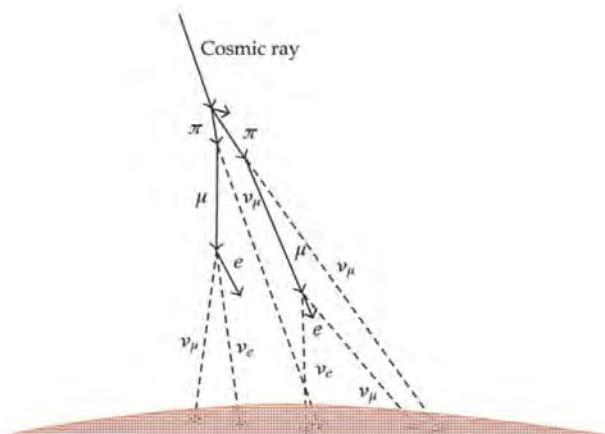


Figure 1. Decomposition of a cosmic ray

In this work we analyze a flux of atmospheric neutrinos generated by GENIE (event generator), in LAr Batch Tools is an executable python script that is the main entry point for user interactions. Project.py is used in conjunction with a xml format project definition file. The concept of a project, as understood by project.py, and as defined by the project definition file, is a multistage linear processing chain involving a specified number of batch workers at each stage.

The general structure of the project file is that it is an XML file that contains a single root element of type "project" (enclosed in "<project name=project-name>...</project>"). Inside the project element, there are additional sub-elements, including one or more stage sub-elements (enclosed in "<stage name=stage-name>...</stage>".

How project python work?

Project python splits simulation, reconstruction and analysis into distinct stages;

gen – generation of particles

g4 – GEANT4 simulation (including TPC, counters, photon detectors)

detsim – TPC readout simulation

reco – Full event reconstruction

ana – analysis output files, and run AnaTree_module on those files. Only these are uploaded to Enstore.

Each stage is sequential (the g4 stage runs on the output of the genie stage), therefore you must wait for the previous stage to be fully completed before starting the next stage.

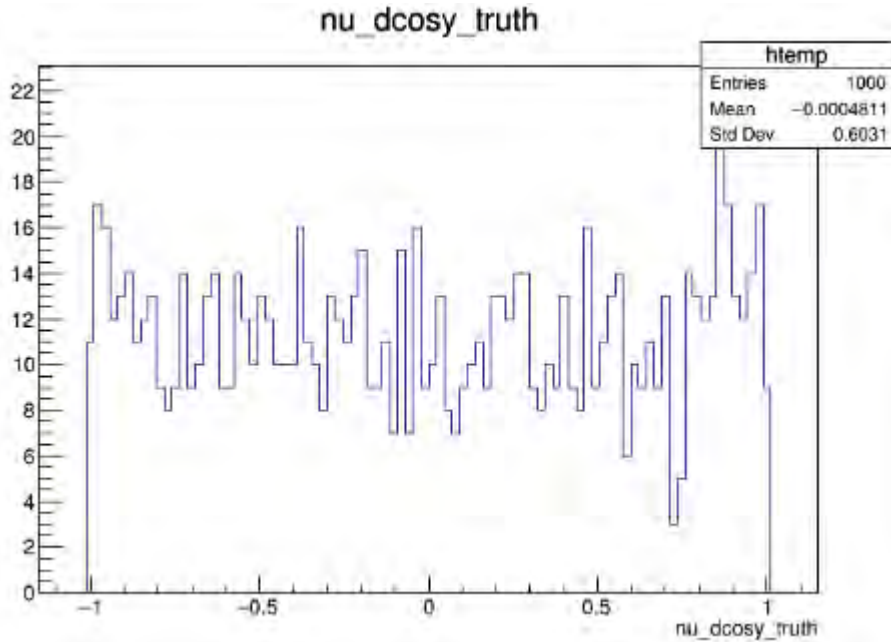
once our project.py is created and run, it shows us table 1.

XML Path:	progenie_atmomax.xml									
Project:	atmomax									
	Output			Check	CheckAna	Fetchlog	Batch Jobs	Submit	Makeup	Update
Stage	Exists?	Art Files	Events	Ana Files	Errors	Missing	Idle	Running	Held	Other
gen	Yes	1	1000	0	0	0	0	0	0	0
g4	Yes	1	1000	1	0	0	0	0	0	0
detsim	Yes	1	1000	1	0	0	0	0	0	0
reco	Yes	1	1000	1	0	0	0	0	0	0
ana	Yes	1	1000	1	0	0	0	0	0	0

Table 1. Project.py

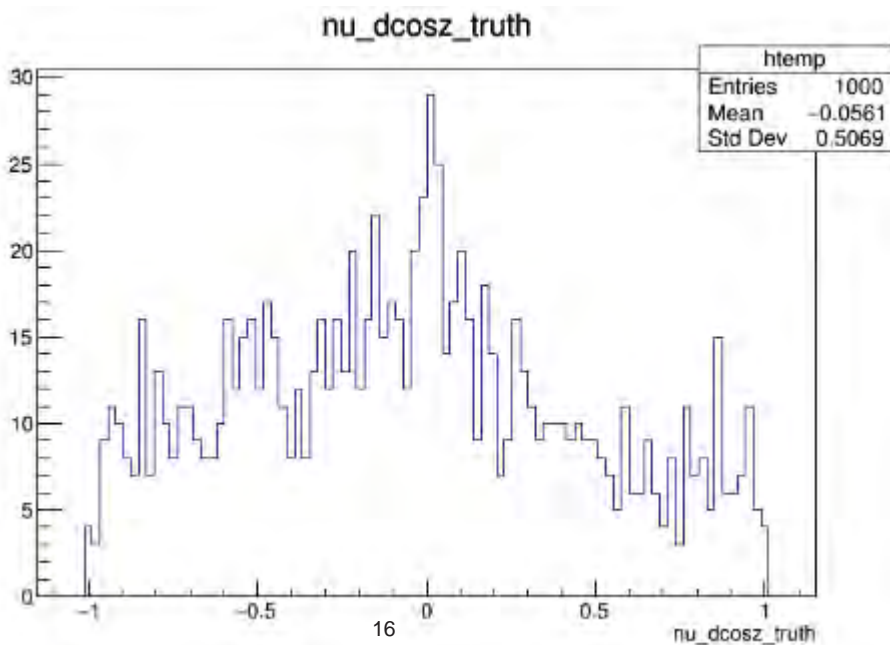
this table show in the left part the output information, in our .XML we make to produce 1000 events and for each Stage produce one ana file except for gen. In the right part are the Batch jobs (there is not much information because in this moment the project.py finished to run).

then we went to analyze the results that anaTree shows us, with these results we get some graphics that allow us to see how was the behavior of this flux of atmospheric neutrinos in DUNE.



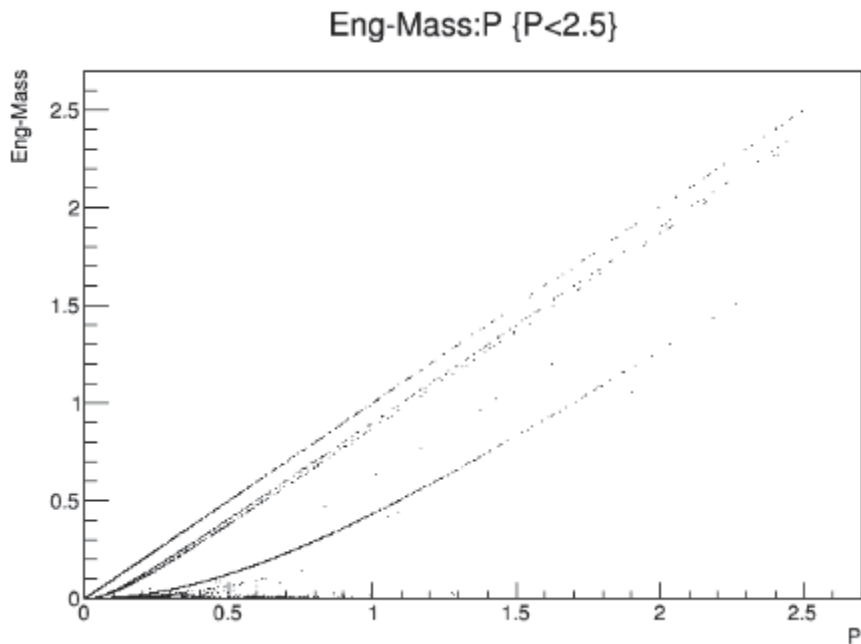
Graph 1. direction $\cos(y)$ of neutrino

this graphics show us the direction $\cos(y)$ of distribution neutrino flux on the detector .



Graph 2. direction $\cos(z)$ of neutrino

This graphics show us the direction $\cos(z)$ distribution of neutrino flux on the detector.



Graph 3. kinematic energy and momentum

in this graph we can observe the kinetic energy of the atmospheric neutrino flux as a function of the moment and it can be detailed that the linear distribution refers to the fact that the less massive particles are found and the curve refers to the more massive particles.

Reference

[1] Collaboration, D. U. N. E., Acciarri, R., Acero, M. A., Adamowski, M., Adams, C., Adamson, P., ... & Amador, E. (2016). Long-Baseline Neutrino Facility (LBNF) and Deep Underground Neutrino Experiment (DUNE) Conceptual Design Report Volume 2: The Physics Program for DUNE at LBNF.

[2] Andreopoulos, C., Barry, C., Dytman, S., Gallagher, H., Golan, T., Hatcher, R., ... & Yarba, J. (2015). The GENIE Neutrino Monte Carlo Generator: Physics and User Manual. arXiv preprint arXiv:1510.05494.

[3] Kajita, T. (2010). Atmospheric neutrinos and discovery of neutrino oscillations. *Proceedings of the Japan Academy. Series B, Physical and Biological Sciences*, 86(4), 303–321. <http://doi.org/10.2183/pjab.86.303>

Optimization of the ND MR-TOF

Quinn Campagna

Advisor: Maxime Brodeur

July 27, 2018

Abstract

A multi-reflection time-of-flight (MR-TOF) that will separate isobaric contaminants produced at the future A=126 beam factory of Argonne National Laboratory (ANL) has been constructed at the University of Notre Dame. The MR-TOF is currently being commissioned using an off-line ion source. This REU project is aimed at optimizing this device in terms of efficiency and resolving power. Both the mirror potentials and injection optics have been optimized. Two dimensional potential scans have been performed to study the dependencies of the various electrodes. This has resulted in a resolving power of 46,000 with an efficiency of 18%.

1 Introduction

Understanding the process of nucleosynthesis through rapid neutron capture is an important problem in both nuclear physics and astronomy [1]. Currently, a facility at ANL is under construction to produce heavy radioactive r-process nuclei with approximately 126 neutrons, similar to the KISS facility at RIKEN, Japan [2]. These nuclei will be produced through deep-inelastic collisions, which

causes the beam and target to exchange nucleons [2]. The masses of these nuclei will be measured with high-precision using a Penning trap [3], and will help in the development of more accurate nuclear mass models.

There is, however, a complication. The production of these nuclei results in a large number of contaminant isotopes, while nuclei of interest are short lived. Therefore, a process to quickly and efficiently separate the nuclei of interest from the contaminants is needed. Such a process can be accomplished by a multi-reflection time-of-flight (MR-TOF) mass spectrometer. An MR-TOF uses two electrostatic mirrors to separate isobars by their mass to charge ratio [4, 5]. By using this device, we can clean the beam to the degree necessary for these mass measurements, which corresponds, in most cases, to a mass resolving power of 40,000 or greater. To achieve such resolving power, we need to optimize the potentials applied across the various components of the MR-TOF, as well as the injection beam line. In addition, we wanted to maximize the efficiency of the device, in order to minimize loss.

2 Setup

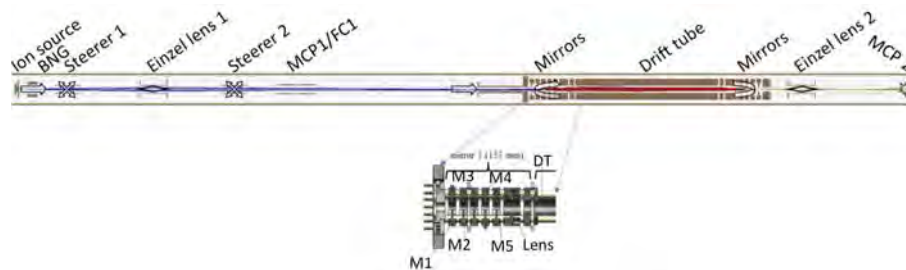


Figure 1: Diagram for the Off-Line Commissioning of the Notre Dame MR-TOF

The off-line configuration of the MR-TOF, shown in Fig. 1, starts with the ion source. The ion source produces primarily ^{39}K , as well as small amounts of ^{41}K , ^{23}Na , ^{85}Rb , ^{87}Rb , and ^{133}Cs

via thermo-ionic emission [6]. The beam is then divided into bunches by a Bradbury-Nielson gate (BNG) [7]. The BNG is made of two sets of interweaving stainless steel wires which are normally held at equal and opposite voltages. For a short amount of time, on the order of 160ns, the voltage across the wires is brought down to zero, allowing the beam to pass. After this time, the voltage is brought back up and the beam is blocked again. This process is depicted in Fig. 2. It should be noted that when the MR-TOF is inserted into the beam line at Argonne, this BNG will be replaced by a radiofrequency quadrupole (RFQ) [8], which will be able to provide bunches with smaller energy spread. Once the ion bunch has been formed, it passes through two steerers and an einzel lens. These serve the purpose of realigning the bunch with the axis of the MR-TOF, as well as focusing the bunches, which maximizes the transmission efficiency.

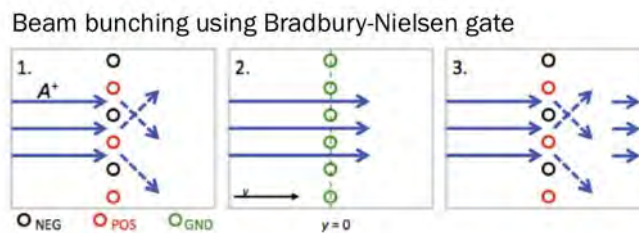


Figure 2: Diagram of BNG Operation. 1 and 3: Beam deflection. 2: Beam is let through

Once the bunch has passed the second steerer, it enters the MR-TOF itself. The main components of the MR-TOF are the two mirrors, the lenses, and the drift tube. The two mirrors are identical, and comprise 5 electrodes, each with a unique voltage, which are critical to obtain a good resolving power. The ND MR-TOF uses the so-called "lift" method [9] to capture the ion bunches. For that method, upon injection, the drift tube will be at potential and drop to ground when the ion bunch enters the MR-TOF, capturing the bunch. This traps the bunch, allowing it to be reflected between the mirrors without escaping the MR-TOF. Between the mirror electrodes are the lenses, used to focus the bunches oscillating in the MR-TOF. By reflecting the bunch, we

can condense a total flight length of thousands of meters to a device of roughly 1 meter in length [5]. As the ions are reflected by the mirrors, they are given a push by the electrostatic force. Because the different species of ions have slightly different masses, the acceleration imparted by this force is unique to each species. This, over time, results in the various isotopes separating out into individual bunches. After the ions have made a sufficient number of loops to produce the requisite resolving power, the drift tube is brought back up to its original voltage, allowing the ions to escape the MR-TOF. The ions are then passed through a second einzel lens to focus them on a microchannel plate detector, which records the individual groups of ions [4, 5]. In the future N=126 beam factory, the ions will instead pass through a BNG in order to remove the unwanted isotopes from the beam. The separation of ions is depicted in Fig. 3.

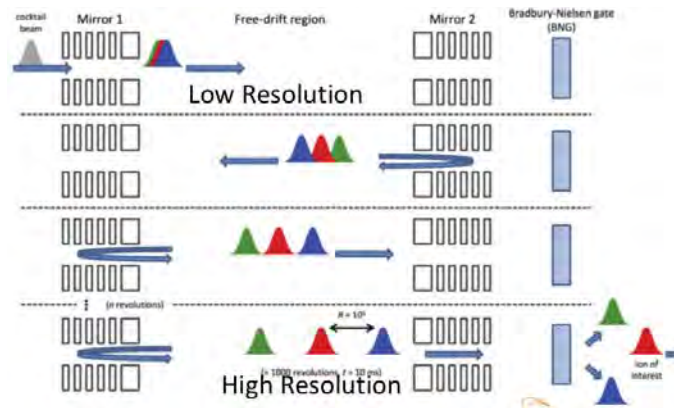


Figure 3: Diagram of Ion Separation

3 Measurements

The first significant sets of data that we took were two dimensional scans of the various mirrors and lenses to check their dependencies. It had been observed that certain pairs are coupled with respect to their effect on the ion bunch. In order to determine this, as well as for optimization

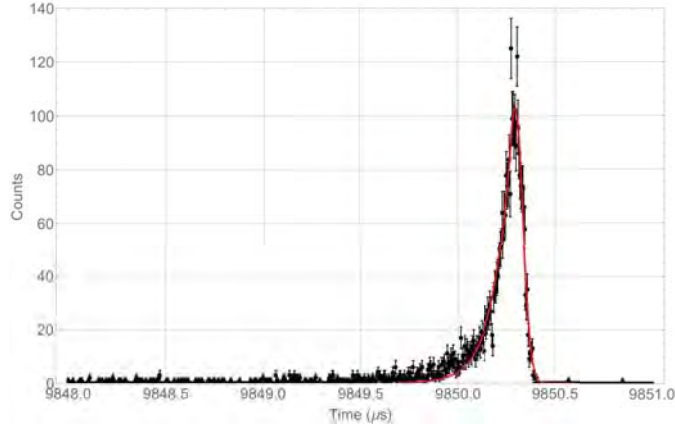


Figure 4: Time-of-flight spectrum of a ^{39}K bunch after 640 loops together with a fit

in general, we measured the total ion count and performed Gaussian fits of the bunches, which outputted the temporal standard deviation of the bunch (σ) and the amplitude of the peak formed by the ^{39}K ion group. The goal was to minimize σ while maximizing the amplitude and total counts. These values were measured using an SRS SR-430 Multi-Channel Scaler. An example of the ion spectra and Gaussian fit is shown in Fig. 4. For each pair, we held one voltage constant while the other was varied, then changed the first and repeated the process until a sufficient range was covered. When making these measurements, it became necessary to adjust the time interval at which the drift tube voltage was raised back to its original level, called extraction time (t_{ext}), in proportion to how much the mirrors had been changed. The times at which the various stages of the MR-TOF were executed were all controlled by a digital delay/pulse generator. Fig. 4 shows two representative examples of 2D scans. Table 1 qualitatively lists the dependencies of each pair of electrodes studied. As seen in the table, the optimal potential on any of the MR-TOF electrodes is completely independent of the EL1 potential. Essentially, the MR-TOF mirrors can be optimized independently from the injection optics. In addition, most pairs of electrodes studied show either no dependencies or a weak dependency. This will make future tuning easier, as it will require only

a limited number of 2D scans.

Strongly Dependent	Weakly Dependent	Independent
M1 vs Lens	M1 vs M5	M1 vs DT
M2 vs DT	M2 vs M5	M1 vs M2
M2 vs Lens	M4 vs M5	M1 vs M3
M3 vs DT	M3 vs M5	M1 vs M4
M3 vs M4	M3 vs Lens	M1 vs EL1
		M2 vs M3
		M2 vs M4
		M4 vs DT
		M4 vs Lens
		M5 vs DT
		M5 vs Lens
		DT vs Lens
		Lens vs EL1
		DT vs EL1

Table 1: Table of Dependencies

After comparing all of the electrodes and lenses, we scanned through different voltage biases for steerer 1 in order to improve the beam transmission. The steerers are held at an overall bias, and the individual components are adjusted to steer the ions up or down and left or right, until the beam passes through the MR-TOF on-axis. For each steerer bias, we created contour plots like those shown in Fig. 5. Once the optimal steerer voltages were determined by these plots, we

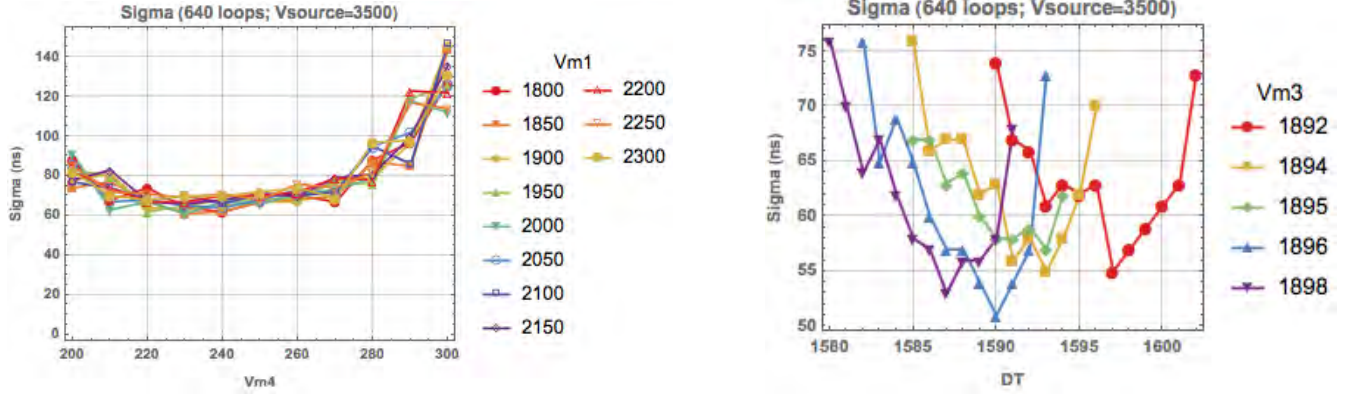


Figure 5: Shows the process undergone with the 2D scans. The left panel is an example of 2 mirrors that are independent: the shape of the dependence of σ with M4 is the same regardless of the potential on M1. The right panel, on the other hand, shows that σ is minimized for different V_{DT} depending on M3.

scanned through voltages for the first einzel lens and the M1 electrode. The data acquired are shown in Fig. 6. The data had been adjusted to account for daily variation in total counts. This was done by retaking a data point from the first day of measurement (bias=1190V). Each set of total counts were then multiplied by the ratio of the original value to the new value to produce the value that would have been acquired on that first day.

Periodically throughout this process, we conducted scans of the resolving power and efficiency of the MR-TOF as a function of the number of round trips the ions made before ejection. This was done by simply adjusting the ejection time to that which corresponded to the desired number of round trips. In addition to the measured values already described, we also recorded t_{mid} , or the time at which the ions hit the detector after exiting the MR-TOF. The resolving power is calculated using the equation:

$$R = \frac{\bar{t}}{2\Delta t}$$

where \bar{t} is the time of flight (time from source to MR-TOF+total time bunch is in MR-TOF, $t_{ext}+t_{mid}$),

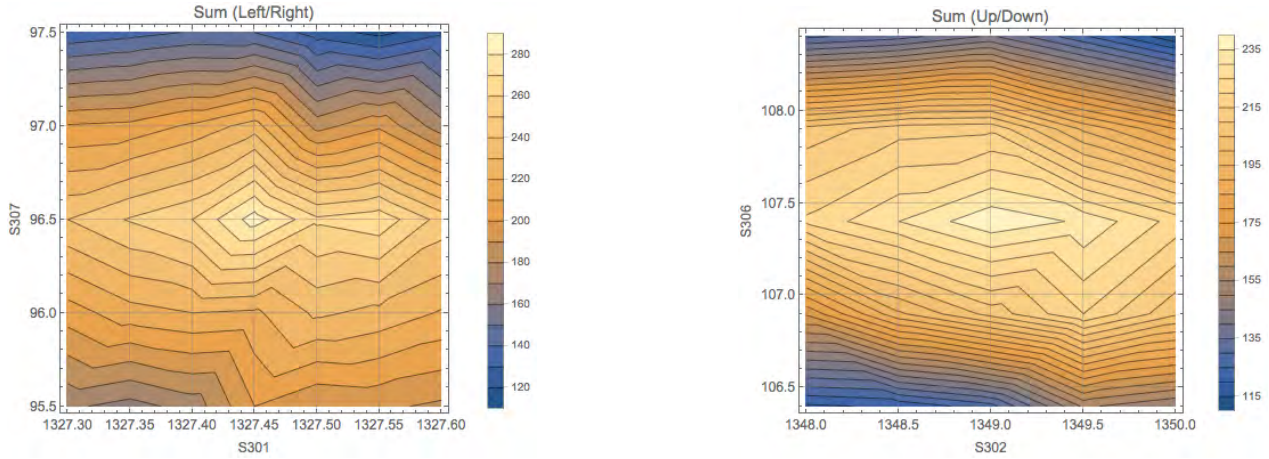


Figure 6: Contour Plots of Steerer Voltages and Total Ion Counts. S301 and S302 correspond to voltages on Steerer 1, and S306 and S307 to Steerer 2.

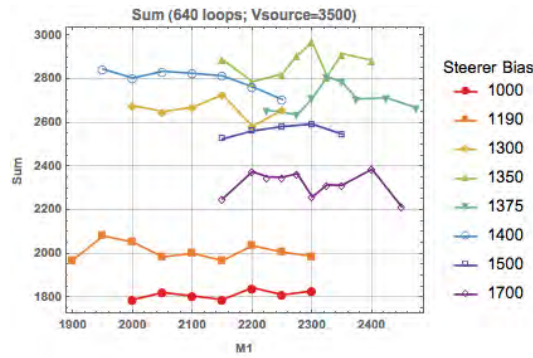


Figure 7: Comparison of Steerer Bias Scan, Adjusted for Daily Variation

and Δt is the full width at half maximum of the ion signal ($2.355 \cdot \sigma$) [4, 5]. The efficiency is simply the ratio of the total ion count at a given number of loops to the total number detected when the ion bunch is allowed to pass straight through the MR-TOF ($t_{ext} = 1 \mu s$). All times here are measured in microseconds. The MR-TOF can currently achieve a mass resolving power of 46,000 with an efficiency of 18%. The most recent resolution and efficiency scans are depicted in Fig. 7. The sharp increase in R near 640 loops is due to the bunch reaching its time focus. The sudden drop in efficiency in that region, however, is not understood, and will require further investigation.

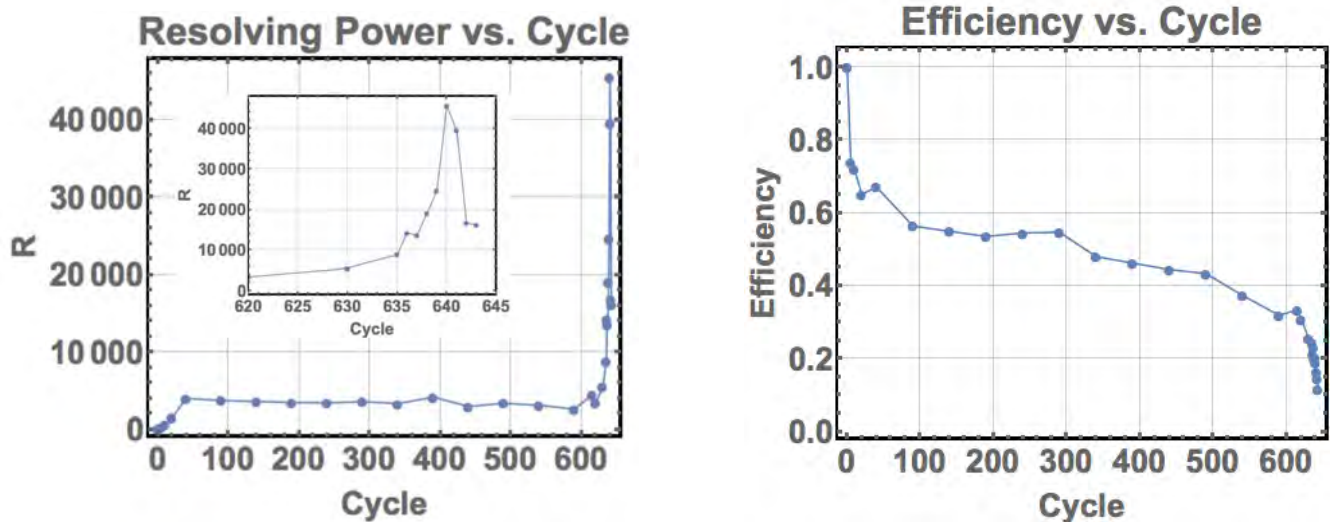


Figure 8: Resolving Power and Efficiency vs Cycles

4 Conclusion

Over the course of the summer, the goal of reaching resolving powers of $>40,000$ on the MR-TOF has been achieved. This was done through the optimization of voltages across the electrodes and other components of the MR-TOF. However, there is still room to improve the efficiency, which is currently at 18%. We have attempted to address this through adjustments to the steerers. Going forward, our main focus will continue to improve the efficiency of the MR-TOF.

References

- [1] C. J. Horowitz *et al.*, arXiv:1805.04637
- [2] Y. X. Watanabe *et al.*, *Nucl. Instr. Meth. B* **317**, 752 (2013).
- [3] J. Dilling *et al.*, *Ann. Rev. Nucl. Part. Sci.* **68**, 45 (2018)
- [4] B. Schultz *et al.*, *Nucl. Instr. Meth. B* **376**, 251 (2016)
- [5] R. Wolf *et al.*, *Nucl. Instr. Meth. A* **686**, 82 (2012)

[6] www.cathode.com

[7] T. Brunner *et al.*, *Int. J Mass Spec.* **309**, 97 (2012)

[8] B. R. Barquest *et al.*, *Nucl. Instr. Meth. A* **866**, 18 (2017)

[9] R. N. Wolf *et al.*, *Int. J Mass Spec.* **313**, 8 (2012)

Analysis of the cataclysmic variable GY CNC light curve over two K2 campaigns.

Author: L Alberto CAÑIZARES

NSF/REU Program

Physics Department, University of Notre Dame

Advisor: Peter GARNAVICH

Abstract

Following the release of the Kepler K2 campaign 16 data, this study investigates the lightcurves observed by Kepler on the eclipsing cataclysmic variable known as GY Cnc located in the constellation Cancer. Previous analysis made by Kato et al. [1] and later, by Feline et al. on the same star [2], led to suggest that the eclipsing variable follows a period of 4.2 hours, however the precision of these measurements was low due to the nature of ground observations. With the benefit of the K2 being a space telescope, a more precise value for this period is possible. This improvement is a result of K2 being capable of making one minute cadence observations for a period of three months, continuously, for each campaign. An ephemerides analysis was performed over K2's Campaigns 05 and 16 and is compared with eclipse timings from the literature and AAVSO observations. Such an exclusive set of data provides a unique opportunity to search for orbital period changes over a long time scale.

1 Introduction

Cataclysmic variables (CVs) are binary star systems consisting of a white dwarf (primary star) and a small star on the main sequence, usually a red dwarf (secondary star) [1]. Such systems evolve from a sun-like star and a red dwarf in a wide orbit. However, due to the much smaller lifetime of a sun-like star, the primary will run out of fuel becoming eventually a white dwarf. As this process takes place, the primary star will start shedding its outer layers shrinking the binary system distances, complying then with the laws of conservation of angular momentum [3]. If the right conditions are met, the two stars will start to get closer to each other, to the point where the secondary star will overflow the Roche lobe of the white star [4]. This means that due to the close proximity of the two stars and the dense nature of the white dwarf, the secondary star will start transferring mass to the white dwarf forming an accretion disk around it. This accretion disk is a particular characteristic of CV's, a

“bright spot” will form in the point where the material of the donor hits the disk, generating another source of variability for this system [3]. If that was not enough, if the rate of mass transfer from the donor to the disk is faster than the rate of mass flow from the disk towards the primary, mass will build up in the disk and thermal instabilities will occur as a result of the increase in viscosity [2], reaching a critical value which will result in a rise in luminosity of up to 5 mag [2]. This period is known as outburst. Some CVs might also fall in the category of eclipsing binaries. If the orbital plane is directly aligned with the observer, the much cooler star will block some of the light produced by the system as it transits in front of the observer. Such periodicity is useful in determining mass ratios and consequently changes in the period could also mean significant changes in the geometry of the system.

2 Observations

The eclipsing cataclysmic variable GY Cnc, was observed using the space telescope K2 at its shortest cadence (1 minute) during campaigns 05 and 16. C05 took place in 2015, for 75 days without interruption between the months of April and July. C16 observed the source between December of 2017 and February of 2018 for 80 days without interruption.

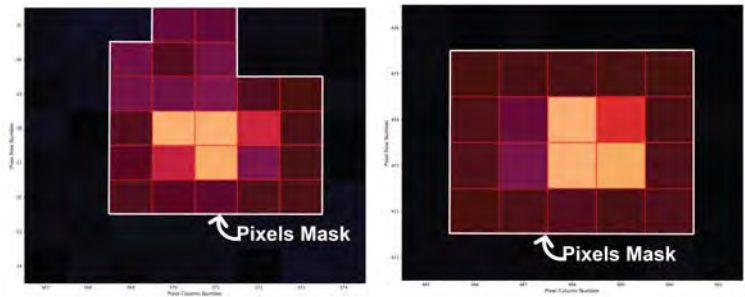


Figure 1: GY Cnc as seen by K2 Campaigns 05(Left) and 16(Right). Pixels masks are selected manually (as shown) using the software package Pyke. Lightcurve extracted from this mask.

The lightcurve was processed in order to correct for the drift of the spacecraft and data points

flagged by the spacecraft were removed. The software package Pyke was used in order to manually select pixels of interest from the MAST data set and later the data was cleaned using background subtraction. As it can be seen in Figure 1, C05 was a rather challenging observation. The wider area of the mask is due to the apparent movement of the star in the CCD. This is attributed to the fact that GY Cnc was located at the edge of the CCD when the observation took place and the image quality is poor. Campaign 16 on the other hand was found to be much better centred and therefore a more precise mask was possible. Data from the AAVSO archive and published data by Kato et al. [1] was also used for the purpose of comparing the data obtained by K2 in order to get a more precise representation of the orbital period of the eclipsing variable.

3 Method

In order to get a more precise representation of the orbital period of the binary system, an ephemerides analysis was performed. In order to do so, timings at which every eclipse occurs were taken and they were attributed a particular epoch number. The relationship between the epoch number and the timing of each eclipse is a direct representation of what the system is doing. If the system is orbiting at a constant orbital period then the following equation applies:

$$T_{eclipse} = PE + t_0 \tag{1}$$

where $T_{eclipse}$ is the time of the particular eclipse, E is the epoch number of that particular eclipse, P is the period and t_0 is a constant.

However if the system was observed to be varying its period, a more accurate representation of the system would be described by:

$$T_{eclipse} = \alpha E^2 + PE + t_0 \tag{2}$$

where $\alpha = 1/2\bar{P}\dot{P}$ is the governing constant for the rate of change of the orbital period. This means that assuming that in such a small time-scale[5], the orbital period is essentially constant and plotting the eclipse timing vs the epoch number should give a linear fit. It is therefore, crucial for the accuracy of the analysis to find a precise method of obtaining the eclipse timings. To do so, the light curve during the eclipse was approximated to a quadratic fit and the eclipse timing is found using the following method:

- 1) An approximate period is found using a power spectrum of the lightcurve.
- 2) Based on this approximate period the first period of the lightcurve is isolated.
- 3) The minimum point in the lightcurve is assumed to be part of the eclipse. An n number of points are taken before and after that “minima”, a first iteration quadratic fit is applied to these points.
- 4) The minimum of the quadratic is found by $x_{min} = \frac{-b}{2a}$ where the constants a and b are obtained from the fit in the form $y = ax^2 + bx + c$.
- 5) Steps 3 and 4 are repeated, taking the minimum point of the quadratic as the new minimum.
- 6) The software moves to the next eclipse by moving half a period from the eclipse minimum and starts the process again. This method is particularly useful in some eclipses where the eclipse is not particularly well defined by the data as some points had to be removed due to flags made by the spacecraft such as when the engines are fired to readjust the orbit.

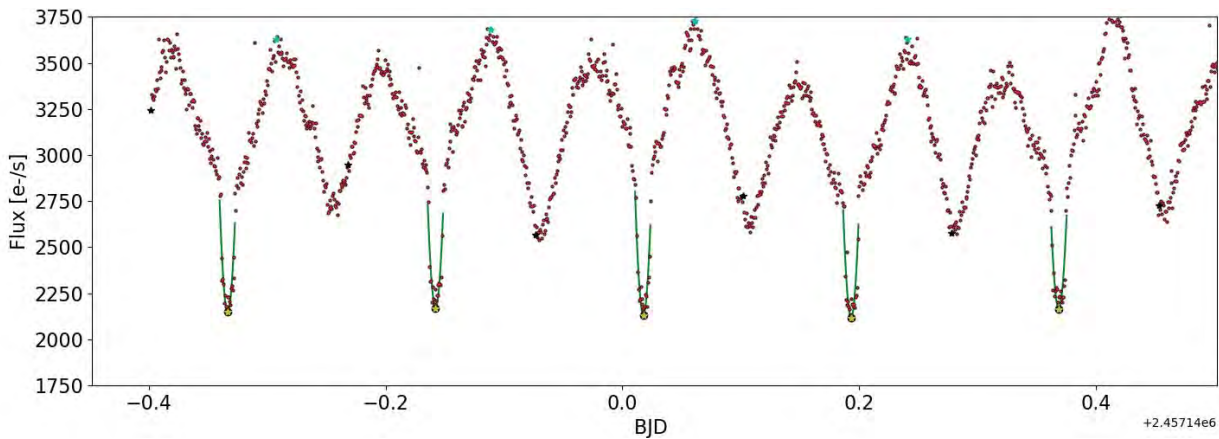


Figure 2: First 5 eclipses of the K2 C05 data set. Continuous line shows the quadratic fits for each cycle. The minimum point is assumed to be the eclipse time point.

4 Results

The lightcurves obtained by K2 are as shown:

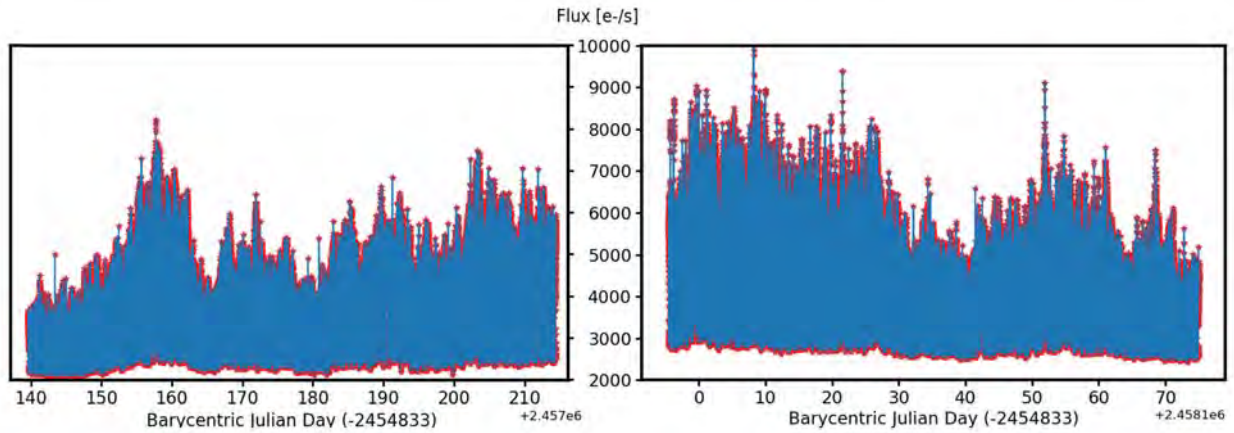


Figure 3: Lightcurve of GY Cnc obtained during Campaign 05(Top) and Campaign 16(Bottom).

The lightcurves of the K2 observations show immediately the variability of the source. The flux in C05 almost doubles within 20 days as shown by the peak between the 2320 and 2330 BJD (-2454833) and if compared to the flux in C16, the average flux of GY Cnc is much superior to the flux in C05, however C16 did not present a large and sudden variation as the data in C05.

The data was then analysed by making a power spectra:

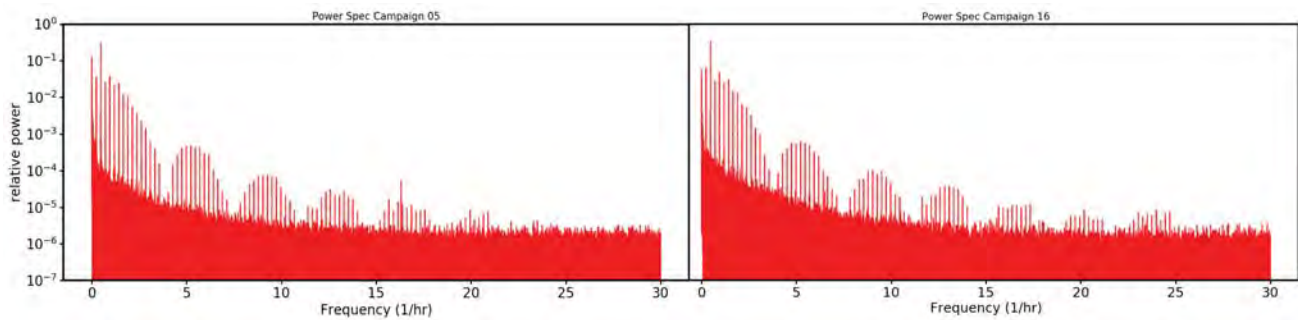


Figure 4: Lightcurve of GY Cnc obtained during Campaign 05(Left) and Campaign 16(Right).

Each of the peaks in the power spectra represents a harmonic of the orbital period and therefore by plotting vertical lines separated equally by a constant (the period). It is possible to determine a rough estimate of the period as fine tuning will show eventually a perfect match of all these

harmonics. Campaign 05 shows a particular peak that does not match an orbital harmonic (at around $\nu = 16.3[1/hr]$) which is a harmonic frequency beating against the 1 minute cadence of the data. The peak is gone in C16 due to the spacecraft position with respect to the earth and the source and its velocity vector. The spectrum also shows a large number of frequencies that look like noise, shown under these harmonics, this is attributed to the randomness generated by the bright spot of the CV. Consistency between the two observations was to be expected.

4.1 Ephemerides Analysis

The epochs of the data were obtained to a first approximation by adding the data to the relationship found by Feline et al. [2]. Note AAVSO data was also added into the the ephemerides analysis.

Manual fine tuning was then applied and the fit was updated as shown:

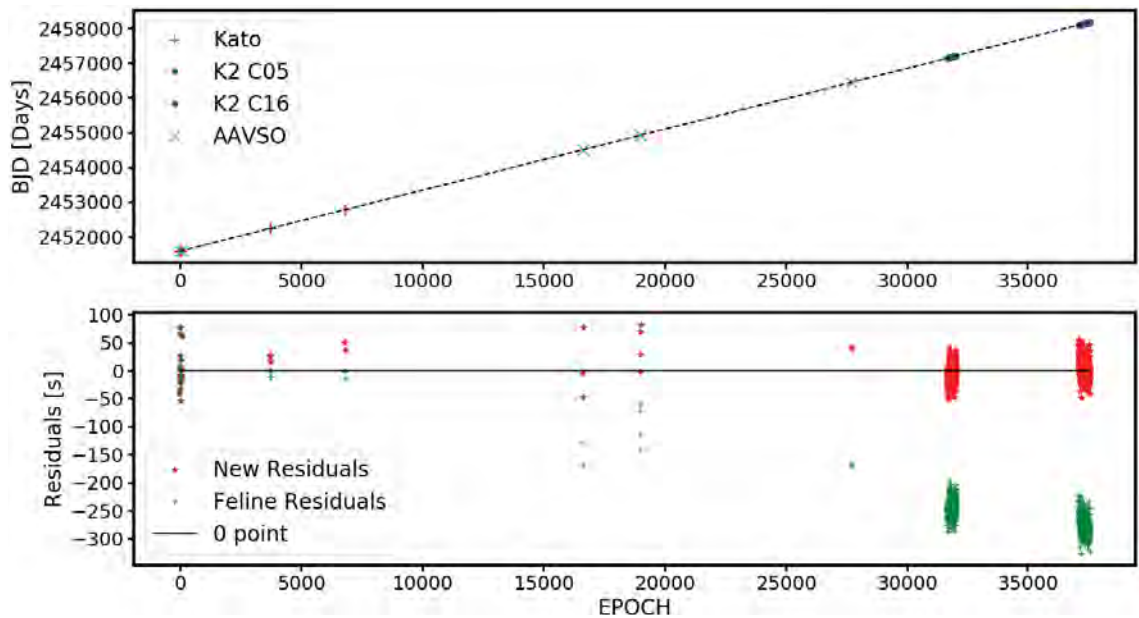


Figure 5: Ephemerides of the K2 data including data from the AAVSO and Kato et al. [1]

This gives an orbital ephemeris of:

$$\text{BJD} = 0.1754424121 \text{ E} + 2451586.212797 \pm 40$$

The new proposed orbital period of GY Cnc is $P_{GYCnc} = 0.1754424121 \pm 1.2 * 10^{-09}$ days, or 4 hrs 12 mins 38.2244 s, which compared to the period proposed by Feline et al.[2] $P_{Feline} = 0.1754424988 \pm 2.1 * 10^{-09}$ is only a 7.5 ms improvement. However, such a small error rapidly propagates with time. As it can be observed in Fig.5 the error in the Feline ephemerides would be of more than 300 s by campaign 16. The improved period is thanks to the capabilities of K2, making continuous observations at the small cadence of only 1 minute for a period of months.

4.2 Maximum flux of each period vs ephemerides residuals

Additional to the ephemerides analysis, it was noticed that the maximum flux value during a particular period, shows a correlation with the residual value obtained in the ephemerides analysis.

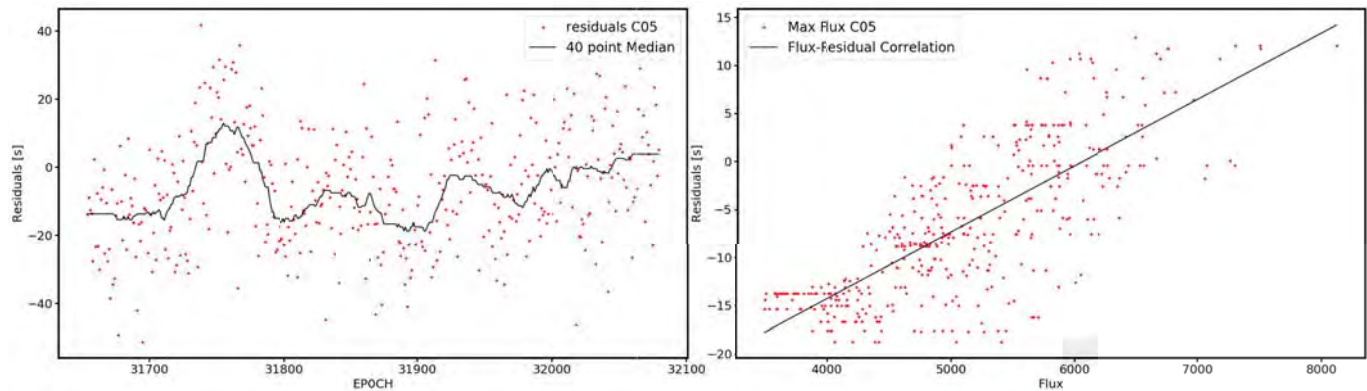


Figure 6: Correlation between the maximum flux in the epoch period and the corresponding residual from the ephemerides analysis. Campaign 16 is not shown due to the similarity of the graphs. The residuals were smoothed out using a 40 point median filter.

A possibility for this effect could be that the influence of the bright spot during the eclipses could lead to slight apparent changes in periods as a result of the geometry of the primary/bright spot/secondary with respect to the observing telescope. Flux will be at its maximum when the primary, bright spot and secondary are visible. However when the bright spot and the primary are being

eclipsed by the cooler star, the flux will be at its minimum. There will be times where the bright spot will be visible while the primary is still being eclipsed and hence the bright spot shifts the apparent orbital period of the system, acting like a third body in the equation. In addition, the bright spot is a known [3] source of random fluctuations which would explain the large spread of the data. The graphs shown in Fig. 6 are the fits from C05. The reason C16 was not shown is due to the similarity of the graphs. The Epoch-Residuals graph was smoothed out by applying a median filter (Note solid line). This was done to get a higher signal to noise ratio. The slopes of the C05 and C16 Residuals - Flux correlations were $(8.0 \pm 0.3) \times 10^{-8}$ and $(4.8 \pm 0.3) \times 10^{-8}$ respectively. Both slopes are within tolerance of each other suggesting that this effect is not time dependent.

5 Conclusion

The large contribution of the K2 space telescope data towards the eclipsing cataclysmic variable GY Cnc makes it possible to obtain large continuous sets of data. Compared to the data obtained from ground telescopes, these data sets represent an invaluable opportunity to investigate the nature of cataclysmic variables.

This study used primarily two sets of data from Campaigns 05 and 16 of the K2 mission . The data was compared to the previously published data by Kato et al. [1] and the AAVSO and a new orbital period is proposed for this object. The orbital period proposed is $P_{GYCnc} = 0.1754424121 \pm 1.2 \times 10^{-09}$ days which is 4 hours 12 mins and 38.2244s.

Finally it was observed that the maximum flux of a particular period showed a correlation with the residuals obtained during the ephemerides analysis which could be a result of the bright spot being a third source of light variation during the eclipses.

References

- [1] Takeyoshi Kato, R Ishioka, and M Uemura. Outburst photometry of the eclipsing dwarf nova gy cancri. *Astronomical Society of Japan*, 54, 09 2002.
- [2] W J. Feline, V S. Dhillon, T R. Marsh, Christopher Watson, and S Littlefair. Ultracam photometry of the eclipsing cataclysmic variables gy cnc, ir com and ht cas. *Monthly Notices of the Royal Astronomical Society*, 364, 10 2005.
- [3] Coel Hellier. *Cataclysmic variable stars : how and why they vary*. Springer Published in association with Praxis Pub, London New York Chichester, UK, 2001.
- [4] T. S. Khruzina, I. B. Voloshina, and V. G. Metlov. A photometric study of the eclipsing dwarf nova gy cnc in quiescence and during an outburst. *Astronomy Reports*, 60(11):971–995, Nov 2016.
- [5] M. T.-C. Yang, Y. Chou, C.-C. Ngeow, C.-P. Hu, Y.-H. Su, T. A. Prince, S. R. Kulkarni, D. Levitan, R. Laher, J. Surace, A. J. Drake, S. G. Djorgovski, A. A. Mahabal, M. J. Graham, and C. Donalek. Long-term periodicities of cataclysmic variables with synoptic surveys. *Publications of the Astronomical Society of the Pacific*, 129(9):094202, 09 2017.

A REU FINAL REPORT

Controlling Transport with Strain

Author

ZHIYUAN CHENG

July 25, 2018

Abstract

One of the driving forces in condensed matter physics research is development of techniques to incorporate nanometer-scale quantum physics into functional electronic devices. Our lab has a bottom-up approach capable of building nanoscale structures that reproduce the behavior of electrons interacting with single molecules. We built strain sensitive transistors by arranging CO molecules on the surface of Copper. We create waveguides that transmit electrons in a quantum coherent manner. We allow these electrons to interact with synthetic structures that present a switch-like behavior similar to a transistor. In my research I performed numerical simulations of the structures and helped to plan the experimental phase of this project.

1 Introduction

The electronic industry is able to make nano-scale transistors. However making even smaller transistors can be a great challenge. The traditional transistors consist of three parts - source, drain and gate, we may make source and drain smaller, but making gate smaller is much harder than imagine. In order to do this, we now find a feasible way - we can

introduce condensed matter to this area and design a synthetic transistor(Figure 1). Since electrons can be both particles and waves, we can use scatterers(atoms) to act like walls to affect electrons' behaviors. So if we arrange scatterers in a certain way on a substrate(Cu(111) in this case), like constructing a structure, we then change the electrons' behaviors of the substrate.

In condensed matter physics, we are able to use scanning tunneling microscope to move atoms or molecules as well as observing their electric properties. We can move atoms by using atomic-scale tip, when we need to move atoms, we then drop the tip a little and by applying electric field, we then can drag atoms wherever we need. When exploring the system's capacities, we can move the tip above the substrate and measure its electric capacities. Therefore we can move atoms to construct a 2D structure - in this case, a strain sensitive transistor which is made up of atoms arranged in a strain(shown in Figure 1) - and explore their physical characteristics.

When we explore the transistors' electric capacities, we can measure the current intensity to figure out what is going on. In this case, we measured the wave patterns in different bias, and then figure out a map showing the wave patterns at different locations at a certain bias. By making the

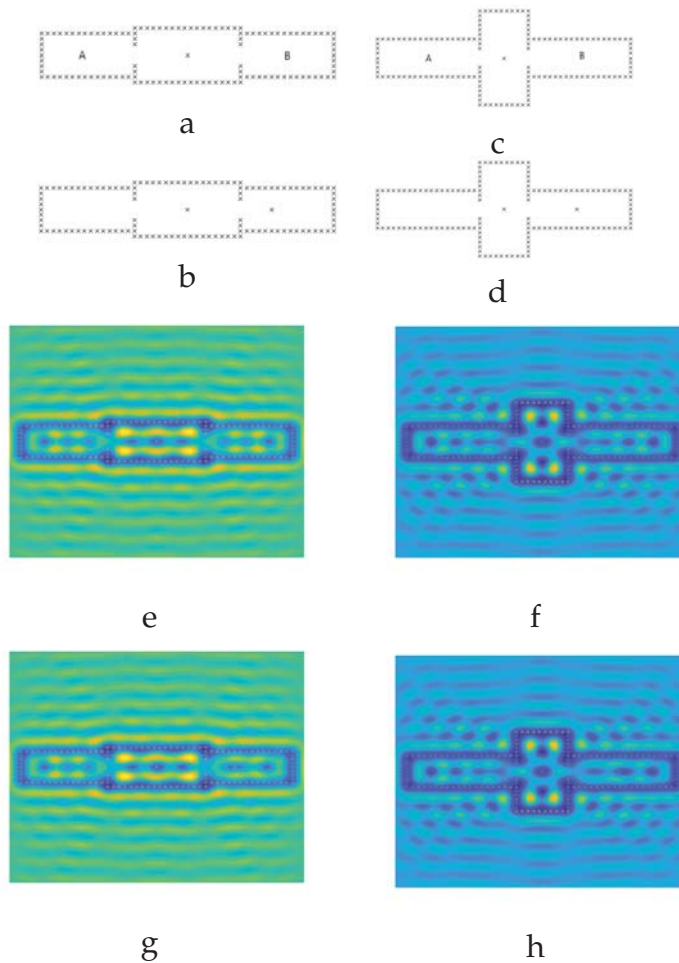


Figure 1: Strain sensitive transistors. A and B are two channels, the change of central structures from vertical to horizontal can be recognized as a process of stretch, and putting a scatterer on channel B is like applying bias to a transistor. a: horizontal dots map without a scatterer, b: horizontal dots map without a scatterer, c: vertical dots map without a scatterer, d: horizontal dots map with a scatterer, e: horizontal simulation maps without a scatterer under the bias of -0.15V , f: horizontal simulation maps without a scatterer under the bias of -0.15V , g: horizontal simulation maps with a scatterer under the bias of -0.15V , h: vertical simulation maps with a scatterer under the bias of -0.15V . In a-d each "x" shape represents a molecule

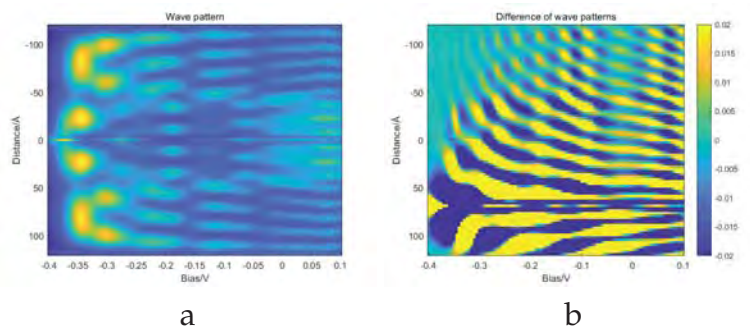


Figure 2: a: we call it the map, the x-axis represents different bias, while the y-axis represents scanning locations at the central horizontal line, by fixing at a certain bias, we can then know the exact wave pattern along the central horizontal line. b: when we draw out two bias maps, one without a scatterer as well as one with a scatterer, we then make the difference of the two and come out the difference of wave patterns(difference for short)

difference between horizontal wave pattern maps, we can see a clear picture of how much it changes by putting a scatterer(as is shown in figure 2). Then by comparing the horizontal difference and the vertical difference, we can tell whether this kind of structure would work.

2 Methods

Before we start the simulation, we need to figure out how the atomic manipulation works so that we can construct functions in Matlab to run.

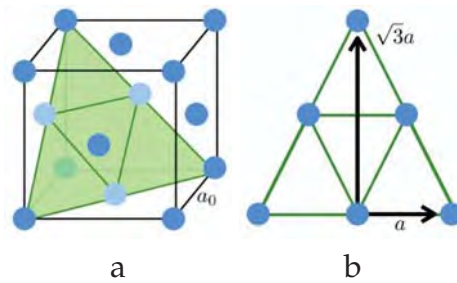


Figure 3: a: Cu crystalline structure, b: Cu(111) substrate

2.1 Copper substrate and CO molecule

Cu crystalline structure is a Face-centered cubic. In this experiment we use single copper crystal and cut the surface along the (111) plane. Since it's a single crystal, every copper atom should be surrounded by 6 atoms with the same space of $a = \frac{a_0}{\sqrt{2}} = 0.255 \text{ nm}$ (shown in Figure 3.a)[1].

In this experiment, we use CO molecules to attach to the copper substrate as well as constrain the surface state electrons of Cu(111). In order to keep the CO molecules absorbed to the substrate, the temperature must be kept below the boiling point (41K), so in the STM, we use Liquid Helium (4.2K) to cool down the whole experiment area.

2.2 Atomic manipulation

How are we going to move atoms, construct strain sensitive transistors and explore their physical characteristics? We can use the STM as a

powerful tool to manipulate atoms. There are two ways of atomic manipulation(Figure 4). The first way is by applying electric field force to drag the atoms, while the second way is to poke down the pin and pick up the atom to a certain location and then use the opposite bias to put the atoms down[2].

However, in this experiment, we use the first way to manipulate CO molecules, on the one hand, it is faster, on the other hand, since we don't have to poke the tip as well as change bias to push molecules to the substrate, we then save energy. Atomic manipulation requires high accuracy, any vibration or electric-magnetic field would affect the experiment greatly, so we built a Faraday cage outside the STM to avoid electric-magnetic field coming in, put the samples in vacuum and cool both tip and substrate to 4.2K to minimize the thermal vibration of atoms.

But how are we going to measure their capacities? There are two accessible ways. The first way is to apply a fixed height to the substrate and tip, then as we scan through the surface, due to the change of electrons' wave, the current we get changes as the conductivity changes, so by drawing out current intensity or conductivity at each point we scanned, we then have the map. The second way is to fix the current intensity, so

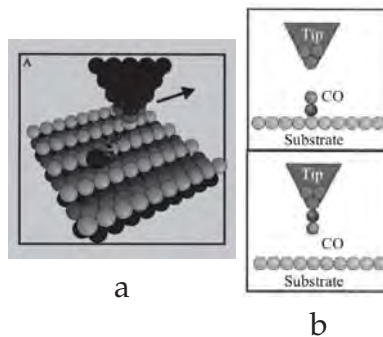


Figure 4: a: move Cu atoms by dragging, b: pick up and put down CO molecules

to maintain the current intensity, the tip will change its height and we can draw the map of height at each scanned point. In our lab, we use both.

3 Simulations

In this experiment, I did the computer simulation to find a structure that shares the greatest change when strain is applied. While building up the structure, it is important to mention that since the wavelength of electrons is a certain value and waves in the structures are stand waves, the channel must be wide enough to allow propagation in the y-direction. Also, we can see that there is a single molecule in the middle of the central structure, we did this to avoid the wave travel through the structure, by adding a molecule in the middle, we can then tell how would the change

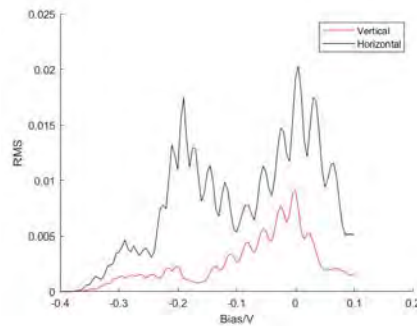


Figure 5: RMS of the difference while the scatterer is put at $(37*a,0)$ and the channel length is $15*a$

in channel B affect channel A. Last but not least, we use the scatterer to simulate a bias across the channel, it is because when we put a scatterer in channel B, the original wave patterns in channel B would change.

After dozens of trails, I finally found a rectangle central structure at a size of $8.662\text{nm} \times 4.412\text{nm}$. After that, I calculated the RMS of the difference and picked five biases that showed the greatest difference.

Acknowledgement

Thank Prof.K.Gomes, D.Green, Dr.Laura.C.Collins for their great help in my academic research. Thank Prof.Garg for giving me this precious opportunity to attend this program. Thank Ms.Lori for much help in my life in Notre Dame.

References

- [1] Laura C. Collins: *Shaping The Potential Landscape: A Study of Atomically Engineered Quasicrystals And Molecules*, University of Notre Dame(2018)
- [2] Gerhard Meyer, Ludwig Bartels, Karl-Heinz Rieder: *Atom manipulation with the scanning tunneling microscope: nanostructuring and femtochemistry*, Superlattices and Microstructures, Vol.25, No.1/2, 1999

Using HECTOR for Cross Section

Measurements of $^{102}\text{Pd}(p,\gamma)^{103}\text{Ag}$

Emily Churchman

2018 NSF/REU Program

Department of Physics, University of Notre Dame

Advisor: Anna Simon

Introduction

Nucleosynthesis of elements heavier than iron (Fe) in stars occur via three different processes: the s-, r-, and p-processes. The s- and r-processes are responsible for the production of a majority of nuclei past Fe by means of “slow” or “rapid” neutron capture, respectively, followed by β^- decay [1]. The p-process occurs less often and is responsible for the production of only 35 proton-rich nuclei, known as p-nuclei, that lie above the line of stability, such as ^{102}Pd and ^{108}Cd [1]. This process occurs in specific stellar environments – burning phases of stellar interiors and supernova explosions – and uses cascades of gamma (γ) rays to initiate reactions [2]. During the explosion, γ -rays then penetrate the supernova and destroy s-nuclei, shifting the overall abundance towards p-nuclei by means of photodisintegration reactions: (γ , p), (γ , n), and (γ , α), that produce unstable nuclei that β^+ decay back towards the line of stability [3]. Although the reactions taking place in the stellar environments are (γ , p), (γ , n), and (γ , α), their cross sections can be determined from the capture reactions (p, γ), (n, γ), and (α , γ) which can be studied in the lab.

By measuring the cross sections, or probability, of p-process reactions, the new cross sections can shed light on different p-process scenarios that occur during the supernova explosions. The experiment conducted at the University of Notre Dame in June 2018 focused on measuring the cross sections for p-nuclei that could prove important to the p-process itself. These cross sections continue to be constrained in hopes of improving theoretical models of the p-process related cross sections. The measured cross sections can then be used in network calculations, along with other parameters such as temperature, that simulate p-process scenarios with different outcomes during a supernova explosion to improve the accuracy of the model network.

Experiment

The detector used for this experiment was the High Efficiency TOtal absorption spectrometeR (HECTOR). This detector consists of 16 4x4x8 inch thallium-doped sodium iodide (NaI(Tl)) scintillating crystals [3]. Each of these crystals is coupled to two photomultiplier tubes (PMT), utilizing a total of 32 PMTs, partially shown in Fig. 1 [3]. The detector is then oriented to create a cubic array surrounding an inserted target, as shown in Fig. 2, creating a 4π steradian coverage. This orientation allows for the individual γ -rays produced during the de-excitation of the reaction products from the target to be measured simultaneously.



Fig. 1: PMTs on the top of HECTOR coupled to the top 8 scintillators.



Fig. 2: HECTOR in a cubic array.

Using the FN tandem accelerator at the University of Notre Dame, a beam of protons was accelerated towards HECTOR and the targets of interest. The experiment took measurements for ^{90}Zr , ^{102}Pd , ^{108}Cd , and ^{110}Cd . However, the data inspected in this analysis focuses specifically on the p-nuclei, ^{102}Pd .

Gamma-Summation

A single decaying nucleus emits a cascade of photons that can be detected as single photons in individual peaks on a spectrum, which is typically produced in conventional detectors [4]. However, in gamma-summing detectors such as HECTOR, each individual γ -ray cascade is recorded as one single energy peak. To demonstrate this technique, the simple decay scheme of ^{60}Co is examined (Fig. 3).

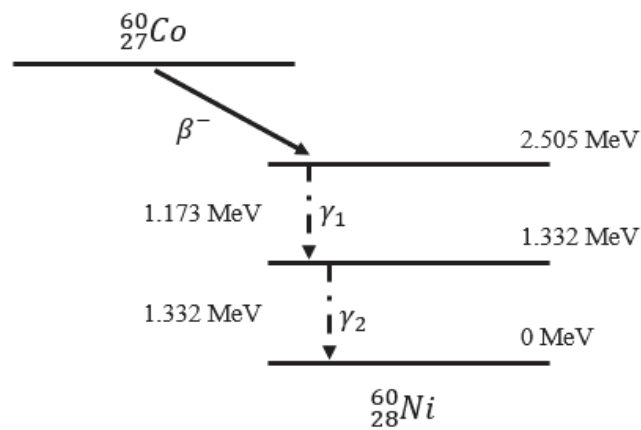


Fig. 3: Decay scheme for ^{60}Co .

After ^{60}Co has β^- decayed to ^{60}Ni and the new nucleus is excited to an energy of 2.505 MeV, 2 γ -rays are emitted to return ^{60}Ni to its ground state. The gamma rays have energies of 1.173 MeV (1173keV) and 1.332 MeV (1332 keV) respectively. In Fig. 4 (top), a traditional γ -ray spectrum displays the 2 individual γ -rays and their energies, with a very small peak at the sum energy of the rays. In Fig. 4 (bottom), the sum spectrum shows one large peak at the total excess energy the nucleus must release when it de-excites.

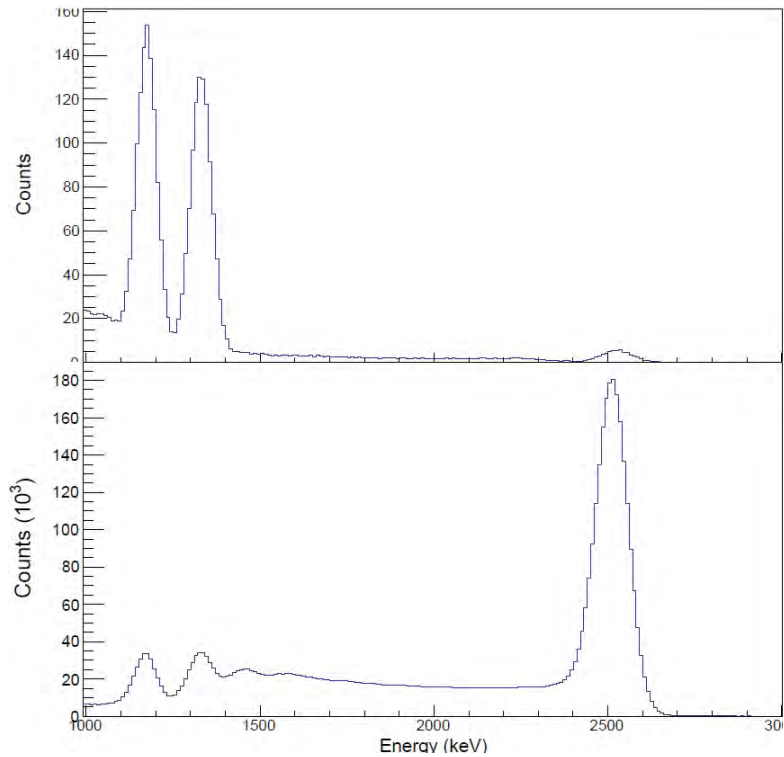


Fig. 4: TOP – Single γ -ray spectrum. BOTTOM - γ -ray summation peak.

In the case of beam induced reactions, the energy of the sum peak, which is the excitation energy of the reaction product, is equal to the sum of the proton beam energy in the center-of-mass system and the Q-value of the target, where $Q = 4.1885$ MeV for ^{102}Pd . For example, if the beam energy is 8 MeV, a γ -ray sum peak would be expected at approximately 12.2 MeV. By taking the integral of this peak, the number of total counts recorded by the detector can be found and used for further cross section calculations.

Background Subtraction

In order to get the correct γ -ray spectrum, a spectrum from the recorded data as well as from a background run, where there is no target or beam in HECTOR, needed to be plotted. The background runs taken from the experiment were at least 4 times longer than most of the data collection runs and therefore needed to be scaled by calculating a time ratio between the data and

background runs. The now scaled background spectrum was subtracted from recorded data spectrum, shown in Fig. 4. This subtraction removes excess γ -rays produced from cosmic rays around the detector that could affect the number of counts recorded by HECTOR during the runs where the reaction is taking place.

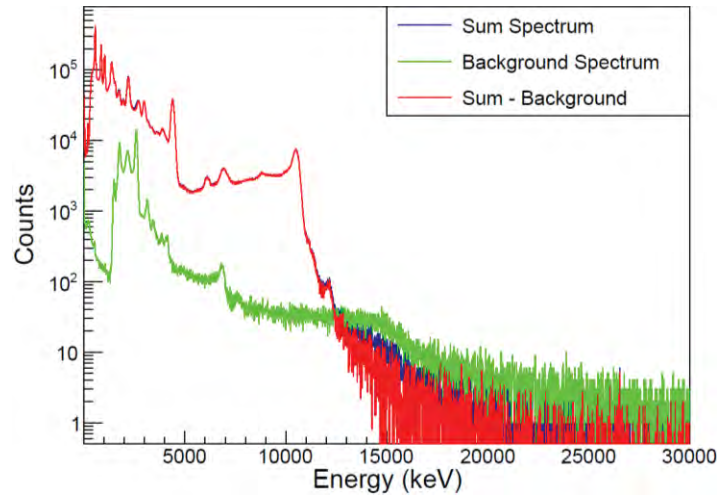


Fig. 5: Full γ -ray sum spectrum for a 6352.2 keV beam energy. Original sum spectrum (blue). Background spectrum (green). Sum spectrum – background spectrum (red).

Integration

To get the integral of the sum peak from the data spectrum, the peak needed to be fit with a gaussian and a first-order polynomial function (to account for the background in the fit). The parameters of this fit varied between energies in order to get the best possible shape of the curve so that it closely matched that of the sum peak. Because it is known that the peak should appear at approximately the sum energy, the gaussian and polynomial were fit over a range around that energy (Fig. 5). After the fitted background was subtracted, the plot was integrated underneath the sum peak to obtain the number of counts from the detector.

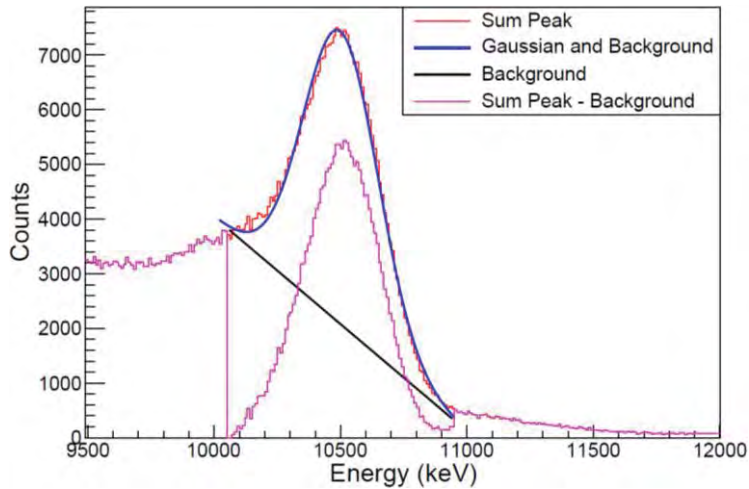


Fig. 6: Original sum peak (red). Gaussian and background fit (blue). Background fit (black). Gaussian with background subtracted (purple).

Multiplicity and Efficiency

One of the values recorded during the experiment keeps track of the multiplicity of an event. The multiplicity is the number of detectors that fired for one specific γ -ray cascade. The number of γ -rays in the cascade is correlated to the number of segments that fired.

The multiplicity then affects the efficiency of the detectors and of HECTOR as a whole. The efficiency (ϵ) tells us the percentage of decays that can actually be detected by HECTOR. The values needed for the efficiency curves cannot be found experimentally but instead are found through simulations that produce 3 coefficients (p_0 , p_1 , and p_2) for a second-order polynomial that is dependent on the multiplicity (m), demonstrated in Equation 1.

$$\epsilon(m) = p_0 + p_1m + p_2m^2 \quad \text{Equation 1}$$

Cross Section Calculations

The cross section of $^{102}\text{Pd}(p, \gamma)$ reactions at given energies is calculated using Equation 2.

$$\sigma = \frac{N_{det}}{N_{beam} * d * \epsilon} \quad \text{Equation 2}$$

In the equation, N_{det} is the number of counts from the detector found by the integral of the sum peak, N_{beam} is the total number of particles from the beam that was found using an analog scalar throughout the experiment, d is the thickness of the target in g/cm^2 , and ϵ is the efficiency of the detector at a given beam energy. The uncertainty in the N_{beam} , target thickness (d), and efficiency was taken at 5%. The center-of-mass energy (E_{CM}) was found by averaging the energy before the beam hits the target and the energy after. The uncertainty in the E_{CM} was found by subtracting either the initial or final energy value from the average beam energy. Finally, the uncertainty in N_{det} was found by taking the square root of N_{det} and the integral of the first-order polynomial fit to the background. Error propagation was then used to calculate the uncertainty of σ .

Results

Cross section measurements were taken at 15 different beam energies. These measurements are listed in Table 1.

Table 1: Resulting cross sections and values used in their calculations

E_CM (keV)	E_CM Error (keV)	Ndet (particles)	Ndet Error (particles)	Nbeam (particles)	Efficiency	d(g/cm ²)	Cross Section (mb)	Cross Section Error (mb)
7813.8	21.0	24917	677	2.66E+12	0.14	6.91E+18	9.56	0.87
7339.5	22.0	30437	694	2.56E+12	0.15	6.91E+18	11.18	1.00
6851.3	23.0	61252	847	3.27E+12	0.15	6.91E+18	17.92	1.57
6358.2	24.0	200275	1432	6.27E+12	0.16	6.91E+18	29.11	2.53
6015.5	25.0	219117	1530	9.76E+12	0.17	6.91E+18	19.22	1.67
6014.6	25.0	123181	1139	5.33E+12	0.17	6.91E+18	19.79	1.72
5866.5	25.5	146042	1193	6.09E+12	0.17	6.91E+18	20.47	1.78
5665.0	26.0	82065	886	4.19E+12	0.17	6.91E+18	16.63	1.45
5473.4	26.5	114222	1062	5.36E+12	0.17	6.91E+18	18.55	1.62
5274.4	27.5	96996	987	6.83E+12	0.17	6.91E+18	12.28	1.07
5078.8	28.0	106903	1113	9.93E+12	0.17	6.91E+18	9.18	0.80
4880.9	28.9	130151	1210	1.43E+13	0.17	6.91E+18	9.18	0.80
4387.6	31.0	127740	1400	1.98E+13	0.19	6.91E+18	4.81	0.42
4189.6	32.0	70983	899	2.45E+13	0.18	6.91E+18	2.31	0.20
3894.0	33.5	54529	881	3.74E+13	0.19	6.91E+18	1.10	0.10

These calculated values of the cross sections, labeled as HECTOR in Fig. 5, were then plotted with theoretical values [5] and measured values from Dillman, et al. [6] and Ozkan, et al. [7], as shown in Fig. 7. The theoretical measurements are found using NON-SMOKER code, which is a standard model for cross section calculations in nuclear astrophysics.

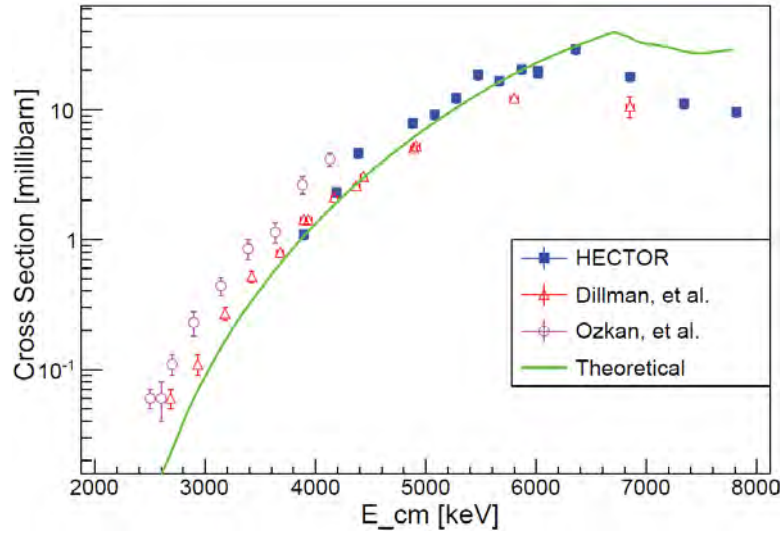


Fig. 7: Measured cross section values from this work and literature compared to theoretical values.

Conclusions

By using the gamma-summing technique, cross sections can be easily obtained and more information regarding the production of p-nuclei in exploding supernova can be found. Using HECTOR and its sum-peak spectroscopy properties, gamma-summing was completed in an experiment at the University of Notre Dame in attempts to simulate (γ, p) reactions in the supernova explosion by measuring the cross sections of (p, γ) reactions in the lab. The $^{102}\text{Pd}(p, \gamma)$ reaction was further analyzed and cross section measurements were obtained.

The cross section measurements that were acquired from the HECTOR experiment were then compared to other measurements taken by Dillman, e. al. and Ozkan, et al., as well as

theoretical values from NON-SMOKER models. The data collected kept the same overall trend as the other experimental values but more closely matched the theoretical values from 3.5-6.5 MeV and lied between the theoretical and Dillman, et al. values at energies between 6.5-8 MeV.

These new cross section measurements are to be used in network calculations that takes these measurements as parameters to simulate potential p-process scenarios and produce possible outcomes. By changing the cross sections, supernova explosions can be simulated, and the p-process scenario can be compared to observed amounts of p-process nuclei.

References

- [1] V. Foteinou, et al. Phys. Rev. C **97** (2018) 035806.
- [2] J. Audouze and J. W. Truran. The Astrophysics Journal **202** (1975) 204.
- [3] A. Simon. <https://sites.nd.edu/anna-simon/research/>, 2018.
- [4] J. Kantele. Nucl. Instr. And Meth. **17** (1962) 33.
- [5] NON-SMOKER. <https://nucastro.org/cgi-bin/tr?script=rl&table=Cross+Sections&projectile=Proton&element=pd&mass=102&massformula=FRDM&user=anyperson&pw=anypw>, (2001).
- [6] I. Dillman, et al. Phys. Rev. C **84** (2011) 015802.
- [7] N. Ozkan, et al. Nuc. Phys. A **710** (2002) 469.

Thin Film Target Preparation and Techniques for Accelerator Low Energy Nuclear Physics

Leah Clark

2018 NSF/REU Program

Physics Department, University of Notre Dame

Advisers: Dr. Ani Aprahamian and Dr. Khachatur Manukyan

Abstract

Thin film targets are an integral component of accelerator low energy nuclear physics, which help provide answers to questions relating to half-life and nuclear structure. Various techniques, including carbon floating, powder mixing, pellet pressing, and evaporation, are introduced and explained in detail for preparation for an upcoming experiment. Targets of four different isotopes of Erbium, Ytterbium, and Dysprosium were successfully created for the experiment.

Introduction

Accelerator low energy nuclear physics can provide great insight into the nuclear structure and lifetimes of heavy nuclei. However, before one can perform experiments on these nuclei to study them, one must create a target for the accelerator. Targets for studying physics can range from simply using three grams of the pure source or using special thin film targets with backing foils. In this experiment, the latter is used. The heavy nuclei of certain isotopes of lanthanides, Erbium-168, Dysprosium-162, Ytterbium-174, and Ytterbium-176, make for an interesting study that will take place at the Maier-Leibnitz Laboratory (MLL) in Munich, Germany. Because of the nature of these isotopes, thin film targets will be used in the experiment. Thin targets are widely used in low energy nuclear physics for their known success in studying nuclear reaction dynamics and nuclear structure ^[2]. The preparation of thin targets is not always an easy task and takes much consideration for each factor of the target making process. Carbon backing floating, powder mixing and pellet pressing, and finally the evaporation techniques of deposition and reduction are needed before the final targets for this experiment can be used in the accelerator. Because different types of lanthanides are used, low temperature and high temperature, different vacuum evaporators are used, a bell jar terminal evaporator and an

electron beam evaporator. The vacuum evaporator is used for the low temperature lanthanides and the electron beam for the other. The steps for the target preparation are outlined in detail as well as the successes of the targets. Similar target making techniques have been around for decades with few variations in the process; however, the challenge in this experiment was in the deposition of the high temperature lanthanides. In time, the procedure worked and multiple targets for each isotope were created in time for the experiment in Germany.

Experimental Methods

Carbon Floating

To properly conduct accelerator based low energy nuclear physics experiments, with projectile energies less than 10 MeV/u, thin film targets are often used to ensure precision. Thin film targets have a thickness ranging from minimal $\mu\text{g}/\text{cm}^2$ to hundreds of $\mu\text{g}/\text{cm}^2$ [2]. There are different techniques used to create the thin film targets before the actual evaporation technique occurs. For this experiment, carbon backing foils were used as the basis for the experimental evaporation to take place. During the actual reaction, the evaporation takes place and is attached to the carbon films, thus creating the thin film target. The carbon foils used in this experiment ranged from thicknesses of 18 $\mu\text{g}/\text{cm}^2$ to 22 $\mu\text{g}/\text{cm}^2$. To prepare the backing, first the pure carbon glass slides are cut into the shape of the desired metal target frame very carefully. The slide is then placed on a lowering machine above de-ionized water. The carbons are slowly lowered into the slightly warm water, causing the carbons to break off the glass slide and float on the water. The metal frames are then used to catch the carbons and attached the frame very carefully. This is a tricky process, as the carbons are so thin and extremely delicate. After the carbons have been backed onto the frames, they are left to dry until use for the evaporation.

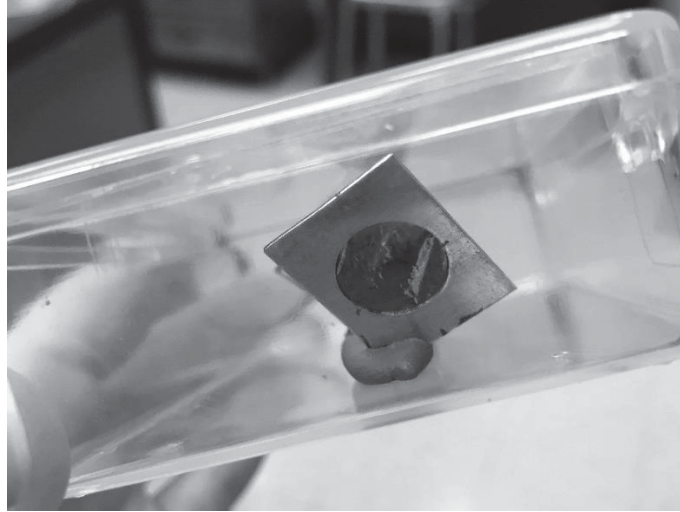


Figure 1: Finished product of a target with a carbon foil backing. The targets are placed in clay to stabilize when moved and a container to shield from contaminants in the air.

Powder Mixing

Sample preparation includes mixing the source one wants to study with a reducing agent. This experiment involves several isotopes of lanthanide elements, which is a series of metallic elements. Erbium and Dysprosium are high temperature lanthanides, meaning they have a high reduction temperature. Ytterbium is a low temperature lanthanide ^[1]. A reducing agent, which is a substance that brings about reduction by being oxidized, is needed to be mixed with the lanthanide to produce a reaction ^[2]. Hafnium is a great reducing agent and was used for all the targets. For this experiment, various milligrams of Hafnium ranging from 250mg to 415 mg were used, depending on which isotope it would be used with. The low temperature lanthanides used less Hafnium than the high temperature. Each element is measured and mixed with the right amount of Hafnium for each. Mixing takes place for about ten minutes in a crucible to get as close to homogenous as possible. The more homogeneous the powder is, the more pure and precise the evaporation can be.

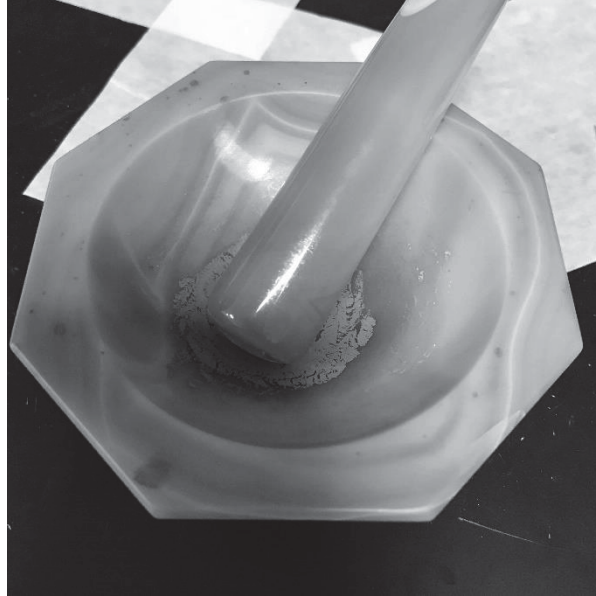


Figure 2: Mixture of Hafnium and Erbium-168 after being measured out and mixed in crucible.

Pellet Pressing

For the high temperature lanthanides, Erbium and Dysprosium, it is beneficial to press the powder into a pellet. Ytterbium was not pressed into a pellet since it is a low temperature lanthanide. Pellet pressing helps aid the reduction and the reaction because of the close contact of the materials ^[2]. Since these elements need to reach a higher temperature to reduce, the closer materials allow for less space to be taken up and heated up. The powder is pressed into a circular disk-shaped pellet using 3000-3500 lbs. of force. The pellets need to be handled with care because they are still fragile.

Vacuum Evaporators

Two different evaporators were used to conduct the experiment, a bell jar terminal evaporator and an electron beam evaporator. Both vacuum evaporators are used for the same purpose, which is to heat up a source, so it evaporates onto the target and makes it ready to use in experiment.

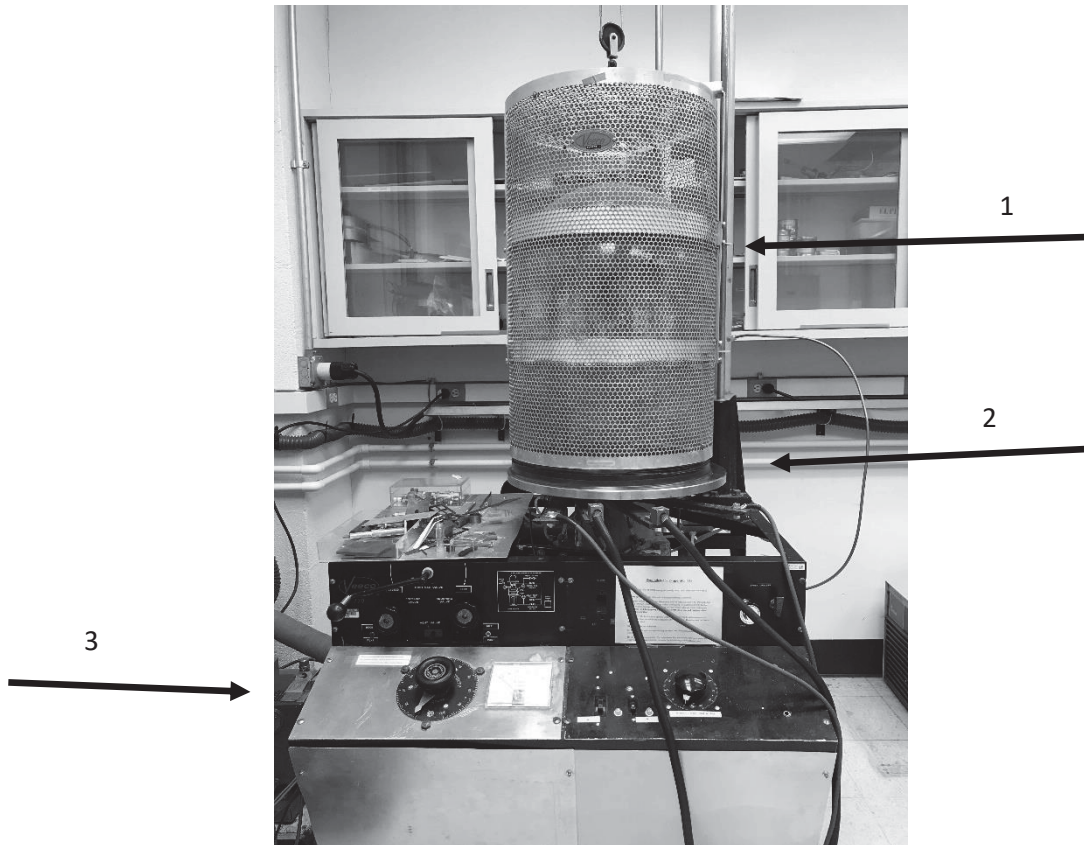


Figure 3: Bell jar terminal vacuum evaporator. 1) The vacuum shielding enclosure. The evaporation takes place inside the bell jar and is sealed after pumping. 2) The thin film targets are placed on a holder above the boat terminal at the bottom of the bell jar. 3) Controls and monitors for current that is sent through the boat.



Figure 4: Close-up of a boat terminal used for evaporation inside bell jar. The center concave dip is where the powder mixture is placed. The terminal is placed between two holders that send the current through the boat.

The bell jar terminal evaporator uses a system of pumping and heating to create the deposition onto the target, where the source is heated by a current running through the terminal. This evaporator works best for lanthanides that are low temperature, otherwise, overheating can cause the source boat terminals to break. For this reason, only the isotopes of Ytterbium were used in the bell jar. Ytterbium has a reduction temperature of 1200°C ^[1]. Using this technique, at least three targets for each isotope were successfully created, with a thickness of approximately $50\ \mu\text{g}/\text{cm}^2$. The electron beam evaporator can handle much higher levels of heat, which is why it was used for the Erbium and Dysprosium reactions, which have reduction temperatures of 1600°C and 1750°C , respectively ^[1].



Figure 5: Electron beam evaporator enclosure. The reaction takes place inside the cylinder and is monitored with voltage and position dials on the machine.

The evaporator works by having an electron beam generated from a filament and guided by electric and magnetic fields hit the source and vaporize it ^[3]. The source then is deposited onto the carbon target. This process takes several hours, since although it can reach higher temperatures, one still must pace the process as to not break anything. Both the terminals and the carbon slides are at risk of breaking if the reaction becomes too hot too quickly. After much trial and error, the electron beam evaporator technique was able to successfully create the Erbium and Dysprosium targets with 50 $\mu\text{g}/\text{cm}^2$ thicknesses.

Conclusion

In conclusion, multiple thin film targets of isotopes of Erbium, Dysprosium, and Ytterbium were crafted using different target making techniques. Evaporation using the processes of carbon floating, powder mixing and pressing, and vacuum evaporation were used. The overall trial and error process took many weeks; errors arose from carbons breaking during evaporation, carbons breaking during the floating process, inaccurate readings of temperature and thickness measurements, and overheating/underheating during the reaction. The targets will be carefully transported to the MLL in Germany to be used in further research.

References

- [1] Greene, John P, and George E Thomas. "Evaporation Techniques for Preparing Rare-Earth Targets Used in Heavy-Ion Nuclear Physics." *Physics Division, Argonne National Lab*, 19 Feb. 1991.
- [2] Thakur, Meenu, et al. "Fabrication and Characterization of Carbon-Backed Thin 208Pb Targets." *Advances in Pediatrics.*, U.S. National Library of Medicine, 2016, www.ncbi.nlm.nih.gov/pmc/articles/PMC5080559/.
- [3] "What Is E-Beam Evaporation?" *AJA International*, AJA International, Inc., www.ajaint.com/what-is-e-beam-evaporation.html.

PREPARATION OF RHINOCEROS EXTENDED GAS
TARGET FOR FUTURE EXPERIMENTS

ZACH DRENNAN

2018 NSF/REU Program

Physics Department, University of Notre Dame

ADVISORS:

Michael Wiescher

Kevin Macon

PREPARATION OF RHINOCEROS EXTENDED GAS TARGET FOR FUTURE EXPERIMENTS

Abstract

By

Zach Drennan

The Rhinoceros extended gas target (RHINO) and its crew have been assigned the tasks of observing various astrophysical reactions, using a former graduate student's thesis as a calibration. The goal for the summer was to complete various hardware upgrades along the beamline of RHINO before being some preliminary runs with beam from the 5U accelerator. The main upgrades included lead shielding, a detector stand, and a cold trap; however, there were various minor changes such as swapping piping and o-rings. The physical aspect of the project was completed, but the preliminary runs had to be rescheduled due to hardware failure.

RHINOCEROS EXTENDED GAS TARGET SETUP

Prior to my arrival, the majority of the reconstruction of RHINOCEROS (RHINO) had been done by Dr. Kevin Macon. When I began working on RHINO, the next step was to set up lead shielding (Figure 1) around the “Octopus” target chamber to shield from gamma rays produced by the proton beam provided by the 5U accelerator passing through the upstream collimators on the RHINO beam line. However, we still had to allow room for the Germanium detector to slide back and forth perpendicular to the target chamber to adjust the detection distance, so we needed to build a “lead tunnel” that provided the maximum gamma ray shielding capabilities, but also allowed for maneuverability of the detector. The series of constructions and subsequent destructions of different variations of the lead shielding lasted for about two weeks before we found an acceptable setup.

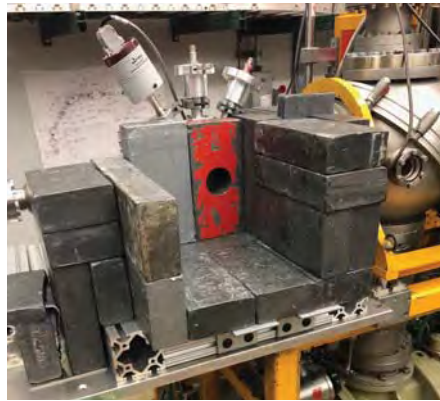


Figure 1: Lead Shielding around “Octopus” Target Chamber

During the construction of the lead of shielding, we were also constructing a sliding platform and stand for the Germanium detector that would be used for upcoming projects. The detector used had come with stand that was built in house at Notre Dame; however, the previous configuration of the stand would not allow the detector to pass far enough into the lead shielding

tunnel. Also, a sliding mechanism needed to be introduced to the stand in order to change the detector distance from the target which affects the detector efficiency. After brainstorming and drawing a few ideas for new stands, we found it was most practical to make a few modifications to the existing stand rather than construction an entirely new stand. Likewise, we decided to reuse an old sliding stand in the lab rather than creating a new one from scratch. With the configuration we selected, the detector would be vibrationally isolated from the turbo pumps which would have create a considerable amount of noise in the readings.



Figure 2: Detector Stand and Sliding Platform

Once the detector stand and platform had been finished, the next step was to assemble a cold trap in the pumping line. The reaction planned for the opening run on RHINO after the reconstruction used Neon gas as a target for a proton beam. Due to the high cost of Neon, it is important to recycle as much of the gas as possible for as many cycles as possible so the idea of the cold trap was introduced. Without the cold trap, the gas would acquire more impurities along the pumping line as it recirculated back into the target chamber. The majority of the impurities would be carbon-based originating from oil in the pumps which would cause a significant amount of noise in the gamma spectra.

The concept of the cold trap is to force the gas and impurities to flow through tubing which has been cooled to a point which the impurities will transition to a solid state and thus be trapped in the tubing while the Neon gas would continue to flow towards the target unaffected by the change of temperature in terms of state transitions due to its significantly lower transition temperatures. More specifically, our setup used coiled copper tubing as the trapping location for impurities and stainless steel as entry and exit tubing (figure 3). The copper portion on the setup and part of the stainless steel would be submerged into a dewar of liquid nitrogen to keep the copper at the desired temperature to keep the impurities from returning to a gaseous or liquid state (figure 4).



Figure 3: Assembled cold trap tubing



Figure 4: Cold trap mounted to pumping line

In preparation for the opening run on RHINO, there were some calculation that needed to be done in order to choose the appropriate collimators for measuring released gamma rays during reactions. The first calculation that needed to be done was and estimate of particles per second that would react with the target using Rutherford scattering as a model. I created a spreadsheet in Excel in which we adjust collimator size, angle of measure, and mass numbers of the scattering particles. With this spreadsheet, we were able to choose collimators which would provide a rate close to 5000 particles per second. The next estimate that needed to be done was the energy loss of beam energy compared to the pressure of the gas chamber to understand how critical it was to keep the chamber as close to vacuum as possible. SRIM was used to make a model of some of the reactions planned for the future, and the data was analyzed in Excel. From the SRIM simulations at different pressures, it was found that the average loss of the beam was linearly proportional to the pressure inside the target chamber (Figure 5).

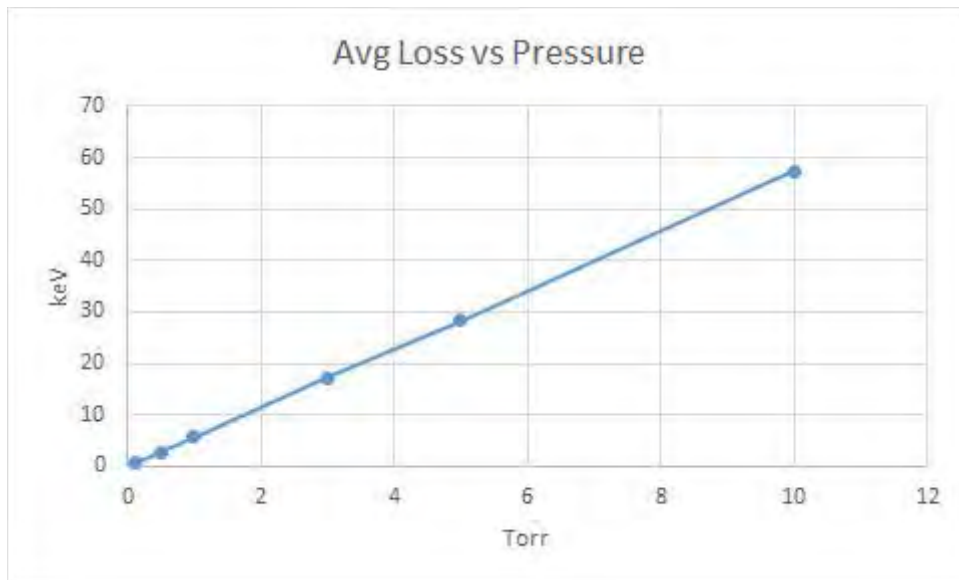


Figure 5: Average loss of beam energy vs pressure

ANALYZING MAGNET FAILURE

On the first day of beam access for the RHINO project, we sat down at the control station after preparing the 5U accelerator and beamline for a calibration run only to notice the bright red figure of the analyzing magnet on the control panel. After a short investigation and much frustration, it was found that there had been at least six transistors blown in the power supply of the analyzing magnet (Figure 6). We were then informed that the parts were not repairable in house and would have to be ordered. This meant that the accelerator could not be used during our allotted time and thus the project has been delayed until well after the REU concludes.

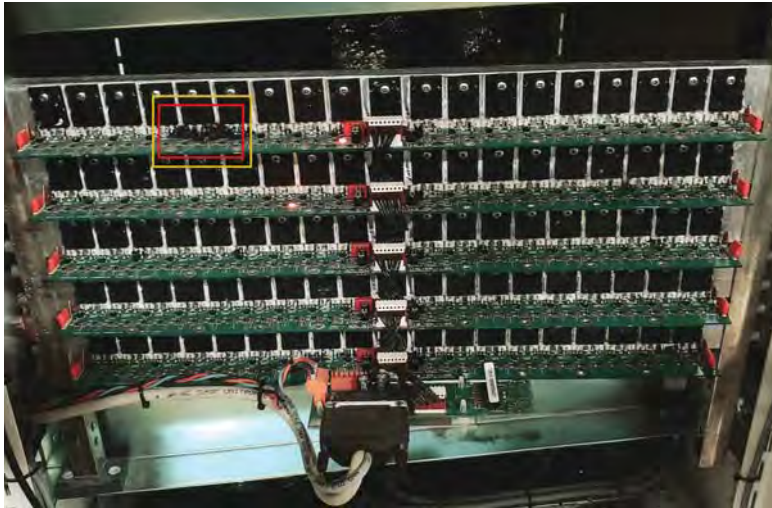


Figure 6: Damage on boards of power supply

CONCLUSION

While we were unable to complete the entirety of the project in the ten weeks I was here, we still managed to make great progress on the RHINO project. On an individual level, I was able to experience the day to day life inside of Nuclear Physics lab while slowly acquiring new skills relevant to the field. Even though I will be leaving the lab without a magnum opus to hang my hat on, I am still proud of the work we did accomplish.

Using Particle-Induced Gamma-Ray Emission
Spectroscopy to Detect Fluorinated Substances in
Personal Care Products

Emi Eastman

2018 NSF/REU Program

Physics Department, University of Notre Dame

Advisor: Graham Peaslee

Abstract

Per- and polyfluoroalkyl substances (PFASs) are known environmental contaminants linked to cancer and other adverse health effects. These compounds have applications in a wide variety of products, including personal care products. PFASs in cosmetics—specifically mascara and lipstick — can travel into the eyes and mouth and increase chances of human exposure. We measured total fluorine in 232 cosmetics using particle-induced gamma-ray emission (PIGE) spectroscopy. PIGE offers an efficient technique to detect the presence of fluorine involving minimal analysis time compared to traditional methods. We found that 50% of all the cosmetic samples contained fluorine, including 92% of waterproof mascaras and 89% of liquid lipsticks. A subset of 8 samples are currently being sent to our collaborators at Oregon State University to identify which fluorinated compounds are in our samples.

Introduction

Per- and polyfluoroalkyl substances (PFASs) is a general term for approximately 3,000 different chemicals. These substances have surfactant properties, making them extremely useful in formulating water-, grease-, and stain- repellants. Common applications of PFASs include food packaging, non-stick pots and pans, firefighting foams, and soil and stain repellent carpets and textiles.³ They are resistant to biodegradation and hydrolysis, making them extremely stable in the environment.⁴ PFASs have been found in the air and water, and they bioaccumulate in animals, including humans.⁵ As discarded products sit in landfills, PFASs seep into the ground—eventually contaminating the groundwater. PFASs remain intact in water and persist into drinking water. Other sources of human exposure include dust inhalation—particularly dust kicked up indoors from carpets—as well as inhalation of contaminated air.⁴ Human exposure has

been linked to an increased risk of testicular and kidney cancer, liver and fertility damage, and other adverse health effects.⁴ The presence of PFAS in consumer products increases the chances of human exposure and threatens the safety of consumers.

Personal care describes a category of items used to maintain one's appearance, health, or well-being. Fluorinated surfactants have been used in hair care products, specifically conditioners, to make hair oleophobic and easier to brush.³ These products are generally more invasive, with most coming in direct contact with the body. While cosmetic ingredient lists are available, they are poorly regulated and often misleading. We found that a significant portion of cosmetics with measurable amounts of fluorine did not list fluorochemicals as ingredients. Cosmetics constitute the bulk of personal care products and have millions of users worldwide. Mascaras and lipsticks pose the greatest danger to humans due to the possibility of ingestion through the mouth or exposure through tear ducts in the eye. Face makeup and other cosmetics tend to just sit on the skin, with less of a chance of invasive exposure.

Particle Induced Gamma Ray Emission (PIGE) spectroscopy is a common type of ion-beam analysis. Gamma spectroscopy is advantageous in that it can be done with high precision and high resolution.¹ A sample is bombarded with protons, which excites the nucleus of any element present when the Coulomb barrier is overcome. The composition of a sample can be deduced from the analysis of gamma ray emissions from the excited nuclei. PIGE requires minimal data analysis time and is a nondestructive technique, making it superior to traditional methods when screening for the presence of PFAS in products.⁷ Because of the Coulomb barrier, PIGE is most efficient and effective when looking for lighter elements—making fluorine detection an ideal application.⁶

Materials and Methods

We collected 235 cosmetics from an Ulta Beauty store in Mishawaka, IN. We separated these samples into 6 groups in order to represent the most commonly used cosmetics available: mascaras, eye-makeup, liquid lipsticks, cream lipsticks, face makeup, and skin care. Each product was painted onto a sheet of fluorine-free filter paper in order to create a target. We cut out a small piece of each sample—using methanol-rinsed scissors to prevent contamination—and mounted it to a stainless steel target-holder with fluorine-free tape. Each target-holder has a 0.5-inch diameter hole where the ion beam hits the sample. We mounted the target-holders to a target wheel—an apparatus that attaches to the end of the beamline and holds 60 target-holders at a time. The target-wheel allows us to quickly switch between targets and reduces downtime between runs.



Figure 1: Target wheel



Figure 2: Modified Alphasross Ion Source

We used a modified Alphasross ion source to generate a proton beam. The source uses radiofrequency (RF) oscillations and charge exchange to create negative ions. We leak hydrogen gas into a quartz bottle, and the gas turns into a plasma using an RF oscillator. The beam travels through vaporized rubidium atoms, where it gains electrons and becomes negatively charged. The beam enters St. Andre, the 3 MV tandem accelerator at the University of Notre Dame. The negative



Figure 3: St. Andre 3MV Tandem Accelerator

ions are attracted to the positive terminal in the center of the accelerator. A stripper foils strips the beam of its electrons, and the now positive beam is accelerated away from the positive terminal. Then, two sets of two quadrupole magnets are used to focus the beam—one when the beam first exits the accelerator and another near the end station. A third set of dipole magnets bends the beam 90 degrees toward the end-station. The beam is brought through a thin Kapton window (~8 microns) into air, where the target wheel sits along with a high-purity germanium detector.

For this study, we exposed each sample to ~30 nA of 3.4 MeV protons in air for 180 seconds. If the sample appeared not to contain fluorine, the time was shortened to 60 seconds. A tantalum collimator near the beam exit was used to normalize the amount of beam on target from day to day. Fluorine has characteristic gamma rays at 110, 197, 1236, 1349, 1357, and 1459 keV. At 3.4 MeV, the gamma ray yields at 110 and 197 keV are significantly higher than the others.² Therefore, we focused on measuring those two peaks. Since PIGE is not selective, the beam excites every element present in the sample if it overcomes the Coulomb barrier. Other common

peaks found in the cosmetics included aluminum (171, 844, and 1014 keV) and sodium (440 and 1369 keV).² We used a data analysis code to convert peak integrations to tantalum-normalized counts per microcoulomb. Our collaborators at Oregon State University are analyzing samples with significant fluorine counts in order to determine the exact chemical composition of the sample.

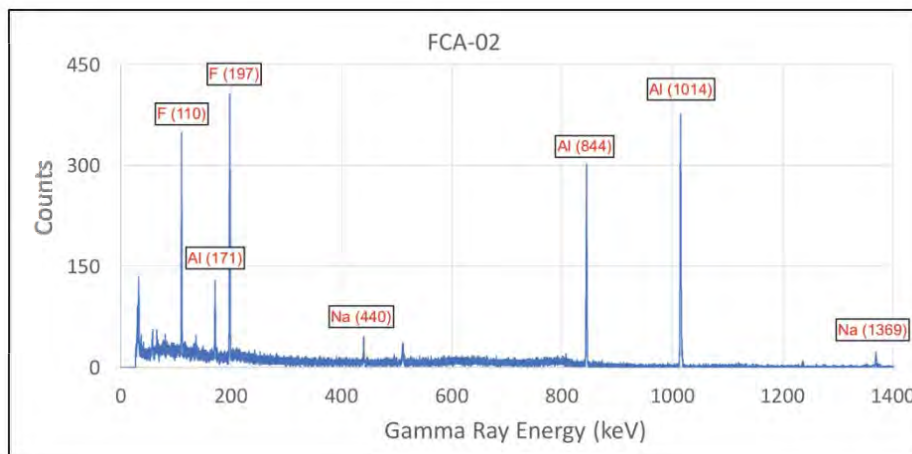


Figure 4: Gamma ray peaks observed in a mascara sample. We detected fluorine, as well as sodium and aluminum.

Results and Discussion

We detected fluorine in 54% of the 235 products that we tested. High counts of fluorine were most frequently found in waterproof mascaras and liquid lipsticks. Waterproof mascaras ranged from 4,585 to 679,812 counts/ μ C and liquid lipsticks ranged from 267 to

category	number of samples tested	number of brands tested	% with F
mascaras	29	19	79
eye makeup	48	14	56
lipsticks	56	26	70
face makeup	59	21	51
other	43	11	26

Table 1: Percentages of Personal Care Products Containing Fluorine

7939 counts/ μC . Overall, cosmetics marketed as “water-resistant” or “long wearing” were found to be more fluorinated than others.

We sent a subset of 8 samples to our collaborators at Oregon State University to identify the specific fluorinated substance in the samples. The subset consists of three highly fluorinated mascaras, one fluorine-free mascara, three highly fluorinated liquid lipsticks, and one fluorine-free liquid lipstick. We are awaiting results.

We know of one common fluorinated ingredient in cosmetics. Synthetic mica is a stable form of mica—a natural mineral that adds sheen—with inorganic fluoride added. It was most commonly found listed as an ingredient in face makeup and eyeshadows. We found no fluorinated substances on the ingredient lists of the 8 products, including synthetic mica. We suspect that there is either a PFAS in the sample, or an issue with the way cosmetics ingredients are disclosed, or both. The presence of PFAS is an obvious health risk to consumers, increasing the chance of human exposure. If a safer, unlisted fluorinated substance like synthetic mica is present, there is an issue with regulating cosmetic labeling. The lack of transparency could negatively affect a consumer unaware of the contents of a product.

The detection of fluorine in personal care products helps to demonstrate the efficiency and effectiveness of the PIGE spectroscopy technique. In one summer, a large survey of products was completed, and two types of personal care products likely to be of concern were identified for further study. These results will likely result in a publication in the next year. Future projects include detection of PFASs in contaminated soils, aerosols, firefighting turnout gear, and bodies of water. PIGE has the potential to identify sources of environmental and human hazards.

Acknowledgements

Thank you to the Umesh Garg and Lori Fuson of University of Notre Dame and the National Science for funding and organizing this research experience. Thank you to John Wilkinson, Ashabari Majumdar, Sean McGuinness, Mallory McCarthy, Alec Gonzales, and Briana Linton for assistance in data sampling and analysis. Lastly, thank you to Graham Peaslee for the constant guidance, encouragement, and fun throughout this program.

References

- (1) Krane, Kenneth S. *Introductory Nuclear Physics*. 1988.
- (2) Kiss, Á. Z., Koltay, E., Nyakó B., Somorjai E., Anttila A., Räsänen, J. *Measurements of Relative Thick Target Yields for PIGE Analysis on Light Elements in the Proton Energy Interval 2.4 – 4.2 MeV*. 1984.
- (3) Kissa, E. *Fluorinated Surfactants and Repellants: Second Edition, Revised and Expanded*. 2001.
- (4) U.S. Department of Health and Human Services, *Agency for Toxic Substances and Disease Registry. Toxicology Profile for Perfluoroalkyls, Draft for Public Comment*. 2018. 2-6
- (5) Marie Pierre Krafft, Jean G. Riess, *Per- and polyfluorinated substances (PFASs): Environmental challenges*. 2015.
- (6) M.J. Kenny, J. R. Bird and E. Clayton. *Proton Induced γ -ray yields*. 1980.
- (7). M. Volfinger. *Quantitative analysis of the fluid inclusions by particle-induced gamma-ray emission*. 2002.

On the Effect of Increased Luminosity on Stubs per Jet and Algorithm Efficiency

Brooke A. Emison

University of Central Florida

Abstract

During the third long shut down of the LHC, the upgrades will include an increase of luminosity. With this upgrade, the CMS detector must handle a greater number of proton-proton interactions which will have a significant impact on its level-1 trigger system. This study helps analyze the effect of increased luminosity on the L1 track trigger upgrade, especially on measurements in jets, where tracker occupancy is highest. It uses simulated data to measure the efficiency of the algorithm used to identify particle tracks. This study compared the results with no pileup and 200 pileup. The results suggest that efficiency is roughly the same, with slight dips near jet axes and that the number of track trigger primitives (“stubs”) in jets is drastically higher with the increase in particle pileup.

On the Effect of Increased Luminosity on Stubs per Jet and Algorithm Efficiency

With a circumference of 27 km and max speeds of $0.999999990c$ (or 3 m/s slower than the speed of light), the Large Hadron Collider is the world's largest particle accelerator. The collisions of particles are actually collisions of bunches of particles. All but very few of the particles in these bunches do not collide and instead create what we call pileup. The LHC will complete its third long shut down by 2026. This upgrade will include an increase in luminosity, which will be the focus of this paper. The Compact Muon Solenoid detector looks specifically at proton-proton collisions, serving a wide range of physics, including the search for the Higgs boson.

The upgrade to the LHC will drastically increase the number of interactions the CMS detector has to handle. The luminosity increase means more protons will be included in the bunches of particles the LHC collides. Because these additional proton-proton interactions, which increase pileup, are far too numerous to be stored, a multi-level triggering system filters out and only saves interesting data. The increase in particle production rates due to higher luminosity makes identifying important data much more difficult. Level one of the triggering system (L1 Trigger) is “an extremely fast and wholly automatic process that looks for simple signs of interesting physics”^[1]. This is the focus of this paper.

The L1 tracker has six barrel layers and five end cap layers. When a particle passes through a layer, it deposits energy onto the detector. This information, known as a stub, can be used later to reconstruct the particle path, or track. This is done by connecting all the stubs for one particle. The L1 trigger sorts through all this data and picks out what we believe is interesting. The track trigger is an upgrade to the trigger system that will help with the increase in luminosity. The algorithm that the CMS group uses to create tracks from stubs, also called

seeds, will be referred to as the seed-track algorithm. It is limited by the design of front end electronics; we call these front end inefficiencies. This paper examines the effect of front end inefficiencies on the performance of the track trigger.

This paper analyzes how the increase in luminosity affects the number of stubs the detector identifies in jets, where particle density is largest, due to a cascade of particles decaying in sequence, creating a cone of many particles. A stub is considered part of a jet if it is within 0.4 radial distance from a jet axis. To calculate the radial distance, we use $\Delta r = \sqrt{\varphi^2 + \eta^2}$.

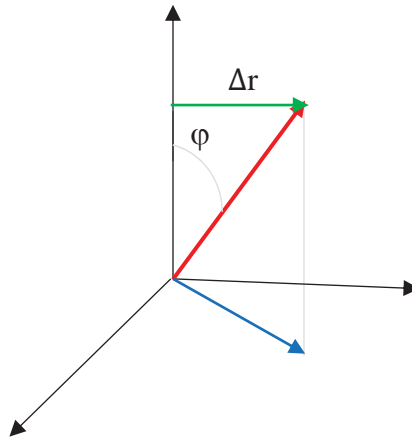


Figure 1. A diagram of a jet axis and the radius from the jet axis to the stub, which is the smallest radius from the jet axis.

Methods

The software CMSSW, versions 9.3.2 and 9.3.7 were used to create simulated data to analyze. The samples used to create the data were:

TTBar PU0: /RelValTTbar_14TeV/CMSSW_9_3_7-93X_upgrade2023_realistic_v5_2023D17noPU-v2/GEN-SIM-DIGI-RAW

TTBar PU200: /RelValTTbar_14TeV/CMSSW_9_3_7-PU25ns_93X_upgrade2023_realistic_v5_2023D17PU200-v1/GEN-SIM-DIGI-RAW

TTBar PU300: /RelValTTbar_14TeV/CMSSW_9_3_7-PU25ns_93X_upgrade2023_realistic_v5_2023D17PU300-v1/GEN-SIM-DIGI-RAW.

The samples were analyzed with code written in C++ and then passed through a C++ macro to create histograms. The plots compared efficiency of the algorithm with front end inefficiencies both on and off. To do this, first I plotted the number of tracks found with front end inefficiencies on vs off with separate plots for pileup and no pileup. Then I calculated the efficiency with front end inefficiencies on divided by the efficiency with front end inefficiencies off to see if the differences in the tracks found were just small, but still significant. The purity ratio was also calculated, which shows how well the algorithm did in accuracy.

I also created histograms that showed the difference in stubs per jet with and without pileup. This was done by first calculating which stubs were part of a jet, and then creating plots for each separate layer. This allows stub loss to be identified. Finally, I created histograms displaying the momentum in each jet for the whole L1 trigger as well as for each layer, with separate plots for pileup and no pileup.

Results

The plots of number of events with a specific number of tracks per event are shown below. The first plots (Fig. 2-3) show $p_T > 2\text{GeV}$. The second (Fig 4-5) show $p_T > 10\text{GeV}$. It is clear, especially from the mean, that the plots are extremely similar. The only plot with minute differences is the highest energy plot with pileup (Fig. 4).

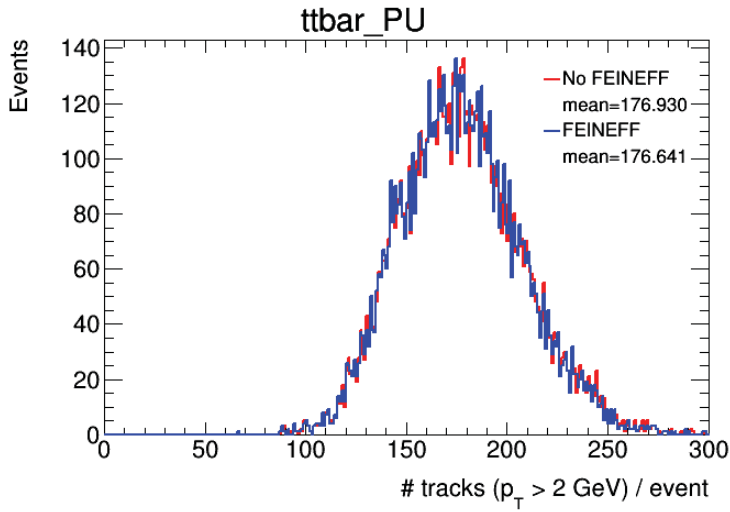


Figure 2. The number of tracks found with front end inefficiencies (FEINEF on vs off. With Pileup (PU), $p_T > 2\text{ GeV}$)

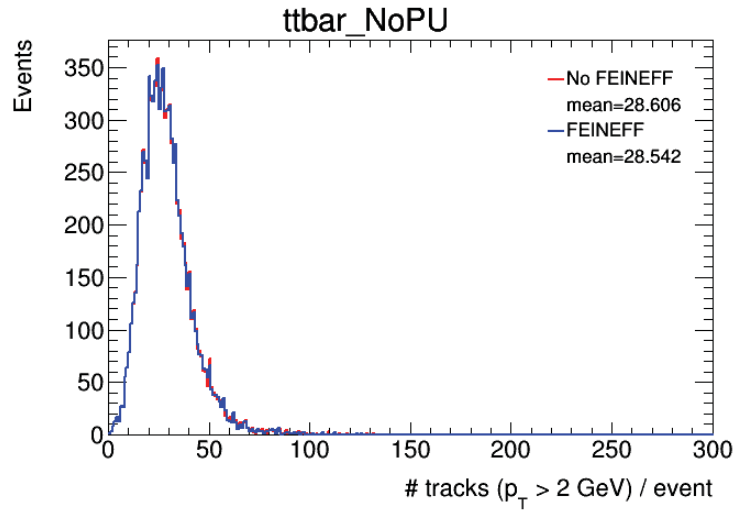


Figure 2. The number of tracks found with front end inefficiencies (FEINEF on vs off. Without Pileup (PU), $p_T > 2\text{ GeV}$)

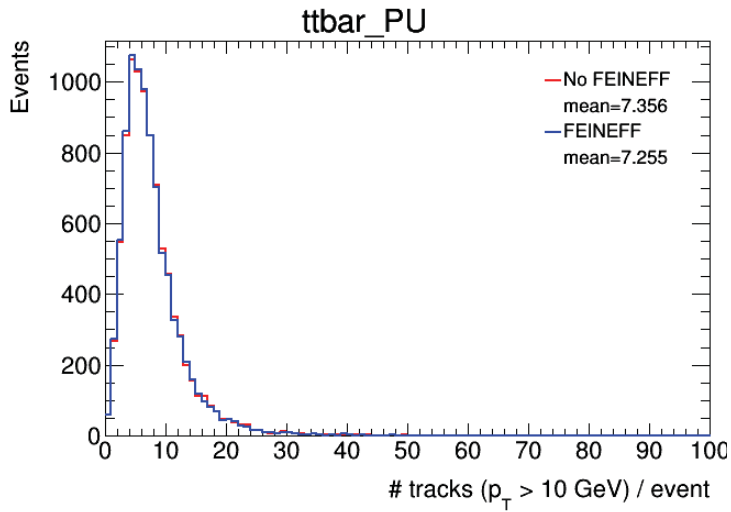


Figure 4. The number of tracks found with front end inefficiencies (FEINEF on vs off. With Pileup (PU), $p_T > 10\text{ GeV}$)

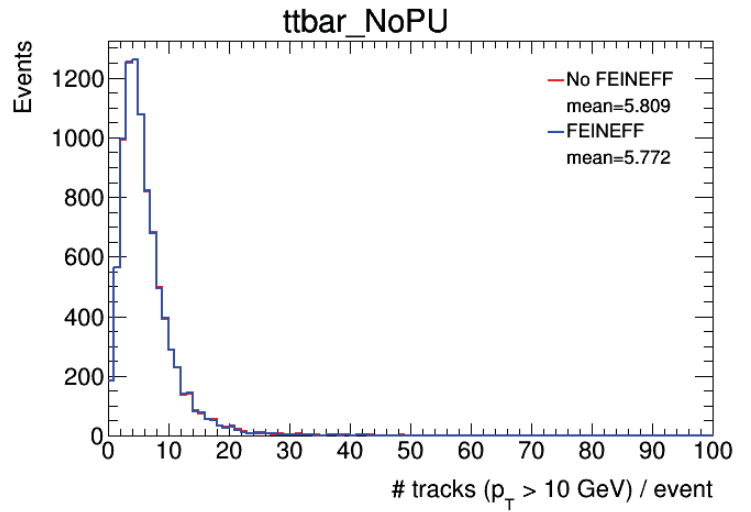


Figure 4. The number of tracks found with front end inefficiencies (FEINEF on vs off. Without Pileup (PU), $p_T > 10\text{ GeV}$)

The next two plots (Fig. 6-7) are ratios of efficiencies with front end inefficiencies on and off. Although there are dips, these ratios are all roughly equal to one, showing no loss in efficiency.

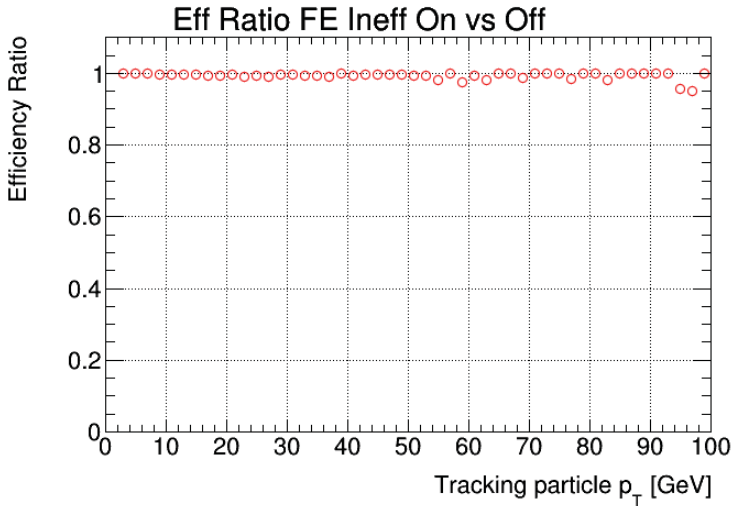


Figure 6. The ratio of efficiency with front end inefficiency on vs off of tracking particle p_T

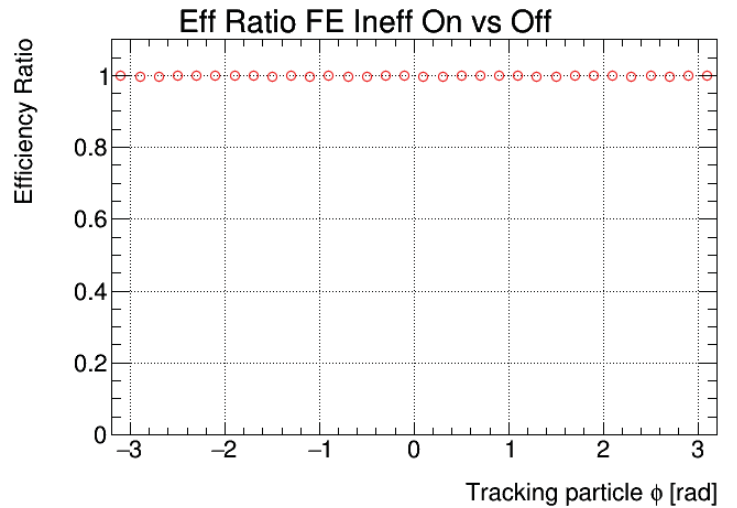


Figure 7. Figure 6. The ratio of efficiency with front end inefficiency on vs off of tracking particle ϕ

This plot (Fig. 8) is the last of the ratios of efficiencies. It shows the ratio near the jet axis and is the only plot with a clear loss in efficiency.

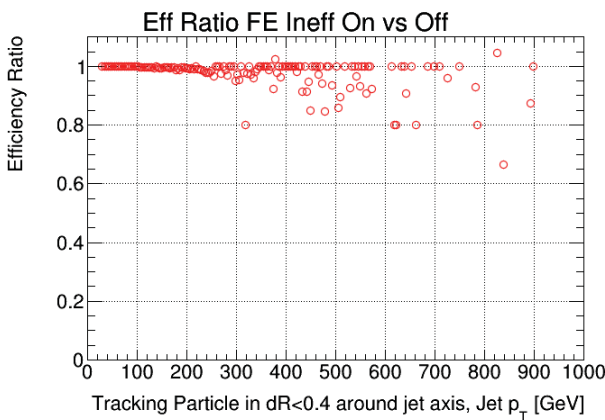


Figure 8. The ratio of efficiency with front end inefficiency on vs off of tracking particle within 0.4 of the jet axis

Figure 9 shows stubs per jet with front end inefficiencies on and off and with and without pileup. There is not any significant difference between front end inefficiencies on and off, however there

are significantly more entries in pileup than in no pileup. Figure 10 shows momentum in each jet vs how many stubs that jet has. Pileup 200 and no pileup are superimposed on the plot.

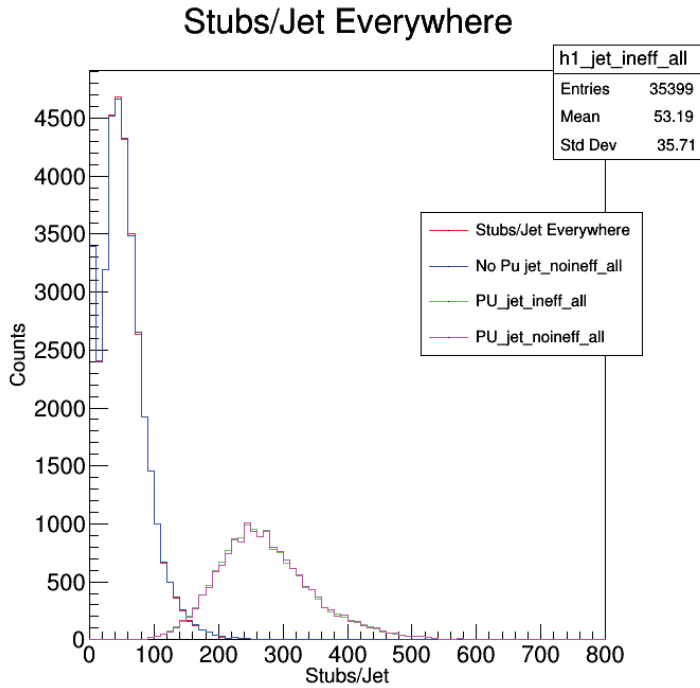


Figure 9. Count of jets with given number of stubs per jet. Front end inefficiencies on and off, pileup and no pileup

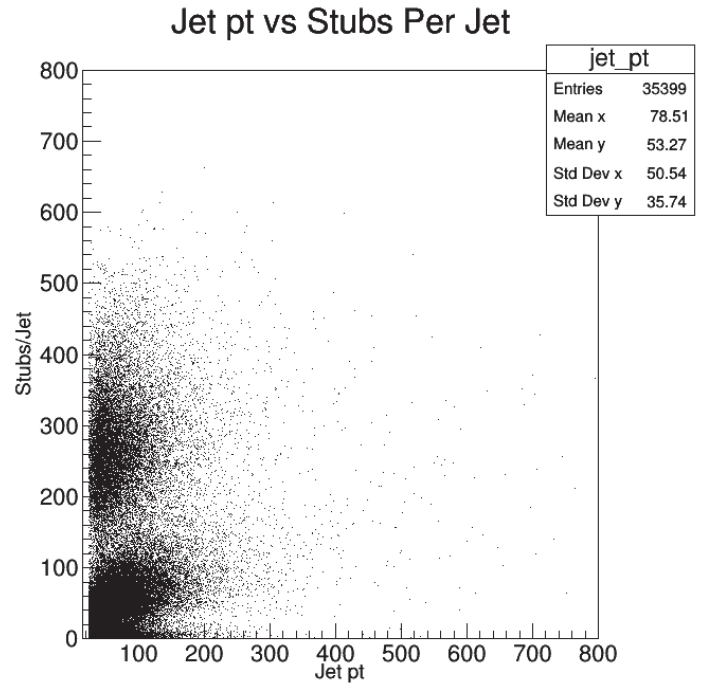


Figure 10. Jet momentum vs number of stubs in the jet.

Discussion and Conclusions

Overall, the plots of efficiencies and number of tracks (Fig. 2-8) showed that there were no major limitations of the hardware of the CMS with the new upgrade. This was an overall positive find. The fact that the only difference was near the jet axis was expected, because this is where the detector may become the most overwhelmed.

The difference in the peaks of stubs per jet between pileup and no pileup shows that neither the electronics nor the algorithm becomes saturated and cannot handle more. If this were true, we would see a cutoff of max stubs per jet, which we do not. Figure 9 also shows just how

many more stubs there are to handle with the increase in pileup. Figure 10 shows jet momentum as a function of stubs per jet and is about what is expected.

References

- [1] Triggering and Data Acquisition. (n.d.). Retrieved from <https://cms.cern/detector/triggering-and-data-acquisition>

Simulating an Interdependent Network of Fibroblasts and Heart Cells

Rebeckah Fussell

2018 NSF/REU Program

Physics Department, University of Notre Dame

Advisor: Dervis Can Vural

July 27, 2018

Abstract

Fibroblast cells secrete diffusive chemicals known as Cooperative Factors (CFs) that work against the mechanisms that cause cell death in both fibroblasts and heart cells. Additionally, a network of beating heart cells in a fluid can stimulate flow that aids in the spread of CFs. This project presents a model for a system where heart cells and fibroblasts operate in a mutually dependent manner: the cooperative factors secreted by the fibroblasts delay the deterioration of the heart cells, and the heart cells mechanically support the spread of CFs among the fibroblasts and back to the heart cells. This project simulates the spread of diffusive CFs from fibroblast cells, and finds that flow of CFs throughout the system can be stimulated by a range of sinusoidal heart cell behaviors.

1 Introduction

Complex life forms, such as animals, are comprised of networks of different cell types. These cells work with other cells of the same type, forming a tissue that performs a particular task. These cell groups also work with tissues networks of other cells types, with each type of cell tissue performing a function that together allows for complex life forms. In complex life forms such as animals, no single cell type alone can be considered fully alive (for instance, a beating heart tissue would not stay alive for long without other cell types performing the functions that keep the heart cells alive). Thus different types of cells are not only dependent on others of that cell type to perform the functions of those cells, and cells are dependent on other cell types

to perform complementary functions. While this sort of complex interdependence is exhibited throughout the animal kingdom and in other life forms such as plants, building a network of living cells that exhibit this sort of interdependence is difficult as it requires deep understanding of the function of the cells. This project proposes a simple model for this type of dependent self-sustaining system that could be built in the lab.

Of course, cell networks cannot be self-sustaining forever: all cells must die. Previous work in cell aging and death has shown that, while there are mechanisms on the individual cell level that cause aging, the complete network of cells plays a crucial role in aging.[1] When the neighbors of a cell fail, the cell itself is more likely to fail. It is possible to describe cell aging and death within a tissue network with a simple mathematical model, and this model applies to cell networks regardless of how various types of cell networks are formed.[2]

A study on the effects on interdependence theory has shown that existing models of diffusion and cell death , when solved in simulations, match well with experimental results.[3] In this project, I used an adapted version of the equations in that study.

Figure 1 illustrates a cross section of the proposed model for a simple interdependent system of heart cells and fibroblasts. On the left side is a bulb that can be contracted and expanded by the network of heart cells attached to the bulb's surface. The change in volume of the bulb induces oscillatory flow in the pipe on the right side of the cross section, where fibroblasts that secrete CFs are attached to the edges of the tube. The focus of this report is on simulating the chemical concentration of CFs in the at different points in the pipe.

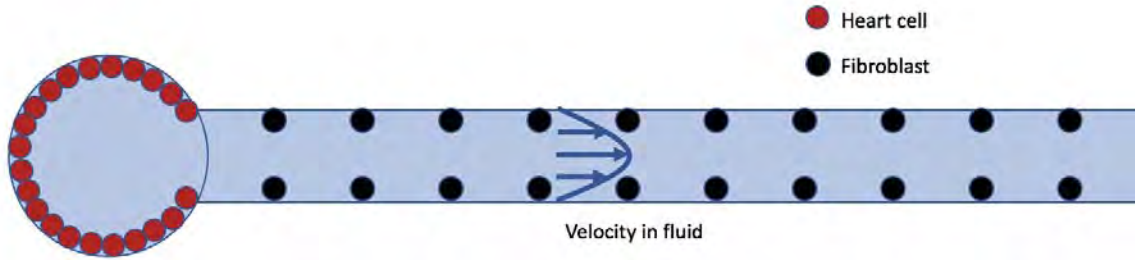


Figure 1: Two-cell type interdependent system. Heart cells beating in the bulb stimulate flow. The focus of this report is the concentration of CFs in the pipe lined with fibroblasts, and how it is influenced by the flow.

2 Methods

The simulation was built on a system of two differential equations that together describe the behavior of diffusive cells in a moving fluid. As the cooperative factors are diffusive, I use a modified version of the diffusion equation:

$$\frac{d\phi}{dt} = D\nabla^2\phi + \vec{v} \cdot \vec{\nabla}\phi + sn - \gamma\phi \quad (1)$$

In eq. 1, the first term on the right hand side simulates the diffusion of the CFs into the fluid, the second term is an advective term that incorporates velocity of the fluid into the simulation, and the third term provides the source of CF, the fibroblast cells, expressed as a position-dependent function n . The fourth term causes the decay of CFs in the fluid.

The death rate of cells (dependent on the concentration of CFs ϕ) is governed by

the equation

$$\frac{dn}{dt} = -\frac{\phi_0}{\phi + \phi_0}n \quad (2)$$

where n represents the cells, as in eq. 1, and ϕ_0 is a constant that sets the rate of cell death.

Since the heart cells were not simulated in this particular project, the oscillations generated by the contractions in the bulb were approximated by setting the velocity equal to

$$\vec{v} = v_{max}\left(1 - \frac{y^2}{R^2}\right)\cos\left(\frac{2\pi}{T}t\right)\hat{x} \quad (3)$$

where v_{max} is the maximum velocity, R is the radius of the tube in the vertical direction, and T is the period of oscillation. It is assumed that the contractions of the bulb only move fluid in the horizontal direction, as in a pipette. The parabolic factor of eq. 3 represents the behavior of fluid in a tube, where the velocity decreases near the edges of the tube.

This equations were solved at discrete time steps across a mesh, using finite element methods using the software Freefem++, then plotted in MATLAB. The mesh was a grid of size 20*1200 and the time steps were of size 0.01.

3 Results of Simulations

Figure 2 shows a simulation at the beginning, middle and end of a single run. At the beginning of the simulation, the concentration of CFs is focused on the area immediately surrounding the cells, in a two dimensional gaussian pattern. After the simulation runs for awhile, at $t= 5.0$, the concentration of CFs immediately

surrounding the cells has decreased as cells have aged in accordance with eq. 2. The chemical begins to form bands between cells on opposite sides of the tube as the chemical concentrates in the middle of the tube. The oscillations of the fluid continue, and by $t = 10.0$ the concentration of chemical begins to approach a constant value throughout the tube, at a value that is approximately one tenth of the initial maximum value. While the rates of diffusion and cell and chemical decay depend on the exact parameters (such as the values of D and ϕ_0), this basic behavior is displayed across a wide range of parameter values.

Due to the cell death behavior described by eq. 2, cells die in an approximately exponential fashion, $n \approx n_0 e^{-kt}$, where n_0 is the initial cell population and k is the decay rate. An example exponential fit can be seen in fig. 3. In fig. 4a, the decay rate is shown for a range of velocity oscillation amplitudes and periods. The fibroblast cells decay faster at higher maximum velocities, which is initially surprising because higher velocities allow the fluid to move throughout the geometry. However, while this greater spread of fluid will likely increase transport of CFs to the heart cells in the bulb, it takes CFs away from the fibroblast cells that secrete them, thus slightly increasing the rate of cell death for those fibroblasts. This is illustrated in fig. 5, which demonstrates that when the oscillations due to the heart cells are removed from the simulation entirely, the decay is slightly slower. Figure 4b shows that the ideal oscillation period to prolong fibroblast cell decay is between 0.3 and 0.4, though the rate of decay does not increase much beyond this ideal value between $T = 0.4$ and $T = 2.0$, which is the range of normal heart beats.

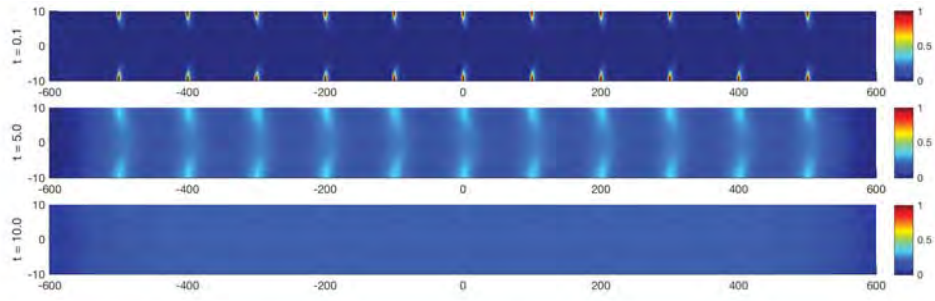


Figure 2: Concentration of cooperative factor in the tube at $t = 0.1$, $t = 5.0$, and $t = 10.0$. The domain represents the tube section of fig. 1

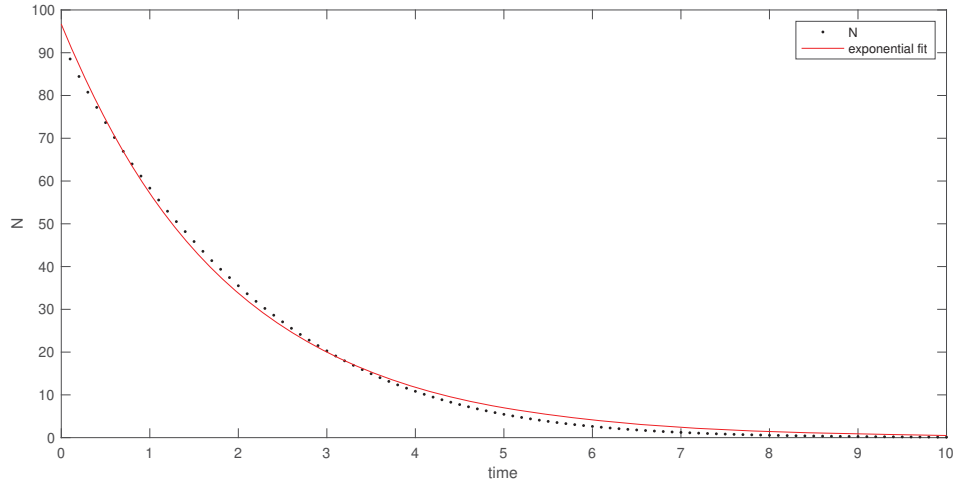


Figure 3: Decay of cells (represented by variable n) over time with exponential fit.

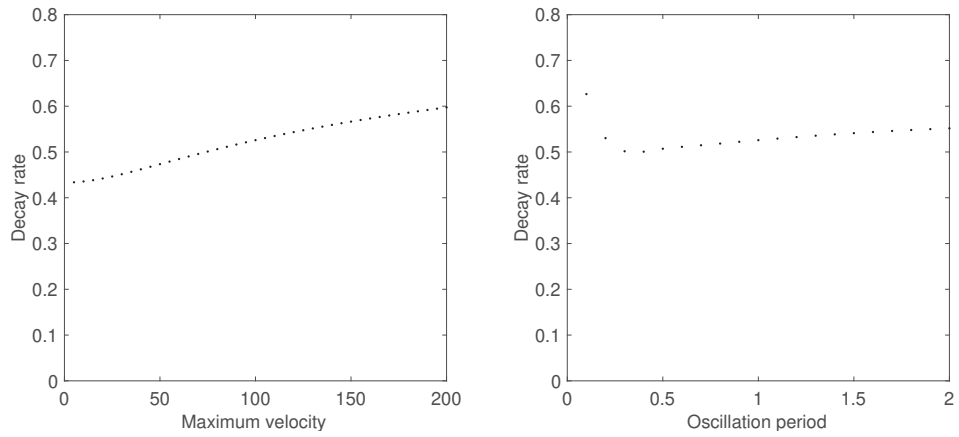


Figure 4: a) Decay of cells for a range of oscillation periods. b) Decay of cells for a range of maximum velocities.

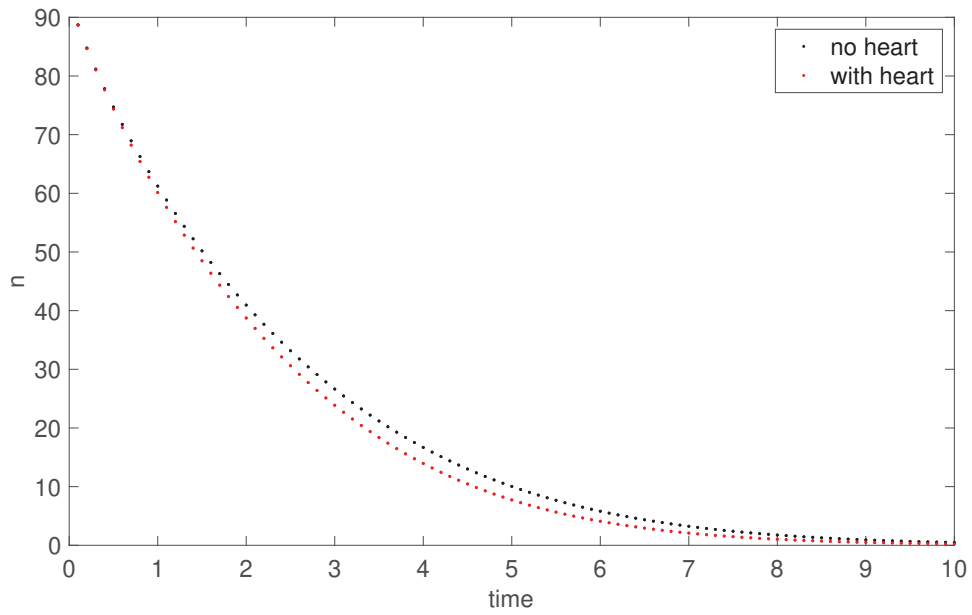


Figure 5: Fibroblast decay with and without heart cells. For the data with heart cells, $v_{max} = 50$.

4 Conclusion

The main result of this project is that the simulations show that, across a range of parameters pertaining to rate of diffusion and aging in the fibroblast cells, heart cells can mechanically provide the stimulus for a spread of cooperative factor through a region and back to the heart cells themselves, provided that the heart cells exhibit a sufficiently high-amplitude sinusoidal flow in the fluid of the tube. While the flow of CFs to the heart cells is likely to work against death in the heart cells, there is a small cost to the long-term survival of the fibroblasts, as they lose some of the CFs in their proximity due to the flow. The next step for this work is to expand the simulation to include a simulation of the heart cells in the bulb. Such a simulation would replace the assumed sinusoidal velocity term in this report with the actual resultant velocity of one of the models for simulating heart cell networks. A simulation of this type is described in Liu Baiting's REU research paper in this book.

Another step is to build an experimental version of the system of fibroblasts and heart cells described in this report, measure the rate of cell and chemical decay, and compare the experimental results to the simulations described in this and Liu Baiting's report. Completion of a functioning experiment of this system would mean the creation of a system of two cell types created in the lab that are dependent on each other to stay alive for a longer period of time, which is progress in the study of prolonging cell life in laboratory settings, and could lead to research into the exact nature of the interdependence of different types of cell networks within a larger system or organism.

References

- [1] Acun A, Vural DC, Zorlutuna P. (2017). A tissue engineered model of aging: interdependence and cooperative effects in failing tissues *Sci. Rep.* 7, 5051.
- [2] Vural, DC., Morrison, G., Mahadevan, L. (2014). Aging in complex interdependency networks. *Phys. Rev. E*, 89(2), 022811.
- [3] Suma, D., Acun, A., Zorlutuna, P., Vural, D. C. (2018). Interdependence theory of tissue failure: bulk and boundary effects. *Royal Society Open Science*, 5(2), 171395.

Bend Consistency Cut Performance in the CMS
Detector L1-Trigger Upgrade

Author: Kevin Greif

2018 NSF REU Program

Physics Department, University of Notre Dame

July 27, 2018

Advisors: Kevin Lannon, Michael Hildreth

Abstract

As the Large Hadron Collider (LHC) upgrades to higher luminosity, more performance is demanded from the L1 Trigger system. An upgrade to the L1 Trigger known as the Track Trigger will provide this performance by incorporating data from the tracker into the L1 Trigger system. This requires quickly reconstructing the paths of particles using only the processing power available on Field Programmable Gate Arrays (FPGA). Given these limited resources, cutting down on the number of fake tracks (those that didn't come from a real particle) is important. This research seeks to do this by utilizing a quantity called bend, which gives a rough estimate of the direction of the particle as it passes through a sensor. Bend is used to implement a bend consistency cut, which requires that the bend of each signal on a possible track is consistent with the track's transverse momentum. First this cut was implemented, and then its performance was studied. Results suggest that this cut will greatly reduce the loss of tracks due to lack of resources, while throwing away only a trivial number of real tracks.

Background

This project was concerned with a portion of the tracker known as the tracker. The tracker works by measuring the positions of particles as they pass through these layers, which are made of thousands of individual detectors known as strips. When a particle passes through a strip it creates a stub, an electrical signal that represents a single interaction of a particle with the tracker. A particle will produce stubs in multiple layers of the detector, which form the track of the particle. The trajectory of a charged particle will bend in the 3.8T magnetic field[1] with a radius of curvature that is proportional to the particle's transverse momentum. Determining this transverse momentum and using it in the L1 Trigger is the goal of the track reconstruction algorithm.

The finer details of the detector geometry are illustrated in figure 1. The strips in each layer are arranged into modules, which consist of two rows of strips stacked on top of each

other, separated by values in the range of 1.8-4.0mm. This means that each stub actually consists of two signals, one in the inner row of strips and the other in the outer row. The horizontal difference between these two signals (measured in units of strips) is a quantity known as bend. Bend supplies a rough estimate of the trajectory of a particle, as shown by the red arrow in figure 1.

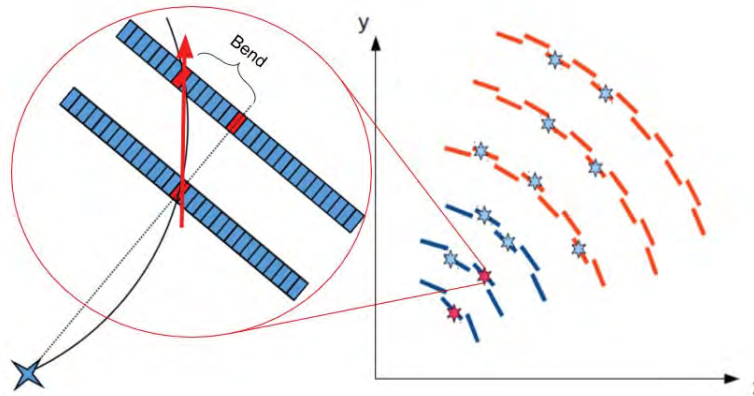


Figure 1: On right is a cross section of the barrel of the detector populated with stubs. Zooming in on a stub shows the two signals, and the horizontal difference in their positions known as bend. Bend estimates the direction of particle as it passes through detector plane.[2]

The first stage in reconstructing a track is forming a group of two stubs called a tracklet. Currently every plausible combination of stubs must be checked to ensure that no particles are ignored, but with enough occupancy in the tracker, this is impossible to do with the resources available. Requiring that each stub's bend is consistent with tracklet transverse momentum allows the algorithm to skip over stub pairs that couldn't have come from a single particle, and save resources for those that did. This is the bend consistency cut which was implemented and tested.

This cut requires a method of converting a stub pair's coordinates into expected bend, which can then be compared to measured bend. Instead of working with transverse momentum, the formulas work with inverse radius of curvature r_{inv} , which is inversely proportional to transverse momentum. The working formulas for the conversion from stub pair coordinates to expected bend is

$$r_{inv} = \frac{2.0 \sin(\phi_2 - \phi_1)}{(r_2 - r_1) \sqrt{1.0 + \frac{2r_1r_2(1 - \cos(\phi_2 - \phi_1))}{(r_2 - r_1)^2}}} \quad (1)$$

$$bend = \frac{-0.5 * 0.18 * r * r_{inv}}{pitch} \quad (2)$$

where r and ϕ are the coordinates of the stubs in polar coordinates, and $pitch$ is the width of the detector strips. In the endcaps, formula 2 becomes

$$bend = \frac{-0.5 * spacing * r^2 * r_{inv}}{pitch * z} \quad (3)$$

where $spacing$ is the separation between the two rows of strips in the detector plane, and z is the z -coordinate of the stub.

Methods

This work was done by studying a simulation of the detector written in software. However, because the algorithm will eventually be implemented in firmware, every operation performed in the software had to be able to be implemented in the firmware. This imposes limitations on the precision and types of calculations that could be done. For example, the firmware can't perform the calculations necessary to do many mathematical operations. Instead look-up tables must be built, where the firmware simply takes a set of inputs which map to a value in a table to find the output. This means that instead of calculating expected bend for each stub pair, a look-up table had to be built[3]. In the barrel, this table takes the inner phi, outer phi, and measured bend as inputs. In the endcaps, the table takes the same parameters plus the outer stub radius. Building the lookup table also required specifying the tolerance of the bend cut, or the maximum number of bend units that the measured bend could be away from the expected bend for the stub pair to be accepted (see results section).

Another limitation of the FPGA firmware is the number of bits that can be used to store bend values. At their maximum, possible bends cover a half-integer range between

-7.5 and 7.5, which makes for 31 possible bend values. This would require 5 bits to keep full resolution, but only 3 bits are available in layers 1-3 and the endcaps, and only 4 bits are available in layers 4-6. As a result, measured bends had to be encoded in some cases, depending on the bend window and where the stub originated[4]. The encoding changed for various situations, but it always involved merging 2 or more bend values into a single intermediate value. An example of this encoding is shown in figure 2.

-2.0	-1.5	-1.0	-0.5	0.0	0.5	1.0	1.5	2.0
↓↓↓↓↓Encoding↓↓↓↓↓								
-1.75	-1.0	-0.5	0.0	0.5	1.0	1.75		

Figure 2: Encoding scheme used for PS modules with bend window of 4. Turns 9 bend values into 7, which can be represented in 3 bits.

Incorporating encoded bend into the bend consistency cut involves taking the quarter integer bends and rounding down to the closest half integer bend. This rounded bend can then be passed to the lookup tables.

The performance of the bend cut is measured in two ways. The first is decrease in occupancy, which is the number of stub pairs that are passed through the algorithm. This is measured by a stub pair counter placed after the bend cut. The cut should drop as many fake stub pairs as possible while dropping few real stub pairs. This leads to the second measure of performance, which is efficiency, or the fraction of real particles that are properly identified and matched to a trajectory. If the cut drops real stub pairs, this will result in a drop in efficiency.

Results

The most fundamental test of the cut's accuracy is how well the formulas that find expected bend match actual bend. To do this, expected bend was found using the true transverse momentum of the particle. Then the difference between expected and measured

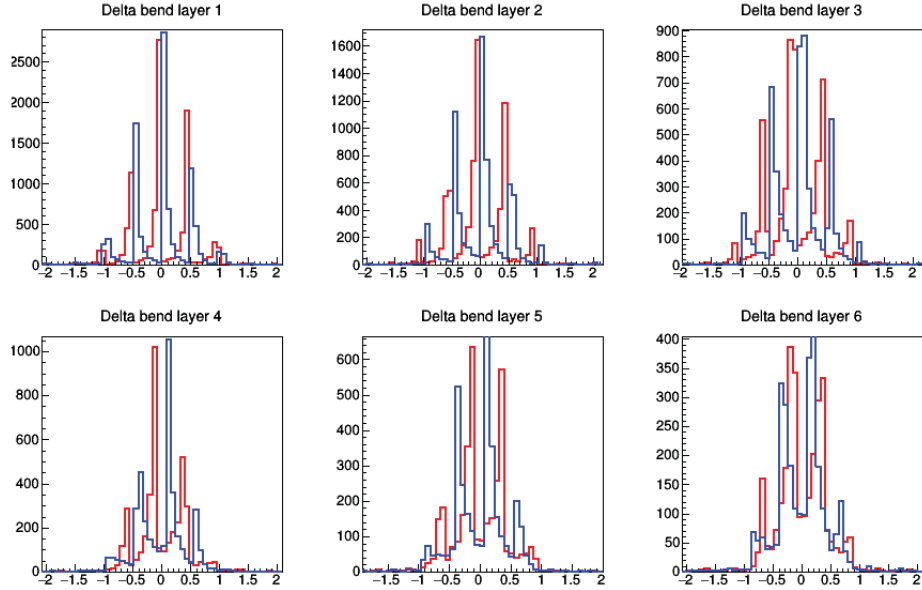


Figure 3: Measured minus expected bend in each layer of tracker. Red line is positive charged particles, blue line is negative.

bend was placed in histograms divided by barrel layer as shown in figure 3.

A slight charge separation is noticeable in the higher layers, which is likely a result of the Lorentz drift caused by the electric fields in the detector, but it could also be that the bend calculation is off by a multiplicative factor. Additionally these distributions spike at half integer differences. This is because the target bend value have half-integer precision, so the measured bend will be off the calculation by half-integer amounts. The same plots are shown for the endcaps in figure 4.

In the endcaps the distributions are more or less uniform, but they are more widely spread than the barrel layers. The RMS and Standard deviation of a Gaussian Fit for each of the distributions are shown in table 1.

These numbers suggest that the bend calculation is less accurate in the endcaps and higher barrel layers, which means that the cut has more limited performance in those areas. However, as a whole these plots show that the bend calculation is able to accurately predict bend to within 1 bend unit of accuracy.

Next, the effects of various bend consistency cuts on occupancy and efficiency were stud-

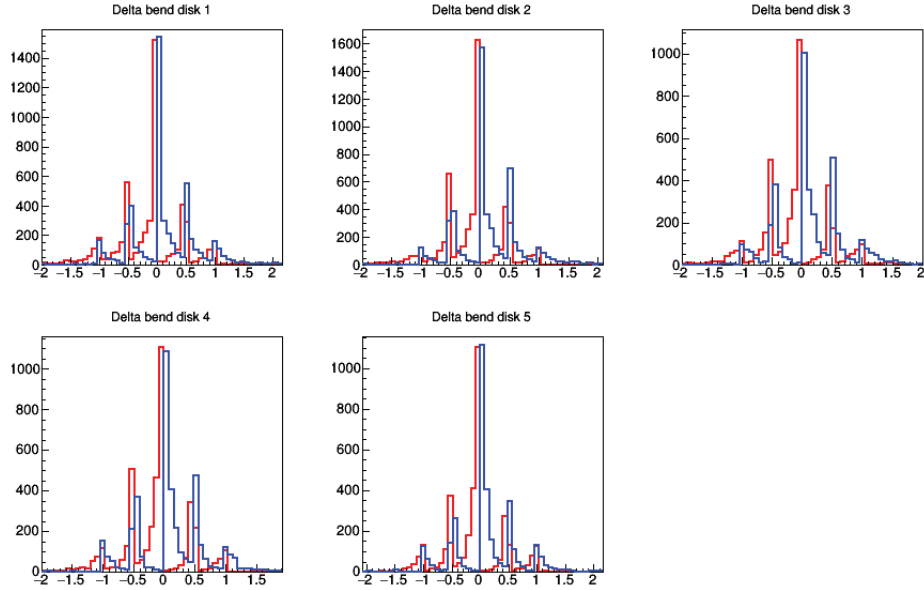


Figure 4: Measured minus expected bend in each endcap of the tracker. Red line is positive charged particles, blue line is negative.

ied. Cuts with a tolerance of 1.0, 1.2, 1.5, 2.0, and 100 (no stub pairs are cut) were tested. The occupancy plot shown in figure 5 is a histogram of the input counter in the tracklet calculator, which occurs just after the bend cut in the algorithm.

As the bend cut tolerance decreases, more stub pairs are thrown out and the occupancy in the tracklet calculator goes down. This is a clear sign that the bend cut is working properly. The most important quantitative measure of occupancy is the percentage of counters above the truncation limit. This limit is a result of the limited processing power of the FPGA units, which aren't able to handle more than 36 stub pairs in one tracklet engine. Percentages for each cut and in each section of the detector are shown in table 2.

Layer	RMS	Std. Deviation
1	0.510	0.486
2	0.524	0.439
3	0.560	0.413
4	0.622	0.401
5	0.650	0.412
6	0.918	0.382

Endcap	RMS	Std. Deviation
1	0.815	0.621
2	0.748	0.590
3	0.757	0.617
4	0.751	0.561
5	0.690	0.562

Table 1: RMS and Std. Deviation of distributions for all layers and endcaps

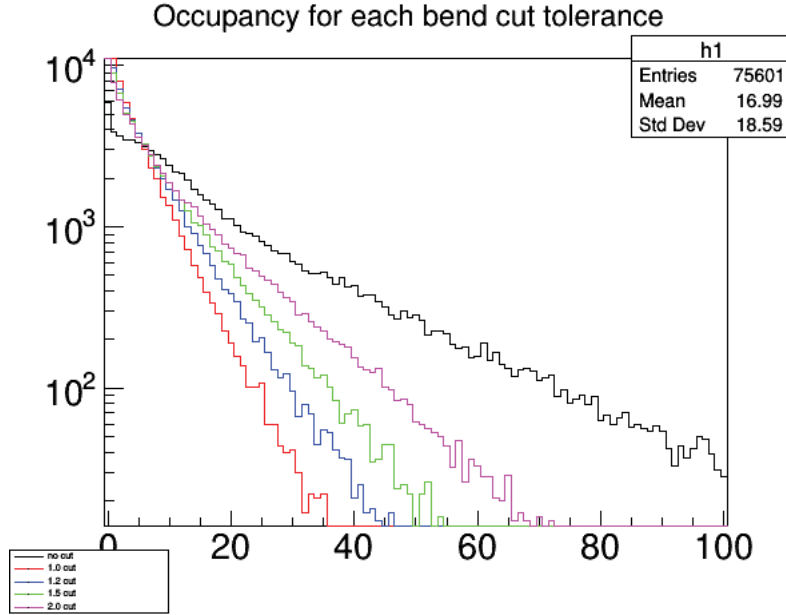


Figure 5: Occupancy for various bend cuts, with no cut being tolerance 100 (no stub pairs should be cut). Tighter cuts clearly reduce the occupancy in the tracklet calculator input.

These numbers show that the cut significantly reduces the effects of truncation. However, cutting much harder than 1.5 tolerance leads to diminishing returns. Ideally no tracklet engines would contain more than 36 stubs, but cutting very tightly will tend to reduce efficiency as real stub pairs begin to be thrown out. The effects of various bend cuts on efficiency are shown in figure 6, where each cut is compared to the benchmark no cut (100 tolerance) shown in black.

These plots show efficiency across the full range of eta, so they include both the endcap and barrel portions of the detector. Separating out the results between central eta ($|\eta| \leq 1.6$) and high eta provides a good estimate for efficiency in the barrel and endcap respectively. Averaging all of the data points in each of these ranges provides average efficiency for the barrel and endcap. These numbers can be seen in table 3.

The efficiency of the algorithm is uniformly higher in the endcap, but the bend cut appears to work much better in the barrel. In the barrel implementing the cut actually increases efficiency, even for the very tight 1.0 cut. This is because removing fake stub pairs allows the algorithm to catch more real ones that aren't being ignored due to truncation.

Section	Tolerance	% Over 36 Pairs
Barrel	No cut	18.6%
	2.0	4.1%
	1.5	1.3%
	1.2	0.5%
	1.0	0.2%
Endcap	No cut	6.3%
	2.0	2.2%
	1.5	0.9%
	1.2	0.5%
	1.0	0.1%

Section	Tolerance	% Over 36 Pairs
Overlap	No cut	16.3%
	2.0	4.9%
	1.5	1.9%
	1.2	1.0%
	1.0	0.2%
Total	No cut	14.2%
	2.0	3.4%
	1.5	1.2%
	1.2	0.5%
	1.0	0.1%

Table 2: Percentage of tracklet engines with more than 36 stub pairs, shown for each section and bend cut tolerance.

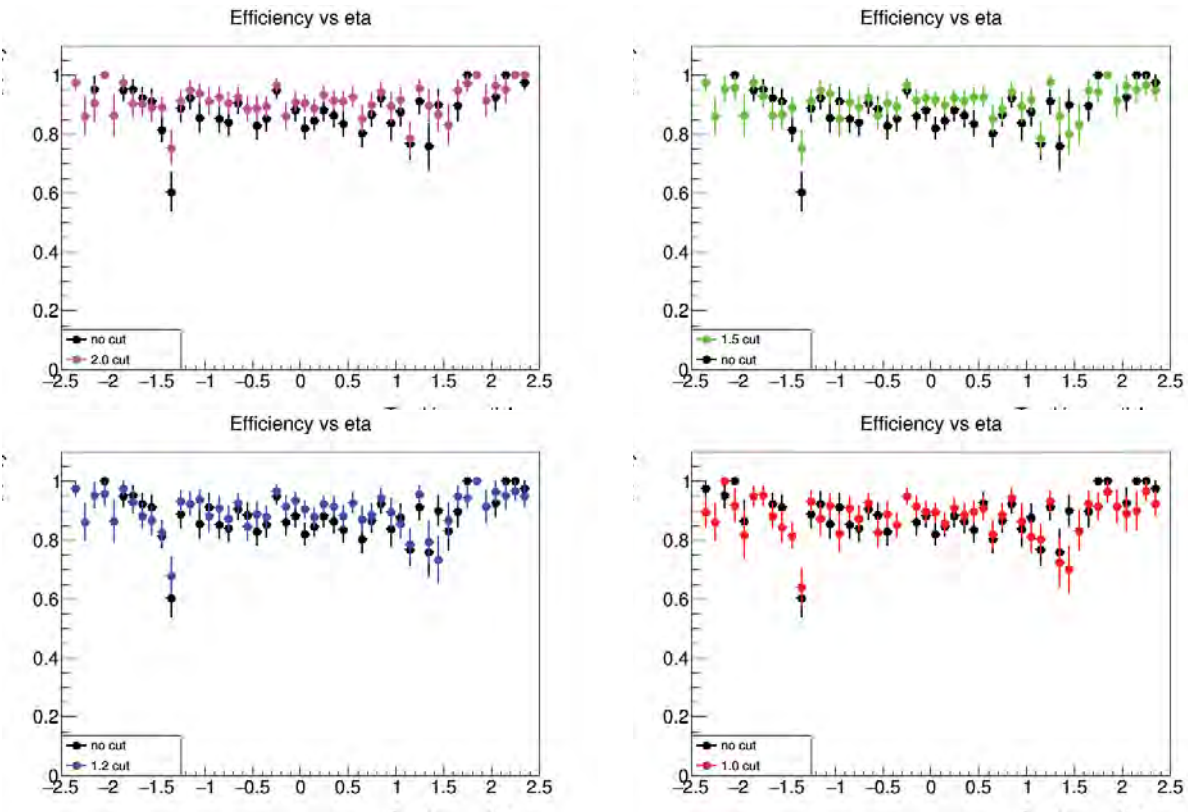


Figure 6: Plots of efficiency vs eta for each bend cut compared to no cut (100 tolerance). Eta is a coordinate that related to polar angle, so higher eta is closer to parallel to the beamline.

The peak efficiency occurs for the 2.0 and 1.5 tolerance cuts, but the 1.5 reduces truncation significantly more, so this is the cut that was implemented. This value is approximately 3σ of the bend resolution plots, which is where the best tolerance was expected to be.

Barrel		Endcaps	
Tolerance	Efficiency	Tolerance	Efficiency
No cut	85.4%	No cut	94.8%
2.0	89.8%	2.0	94.6%
1.5	89.7%	1.5	93.6%
1.2	88.4%	1.2	93.8%
1.0	86.6%	1.0	91.6%

Table 3: Efficiency in the barrel and endcap sections of the detector for each bend cut.

In the endcaps, the efficiency begins to drop as soon as the cut is implemented. This makes sense because truncation effects the endcaps less, so there isn't as much room to be gained by removing fake stub pairs. The efficiency numbers suggest that the best cut in the endcaps is the 2.0 tolerance, which has minimal efficiency loss but still cuts a large number of stub pairs. Again, this is approximately 3σ of the bend resolution plots for the endcap.

Further Studies

One remaining task in this study is to improve the resolution of the bend calculation. Other groups working on this project have managed to produce better resolutions than these results, so there is room for improvement in this calculation.

Once this is done, the bend consistency cut must also be implemented in the projection stage of the algorithm. This is the stage where additional stubs are matched to the already formed tracks. Cutting in this stage as well should increase the performance of the algorithm as a whole.

References

- [1] CMS collaboration: Detector, <http://cms.cern/detector>
- [2] Figure created by Patrick Shields
- [3] Original code for lookup tables and consistency cut written by Anders Ryd
- [4] Code for bend encoding scheme written by Ian Tomalin and Sebastian Viret

SUPERNOVA PROGENITORS OF LIGHT ELEMENTS ABUNDANCES IN R- PROCESS-ENHANCED STARS

ADVISOR: PROF. TIMOTHY C. BEERS
ERIKA HOLMBECK
AUTHOR: PHUONG THI HOANG

PHYSICS REU
NOTRE DAME 2018

Abstract

In this report we try to predict the stellar initial mass function by using the light element abundances of 70 stars including r-I, r-II, limited -r and CEMP (carbon-enhanced metal poor) stars in a previously studied stellar sample. The method we use is similar to the idea presented in Placco et al. 2016 [1] to measure the CN abundance in MOOG and record the predicted masses from StarFit. Our plot of these masses with metallicity [Fe/H] suggests that the first stars were mostly grouped around 20-30 Solar masses (M_{\odot}). On the other hand, we compare the result from StarFit with an r-II star in Reticulum II [4] and find some similarities. We also come up with the noted-star list for further investigation on CN band in the spectra.

Introduction

First described in 1957 by Burbidge, Burbidge, Fowler, and Hoyle [5], the r-process (rapid-neutron-capture process) is responsible for synthesizing roughly half of the elements heavier than iron present in the Solar System. Over decades from the realization that not all stars in the Galaxy have the same elemental composition, metal-poor stars have been important in understanding the nature of the first stars in the Universe, discussed in Beers & Christlieb (2005) [3]. By measuring the elements in old stars existing today, we could try to know how the first elements were made in the first stars. With the discovery of CEMP stars [3], it suggests that a significant amount of carbon was produced in some early time of the Universe with possible sources needing to be verified. With these demands, many sky surveys have been implemented, targeting bright candidates of neutron-capture (r-process) enhancement as well as carbon enhancement (CEMP) stars. These surveys use different techniques; for example “snapshot”

high-resolution spectroscopy as in Christlieb et al.(2004) [6] and Hansen et al. (2018) [7] are often short, normally leading to investigating hundreds of stars' spectra. Working on these huge received data requires human efforts and computation advances.

The mass distribution of stars formed throughout the history the Universe plays an important role in drawing an evolutionary picture of galaxies. Nowadays, modern computation allows astrophysicists to build sophisticated models for the production of light and heavy elements from supernovae explosions by obtaining the abundances of elements in chemically enriched stars, which have been polluted from the previous generations of stars. StarFit is one of these models that predicts elemental abundances from supernovae. In this report, we use this supernova model to predict the progenitor mass of stars in the “DuPont pilot” sample which have already been identified as r-II, r-I, limited-r, or CEMP. These identifications were made by measuring heavy elements that are made in the r-process (Sr, Ba, Eu, and Fe). However, the supernovae model predicts light elements only. Therefore, we only focus on their light element (N, Na, Mg, Al, Si,... Ni) abundances from the line absorption strength. The nitrogen abundance is determined from spectral synthesis of the CN band [1] instead of measuring absorption lines. Furthermore, the carbon abundance has to be corrected from the observed data with the procedure described in Placco et al. (2014) [2]. By making the plot of supernova progenitor mass with metallicity, we see the large population of stars in the mass range of 21.5 and 27-28 M_{\odot} (Solar masses). It raises the question as to why the stars prefer this mass even though no heavy elements (r-process) are included in this analysis.

In addition, we also try StarFit with another r-II star in Recticulum II [4], an ultra-faint dwarf galaxy enriched by an r-process event, using light elements only. The result is quite similar

compared to results for an r-II star in the pilot sample: the mass 21.5 appears again. It is hard to say from just one star but it is worth investigating the initial mass function between the two galaxies in the future.

1. Du Pont pilot sample

To identify r-II stars important for understanding the r-process, an extensive search for bright ($V < 13.5$), very metal-poor ($[Fe/H] < -2$) and extremely metal-poor ($[Fe/H] < -3$) stars in the Milky Way halo was implemented by Hansen et al. (2018) [7]. The sample used in this report is the first dataset on this survey in the Southern hemisphere obtained during six nights in August 2016, with the Echelle spectrograph on the du Pont 2.5m telescope at the Las Campanas Observatory. In this period of time 107 total stars were observed, finding 12 stars strongly enhanced in heavy r-process elements (r-II), 42 exhibiting moderate abundances of heavy r-process elements (r-I), 20 stars showing low enhancement of heavy r-process, but higher abundances of light r-process elements (limited-r) and 7 CEMP stars which have large carbon abundances. In comparison with a previous survey (Barklem et al. 2005) [8]---which expected a rate of finding r-II and r-I of $\sim 3\%$ and $\sim 15\%$, respectively---this sample represents a more successful performance.

Hansen et al. 2018 [7], measured heavy-element abundances and stellar parameters. These parameters include effective temperature (T_{eff}), surface gravity ($\log g$), microturbulent velocity (ξ), which are essential for this work.

2. Method

The process of getting the supernova progenitor mass of a star involves three computational steps. First, light-element equivalent widths (EW) in snapshot high resolution spectra are

measured by using the software IRAF. Next the abundances of light elements are obtained in MOOG from these EWs. Finally, these abundances are the input for StarFit to get the progenitor mass, using the procedure described in Placco et al. (2014) [4]

a. IRAF

IRAF is a widely used software in astronomy with various functions. In this report, we use this software to measure the EWs of light elements from the absorption lines of the spectra. The wavelengths of the absorption lines correlated to 10 light elements (Na, Mg, Al, Si, Ca, Sc, Ti, Cr, Mn and Co) are indicated in Placco et al. (2016) [1]. At the end of this step, a list of wavelengths and corresponding EWs must be obtained for each of these elements.

b. MOOG

MOOG is another software that calculates the abundances of the elements in stars from an input list of their EWs, given the stellar atmospheric parameters which were already calculated in Hansen et al. 2018 [5]. Nitrogen is an important light element ejected by supernovae. Different from other light elements, it is not possible to obtain the nitrogen abundance from the EW measured directly from an absorption line since the transitions we observe in stars are from CN molecules and not just from nitrogen atom [1]. Therefore, we derive the abundance by comparing the observed spectrum to model spectra using MOOG. We provide the atmospheric model, the line list, and the observed spectrum to MOOG. Using the simulated spectrum from MOOG, we adjust the abundances until they best match the observed spectrum. Then the abundance that matches the best is the derived abundance of that element in the star. An example using nitrogen is shown in Figure 1.

As in the Figure 1, nitrogen abundance could not be measured in all stars because of the large noise. The large noise causes difficulty in adjusting the continuum as well as an abundance match. Other stars have small nitrogen abundance, which is reasonable since the stars we are measuring are r-process enhanced stars with small CN band. However, it leads to the lack of nitrogen abundance in some stars which significantly affects the progenitor mass as described in Step 3. A list of elements and corresponding abundance (including carbon, nitrogen, and iron abundance) should be obtained after finishing this step.

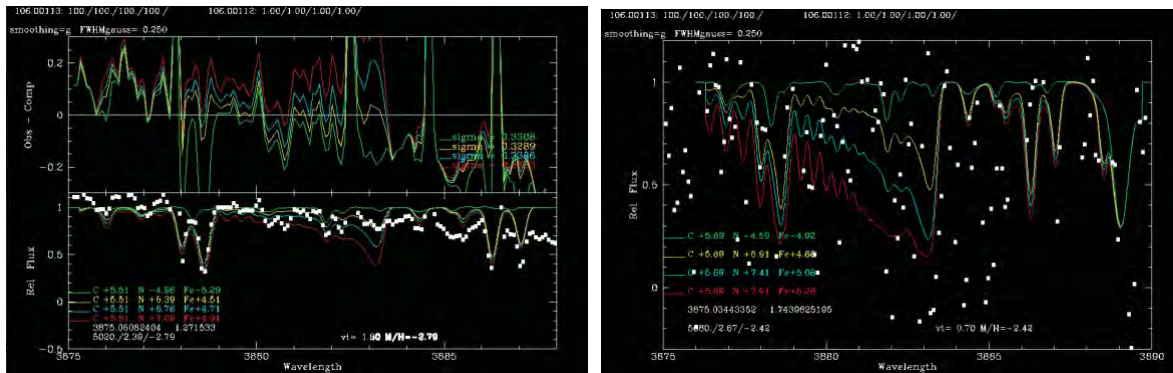


Figure 1: Simulated spectra of two different stars and four values of synthesized abundances (colored lines). C, N, and Fe are adjusted in this example, and their synthesized abundances are indicated in the left corner. The carbon abundance is fixed so its four numbers are the same, and we change vary the nitrogen abundance. Left: the blue line is the best fit with the observed line, compared with two other lines, the Nitrogen abundance is 6.76. Right: an example of a low signal-to-noise spectrum where nitrogen could not be measured.

c. StarFit

StarFit is a program that makes the elements ejected from a supernova to an input list of elemental abundances. In this project, we use an online version of StarFit on the website starfit.org. The follow-up abundance list from the previous step is given as the input file to StarFit. The output are the models with the certain stellar mass and supernova explosion energy based

on the elements we observe in the star. The progenitor mass of the best fit data is the one we collect (see Figure 2).

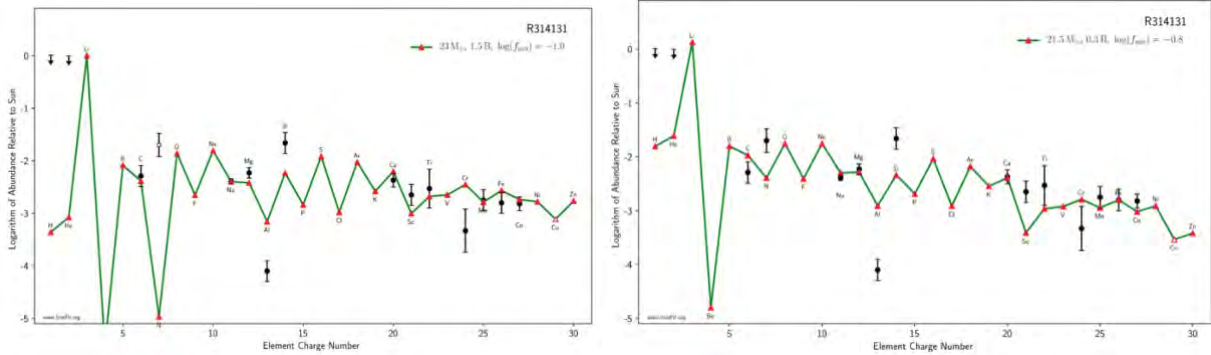


Figure 2: The best fit model of StarFit to a star using N abundance (left) and no N abundance (right) in the input list. When nitrogen is included, the progenitor mass of the star is $21.5 M_{\odot}$. The progenitor mass of the same star without including nitrogen in the StarFit input is $23 M_{\odot}$.

As in the figure 2, the difference between two StarFit model of the same star is considerable. It is clear that the model in Figure 2 with N is a better match to the abundances. Otherwise, with the stars where we could not measure Nitrogen abundance, the other result is acceptable. Fortunately, in 70 stars measured, only 6-7 stars have no nitrogen abundance.

3. Results and Conclusion

a. Progenitor mass distributions

In this projects, light elements abundances for a total of 70 stars including 11 r-II, 33 r-I, 19 limited-r and 7 CEMP stars in the du Pont pilot sample are measured. By compiling the progenitor masses of these stars, we plot the masses as a function of $[Fe/H]$ abundances in Figure 3. However, there is no correlation, which is similar with the $[C/Fe]$ abundances. Moreover, we

notice the large preference of progenitor masses between 21.5 and 27-28 M. no matter what type of star it is (Figure 3).

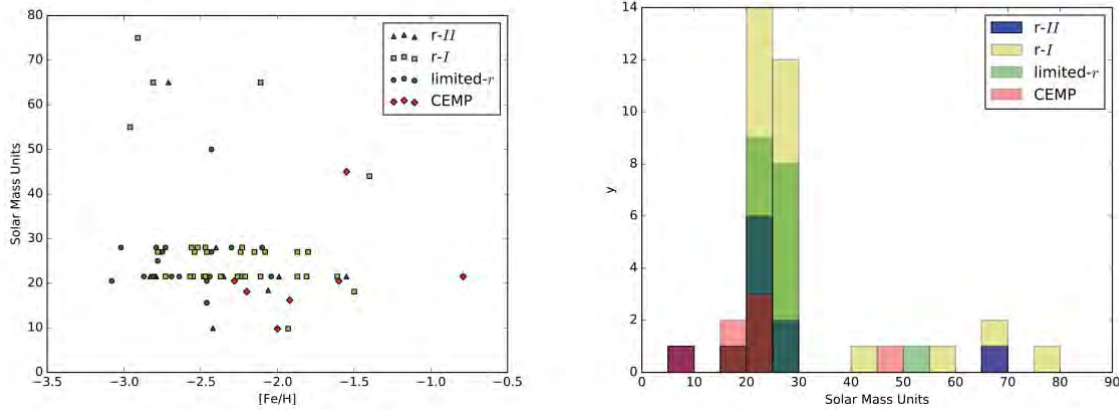


Figure 3: Left: the plot of mass as the function of $[Fe/H]$, no correlation exists. Right: The distribution of 70 progenitor mass where it is grouped mostly around 20-30 M. with all four kinds of stars.

The distribution led to the assumption that all stars might have the same progenitor. Since this is unlikely, there is a question as to why we do not see a correlation with metallicity or type. Our project only considers light elements, which may be similar, so all stars may have the same light element abundances. As a result, the mass of the progenitor stars are grouped around 20-30 M. These assumptions should be verified more with more stars to be measured and not just only in the du Pont pilot sample. However, we could say that light elements that we measured were likely not created by the same mechanism that made the elements Sr, Ba, and Eu since there is no correlation with the heavy elements. Therefore, the mechanism responsible for r-process produces heavy elements, but it is not true for light elements.

b. Compare with a star in Reticulum II

Recticulum II is an ultra-faint dwarf galaxy enriched by rare and prolific r -process event [4]. Ji & Frebel 2018 measured 41 elements abundances and their uncertainties in DES J0335523-540407, a star in that galaxy. We use the data of these abundances (light elements only) as the input for the StarFit to get the progenitor mass. It is surprising that the number $21.5 M_{\odot}$ appears again. Although it is hard to say with just one star, the initial mass function of the galaxy, Recticulum II, might be similar with our Milky Way. This is worth investigating further, especially for this small galaxy.

Reference

- [1] Vinicius M. Placco , Anna Frebel , Timothy C. Beers , Jinmi Yoon , Anirudh Chiti , Alexander Heger , Conrad Chan , Andrew R. Casey , and Norbert Christlieb. (2016). *The Astrophysical Journal*, 833:21.
- [2] Vinicius M. Placco, Anna Frebel, Timothy C. Beers, and Richard J. Stancliffe. (2014). *The Astrophysical Journal*, 797:21.
- [3] Timothy C. Beers and Norbert Christlieb. (2005).. *Annu. Rev. Astron. Astrophys.*, 43:531–80.
- [4] Alexander P.Ji and Anna Frebel. (2018).. *The Astrophysical Journal*, 856, 2.
- [5] E. Margaret Burbidge, G. R. Burbidge, William A. Fowler, and F. Hoyle. (1957). *Rev. Mod. Phys.*, 29, 547 .
- [6] N. Christlieb , B. Gustafsson , A. J. Korn , P. S. Barklem , T. C. Beers , M. S. Bessell , T. Karlsson and M. Mizuno-Wiedner. (2004). *The Astrophysical Journal*, 603:708-728,.
- [7] Terese T. Hansen,1 Erika M. Holmbeck, Timothy C. Beers, Vinicius M. Placco, Ian U. Roederer, Anna Frebel, Charli M. Sakari,Joshua D. Simon,and Ian B. Thompson. (2018).

[8] Barklem, P. S.; Christlieb, N.; Beers, T. C.; Hill, V.; Bessell, M. S.; Holmberg, J.; Marsteller, B.; Rossi, S.; Zickgraf, F.-J.; Reimers, D. (2005). *Astronomy and Astrophysics*, Volume 439, Issue 1.

Dependence of Helium Atmospheric Pressure Plasma Jet (APPJ)-Induced DNA Damage on Voltage Pulse Frequency and Irradiation Time

Kemo BS Jammeh

Advisor: Sylwia Ptasinska

University of Notre Dame Radiation Laboratory, Notre Dame, IN, 46556

July 28, 2018

ABSTRACT

The dependence of Atmospheric Pressure-Plasma Jet (APPJ)-induced DNA damage on the frequency of voltage pulse was investigated. The APPJ source consists of two cylindrical brass electrodes and a dielectric silica capillary connected to a power supply and a pulse generator. The plasma generated from the source is used to irradiate DNA samples at different frequencies and the damage (single-stranded breaks, double-stranded breaks, and denatured DNA) resulting from the irradiation is quantified using agarose gel electrophoresis and imaging techniques. It was found that total DNA damage increased with increasing frequency. Time of irradiation studies was also performed, and the results showed that total DNA damage was higher for longer times of irradiation at a constant frequency. Furthermore, it was found that, while this time dependence trend holds for other frequencies, the extent of damage varied significantly for the same set of irradiation times.

INTRODUCTION

In the past two decades, a breakthrough in plasma physics was made when cold non-equilibrium plasma was generated at atmospheric pressure [1]. This type of plasma, mostly called

Atmospheric Pressure Plasma Jets (APPJs) or cold plasma, is a discharge formed in dielectric capillary tubes when a gas is subjected to direct or alternating voltages with amplitudes in a few kV range, at frequencies in the kHz range [2,3]. APPJs, while maintaining relatively low temperatures, contain strong electromagnetic fields as well as several reactive species including reactive oxygen species (ROS) like ozone (O₃), and reactive nitrogen species like nitrogen dioxide (NO₂)[1,2,4,5]. These reactive species are known for their strong oxidative properties and are capable of initiating signaling cascades in biological molecules, leading to cell death and other biological processes [6,7]. The fact that their generation does not involve expensive vacuum systems [8] and the unique reactive environment they create makes APPJs applicable in several fields including radiation chemistry and clinical medicine [9,10].

The application of plasma on the human body for therapeutic purposes (plasma medicine) has a long history [11]. It has been used in the treatment of wounds [12], the inactivation of bacteria [1], blood coagulation and several other surgical applications [11]. These early applications of plasma in medicine relied on the thermal bio-degradable nature of plasma, making selective treatment of heat sensitive surfaces difficult[4,6,12]. With the emergence of atmospheric pressure plasma jets, selective treatment of heat sensitive surfaces has been made possible. APPJs have been found to induce apoptosis in cancerous cells while causing little damage to nearby healthy cells [5,13,14] making them plausible agents in cancer therapy. Furthermore, it has been shown that DNA molecules experience strand breaks upon exposure to APPJs [15,16]. While the aforementioned effects of APPJs on human cells offer promising possibilities in their use in cancer therapy, usage is still a long way out. Little is understood about the mechanism of plasma-induced DNA damage and cell death. For now, the widely accepted view is that the reactive species in plasma are responsible for effects discussed above[7]. Notwithstanding,

elucidating the exact process of the damage process remains an interesting challenge. Understanding the optimal conditions at which APPJs must be generated to perform certain desired and controlled DNA damage is an important step towards overcoming this challenge. The environmental conditions of APPJs depend on the parameters of the plasma source. It has been reported that the number of reactive species, especially ROS and RNS change with changes in plasma source parameters like flow rate [15]. Ptasinska et al. made interesting observations about the dependence of DNA damage pattern on irradiation time, the distance between the nozzle of the plasma source and the DNA sample, applied voltage, as well as the DNA concentration [17]. This study is a continuation of their work on the correlation between plasma variables and DNA damage. The dependence of DNA damage on the frequency of the pulse generator was studied for a constant time of irradiation. Furthermore, we investigated the dependence of DNA damage on the time of irradiation for different frequencies to see if changes in frequency influences time dependence.

EXPERIMENTAL SETUP AND METHOD

Figure 1. shows a schematic representation of the APPJ source used in this study. It consists of two brass electrodes wrapped around a fused silica capillary tube. The bottom electrode is the powered electrode and it is connected to a transformer which is directly connected to a power supply. The upper electrode is grounded to maintain an electric potential difference between the two electrodes. To ignite plasma, Helium gas is introduced into the system via the fused capillary tube and the flow rate is set to 2.00 standard liters per minute (slm) using a system of flow controllers. The powered electrode is then supplied with 10 kV in square pulses of width 500 μ s at a desired frequency ranging from 0.25 kHz to 5.00 kHz. The plasma that is formed exits the

silica capillary via an orifice located below the powered electrode and is applied to a DNA sample a few millimeters downstream.

DNA sample is put in a glass well and irradiated for the desired time and then removed from plasma exposure. The irradiated sample is collected using an automatic pipette. The glass well is then washed with $5\mu\text{l}$ of Phosphate Buffered Saline (PBS) to collect any remaining DNA samples in the well.

Undamaged plasmid DNA is usually supercoiled in nature. Upon the introduction of a single-stranded break (SSB), it acquires an open circular form. When a double-stranded break (DSB) is introduced, the DNA molecule becomes linear [16]. To quantify the different types of damage induced on an irradiated DNA sample, agarose gel electrophoresis was used to separate the different forms of DNA molecules.

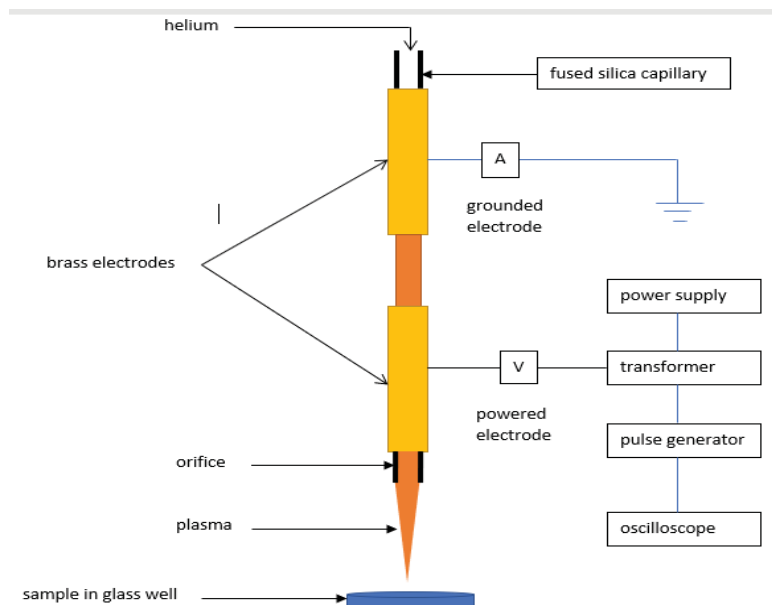


Figure 1. Schematic View of the Atmospheric Pressure Plasma Jet Source

RESULTS AND DISCUSSIONS

3.1 Dependence of DNA Damage on Increasing Frequency.

DNA samples were irradiated at different frequencies; from 0.25 kHz to 5.00 kHz (figure 3). The voltage (10 kV), flow rate (2.00 slm), pulse width ($500\mu\text{s}$), and irradiation time (15s) were kept constant. Three samples were irradiated for each frequency and the mean of the three trials is used to represent the quantity of damage. The error bars represent the standard error between the three trials. The fraction of each type of DNA molecule (SSB, DSB and SC) is plotted against the frequency (figure 2).

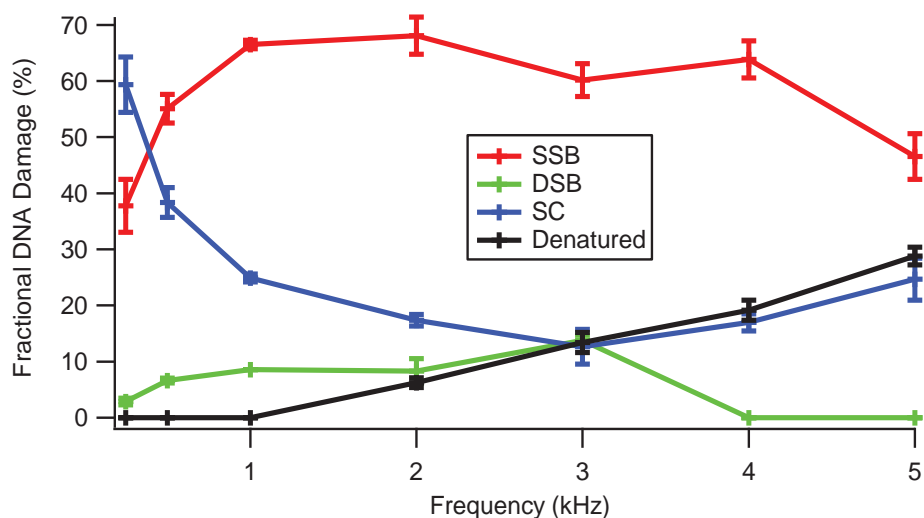


Figure 2. Dependence of the different types of DNA damage on the frequency of the voltage pulse when irradiated for 15 seconds.

As seen in Figure 3, about 60 % of the DNA samples experienced SSB when irradiated at 0.25 kHz for 15 seconds. Under these conditions, the quantity of DSBs was not significant. SSB percentage continues to increase reaching about 65% at 2.00 kHz. Between 2.00 kHz and 3.00

kHz, SSB percentage decreased to about 60%. Notice, however, that this unexpected decrease in SSB between 2.00 kHz and 3.00 kHz is accompanied by a corresponding increase in DSB percentage between those frequencies. As a result, the total DNA damage is constant in that frequency range. This same reasoning can be used to explain the decrease in DSB percentage between 3.00 kHz and 4.00 kHz. The decrease is balanced by the increase in SSB making total DNA damage relatively constant over that range. However, the slope of DSB decrease is steeper than the slope of the SSB increase. This suggests that other factors may be contributing to that extra decrease in DSB. This suggestion is further strengthened by the fact that the balancing act between SSB and DSB does not explain the decrease in SSB between 4.00 kHz and 5.00 kHz. In that frequency range, DSB remains constant at about 0%.

To explain the unexpected behavior of the SSB curve between 4.00 kHz and 5.00 kHz, one needs to consider the black curve in figure 2. At 2.00 kHz and higher, an extra band of DNA appeared beyond the supercoiled band in gel electrophoresis images. As of now, the belief is that this band represents denatured DNA. This belief is supported by studies conducted by Samara et al [18] in which they measured the temperature of plasma at different frequencies for different voltages (figure 3). As seen in figure 3, the temperature of plasma ignited by a 10-kV power source is about 50 °C at 2.00 kHz. This temperature matches nicely with the denaturation temperature of DNA observed by Yan et al when they measure the denaturation temperature of plasmid DNA using atomic force microscopy [19]. While the temperature of the plasma is likely to be the major contributor to DNA denaturation, the reactive species in the plasma could also play a role, either by directly breaking the hydrogen bonds or by significantly lowering the pH of the DNA solution thereby initiating acid induced DNA denaturation. Further studies will have to be done to further understand the exact causes of the denaturation.

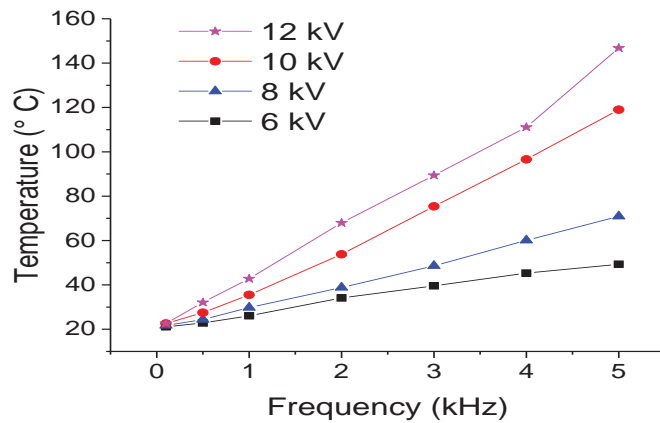


Figure 3: Dependence of plasma temperature on the frequency of the voltage pulse for several voltages [18].

Regardless of the exact nature of DNA denaturation in these circumstances, we believe it is responsible for the decrease in SSB without a corresponding increase in DSB.

3.2: Changes in Frequency Influences Time Dependence of DNA Damage

Adhikari et al. investigated the dependence of DNA damage on irradiation time and found that total DNA damage increased from 9% to 100 % when irradiated between 15s and 60s [17]. In this study, an attempt was made to see whether changes in frequency influences the dependence of DNA damage on irradiation time. For different frequencies, DNA samples were irradiated with plasma generated by a 10-kV voltage with a constant pulse width and flow rate of 500 μ s and 2.00 slm respectively.

At 0.25 kHz, it was found that total DNA damage increased from about 10% to 53% within the first 15 seconds of irradiation (Figure 4a). At 75 seconds, more than 75 % of the DNA sample experienced SSB while about 10% experienced DSB, bringing total DNA damage to about 95%. These numbers are significantly different from what was obtained for irradiation done at 0.50

kHz. In the first 15 seconds, for example, 70% of the DNA sample was damage when irradiated at 0.50 kHz. 100% (90% SSB and 10 % DSB) of the DNA was damaged after 45 seconds (figure 4b).

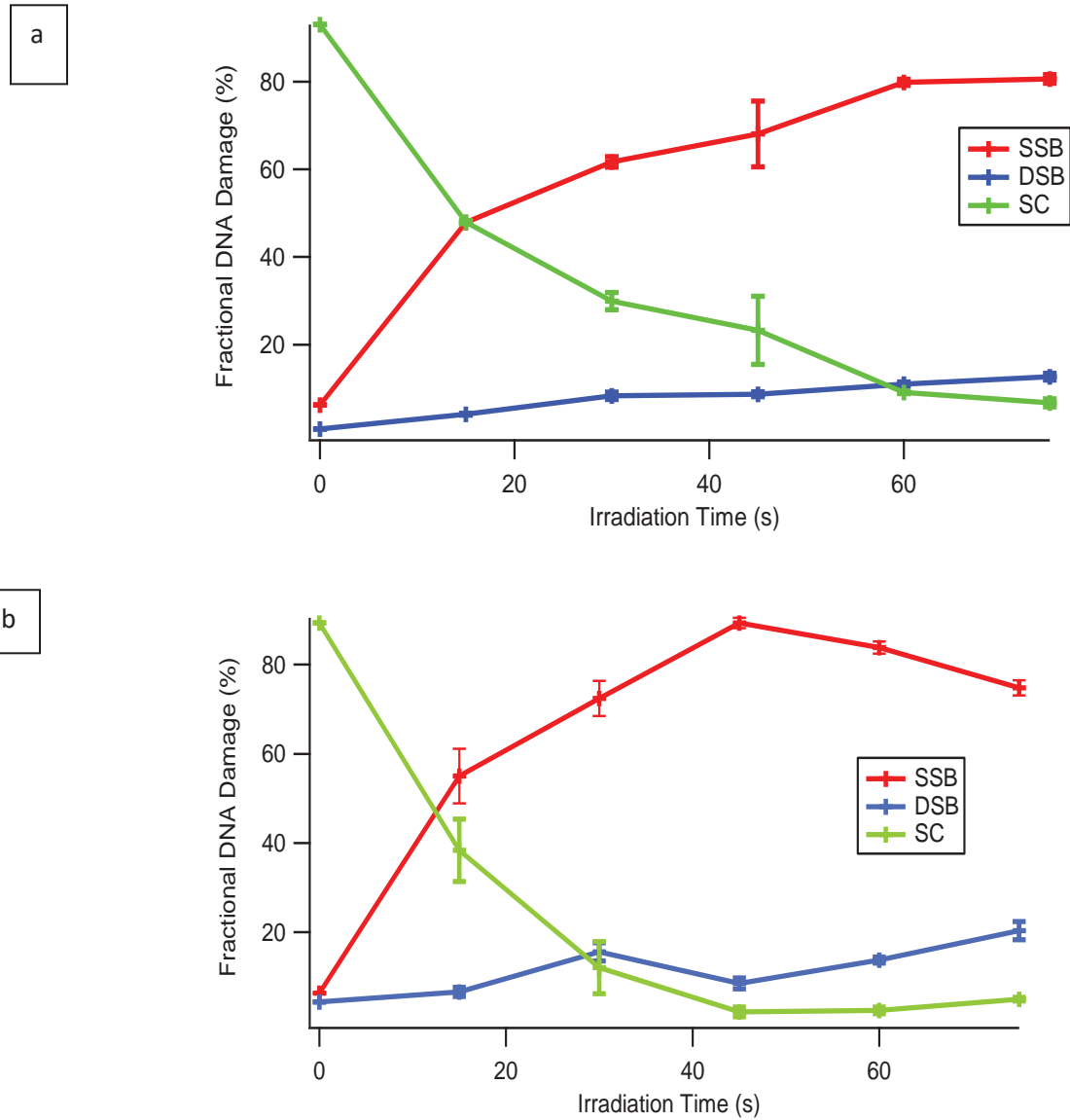


Figure 4. Dependence of DNA damage on irradiation time for a voltage pulse frequency of (a) 0.25 kHz (b) 0.50 kHz.

4. CONCLUSION

The dependence of Atmospheric Pressure Plasma Jet (APPJ)-induced damage on the frequency of the pulse generator was investigated. It was found that total DNA damage increased between 0.25 kHz and 0.50 kHz. Between 2.00 kHz and 4.00 kHz, total DNA damage remains relatively constant as decreases in SSB were balanced by increases in DSB and vice versa. At frequencies above 2.00 kHz, irradiation was found to cause denaturation in DNA. While the exact causes of this denaturation remain unknown, it is suspected that the heat content of the plasma is a major contributor.

As an extension of the frequency dependence studies, the possibility of changes in frequency having an influence over the dependence of DNA damage on time of irradiation was investigated. In both cases, it was found that total DNA damage increased with increasing time of irradiation. This increase in damage, however, is more dramatic for the higher of the two frequencies investigated.

REFERENCES

- [1] X. Lu, G. V. Naidis, M. Laroussi, S. Reuter, D.B. Graves, K. Ostrikov, Reactive species in non-equilibrium atmospheric-pressure plasmas: Generation, transport, and biological effects, *Phys. Rep.* 630 (2016) 1–84. doi:10.1016/j.physrep.2016.03.003.
- [2] K.P. Arjunan, V.K. Sharma, S. Ptasińska, Effects of Atmospheric Pressure Plasmas on Isolated and Cellular DNA — A Review, *Int. J. Mol. Sci.* 16 (2015) 1–3. doi:10.3390/ijms16022971.
- [3] W. Yan, D.J. Economou, Gas flow rate dependence of the discharge characteristics of a helium atmospheric pressure plasma jet interacting with a substrate, *J. Phys. D: Appl. Phys.* 50 (2017) 2–5. doi:10.1088/1361-6463/aa8794.
- [4] K.-D. Weltmann, T. von Woedtke, Plasma medicine—current state of research and medical application, *Plasma Phys. Control. Fusion.* 59 (2017) 2–12. doi:10.1088/0741-3335/59/1/014031.
- [5] X. Han, M. Klas, Y. Liu, M.S. Stack, S. Ptasińska, X. Han, M. Klas, Y. Liu, M.S. Stack, S. Ptasińska, DNA damage in oral cancer cells induced by nitrogen atmospheric pressure plasma jets DNA damage in oral cancer cells induced by nitrogen atmospheric pressure plasma jets, *Appl. Phys. Lett.* 233703 (2013) 1–6. doi:10.1063/1.4809830.
- [6] M. Laroussi, X. Lu, M. Keidar, Perspective: The physics, diagnostics, and applications of atmospheric pressure low-temperature plasma sources used in plasma medicine, *J. Appl. Phys.* 122 (2017) 1–20. doi:10.1063/1.4993710.

- [7] Valko M, Izakovic M, Mazur M, Rhodes CJ, Telser J, Role of Oxygen Radicals in DNA Damage and Cancer Incidence, *Mol. Cell. Biochem.* 266 (2004) 1–7. doi:10.1023/B.
- [8] A Schutze, J.Y. Jeong, S.E. Babayan, J. Park, G.S. Selwyn, R.F. Hicks, The atmospheric-pressure plasma jet: a review and comparison to other plasma sources, *Plasma Sci. IEEE Trans.* 26 (1998) 1685–1694. doi:10.1109/27.747887.
- [9] Ek R. Adhikari, Vladimir Samara, Sylwia Ptasinska, Influence of O₂ and H₂O in a Plasma Jet and its Environment on Plasma Electrical and Biochemical Performances., *J. Phys. D. Appl. Phys.* 51 (2018) 160–166. doi:10.1016/j.apsusc.2016.01.170.
- [10] Xu Han, Yueing Liu, M. Sharon Stack, Sylwia Ptasinska, 3D Mapping of plasma effective areas via detection of cancer cell damage induced by atmospheric pressure plasma jets 3D Mapping of plasma effective areas via detection of cancer cell damage induced by atmospheric pressure plasma jets, *J. Phys. Conf. Ser.* 565 (2014) 1–8. doi:10.1088/1742-6596/565/1/012011.
- [11] J. Gay-Mimbrera, M.C. García, B. Isla-Tejera, A. Rodero-Serrano, A.V. García-Nieto, J. Ruano, Clinical and Biological Principles of Cold Atmospheric Plasma Application in Skin Cancer, *Adv. Ther.* 33 (2016) 1–5. doi:10.1007/s12325-016-0338-1.
- [12] L. Gan, S. Zhang, D. Poorun, D. Liu, X. Lu, M. He, X. Duan, H. Chen, Medical applications of nonthermal atmospheric pressure plasma in dermatology, *JDDG - J. Ger. Soc. Dermatology.* 16 (2018) 7–13. doi:10.1111/ddg.13373.
- [13] H.J. Ahn, K. Il Kim, G. Kim, E. Moon, S.S. Yang, J.S. Lee, Atmospheric-pressure plasma jet induces apoptosis involving mitochondria via generation of free radicals, *PLoS One.* 6 (2011) 6–12. doi:10.1371/journal.pone.0028154.
- [14] S.J. Kim, T.H. Chung, S.H. Bae, S.H. Leem, Induction of apoptosis in human breast cancer cells by a pulsed atmospheric pressure plasma jet, *Appl. Phys. Lett.* 97 (2010) 1–3. doi:10.1063/1.3462293.
- [15] D. O’Connell, L.J. Cox, W.B. Hyland, S.J. McMahon, S. Reuter, W.G. Graham, T. Gans, F.J. Currell, Cold atmospheric pressure plasma jet interactions with plasmid DNA, *Appl. Phys. Lett.* 98 (2011) 98–101. doi:10.1063/1.3521502.
- [16] N.S.J. Braithwaite, Sylwia Ptasinska, Blagovest Bahnev, Agnieszka Stypezynska, Mark Bowden, Nigel J. Mason, DNA strand scission induced by a non-thermal atmospheric pressure plasma jet, *Phys. Chem. Chem. Phys.* (2010) 1–3. doi:10.1039/c001188f.
- [17] E.R. Adhikari, S. Ptasinska, Correlation between helium atmospheric pressure plasma jet (APPJ) variables and plasma-induced DNA damage, *Eur. Phys. J. D.* 70 (2016) 1–6. doi:10.1140/epjd/e2016-70274-6.
- [18] Sylwia Ptasinska, Vladimir Samara, Acoustic Characterization of Atmospheric Pressure Plasma Jets, *Plasma Sci. Technol.* (n.d.) 1–20.
- [19] L. Yan, H. Iwasaki, Thermal Denaturation of Plasmid DNA Observed by Atomic Force Microscopy, *Jpn. J. Appl. Phys.* 41 (2002) 1–5. doi:10.1143/JJAP.41.7556.
- [20] S. L. Berg, Jeremy M., Tymoczko, John L. Gatto, Gregory J. Jr., *Biochemistry*, 8th ed., W. H. Freeman and Company, New York, 2015.